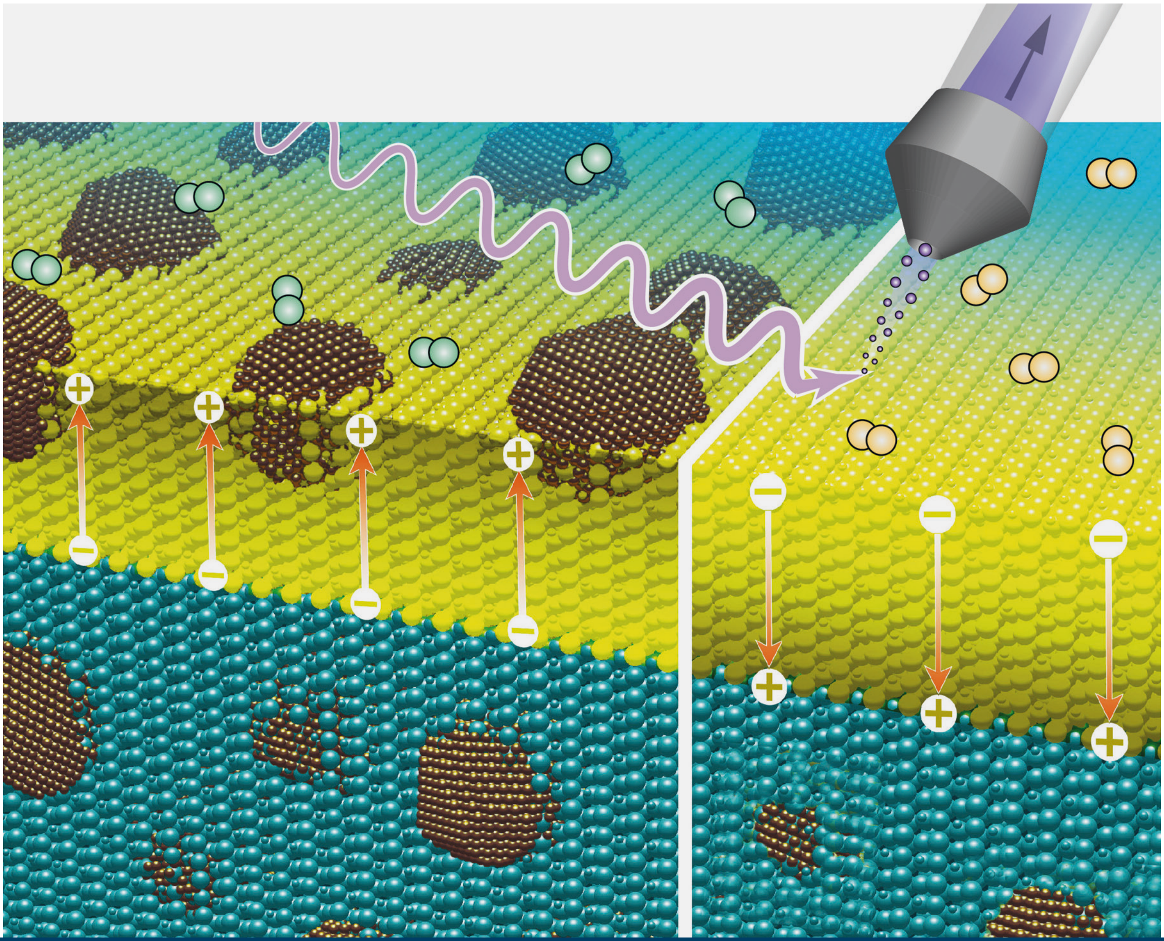

Nanoscale Understanding and Control of Metal Exsolution in Perovskite Oxides

Moritz Lukas Weber

Energie & Umwelt / Energy & Environment
Band / Volume 596
ISBN 978-3-95806-669-4

Mitglied der Helmholtz-Gemeinschaft

JÜLICH
Forschungszentrum

Schriften des Forschungszentrums Jülich
Reihe Energie & Umwelt / Energy & Environment Band / Volume 596

Peter Grünberg Institut (PGI)
Elektronische Materialien (PGI-7)

Nanoscale Understanding and Control of Metal Exsolution in Perovskite Oxides

Moritz Lukas Weber

Schriften des Forschungszentrums Jülich
Reihe Energie & Umwelt / Energy & Environment Band / Volume 596

ISSN 1866-1793 ISBN 978-3-95806-669-4

Bibliografische Information der Deutschen Nationalbibliothek.
Die Deutsche Nationalbibliothek verzeichnet diese Publikation in der
Deutschen Nationalbibliografie; detaillierte Bibliografische Daten
sind im Internet über http://dnb.d-nb.de abrufbar.

Herausgeber und Vertrieb: Forschungszentrum Jülich GmbH
Zentralbibliothek, Verlag
52425 Jülich
Tel.: +49 2461 61-5368
Fax: +49 2461 61-6103
zb-publikation@fz-juelich.de
www.fz-juelich.de/zb

Umschlaggestaltung: Grafische Medien, Forschungszentrum Jülich GmbH

Druck: Grafische Medien, Forschungszentrum Jülich GmbH

Schriften des Forschungszentrums Jülich
Reihe Energie & Umwelt / Energy & Environment, Band / Volume 596

D 82 (Diss. RWTH Aachen University, 2022)

ISSN 1866-1793
ISBN 978-3-95806-669-4

Contents

Abstract

The design of active and durable catalysts is a key requirement for the development of efficient energy conversion technologies urgently needed to meet the challenges of global warming. Metal exsolution has attracted much attention as an elegant synthesis route for nanostructured perovskite catalysts. Thermal reduction of the parent oxide induces the release of reducible cations from the host phase, that assemble in the form of metallic nanoparticles at the perovskite surface. To date the atomistic processes that govern the exsolution behavior in perovskites are inadequately understood. Here, the compositional variety and structural complexity of exsolution-active parent materials often complicate the systematic investigation and comparison of the exsolution response.

This thesis investigates the exsolution of nickel nanoparticles in Nb- and Ni- co-doped strontium titanate on the basis of well-defined epitaxial thin film model systems. The main issues addressed are the principles underlying the accommodation of Ni dopants within the perovskite host lattice, the influence of defects and surface reconstructions on the exsolution behavior and most importantly, the dynamics of metal exsolution processes and the role of surface space charge regions for the exsolution kinetics.

A comprehensive study of the synthesis and structural analysis of ceramic oxides and epitaxial thin films forms the basis of this work. The characterization of the exsolution behavior is based on the detailed analysis of the surface morphology evolution upon thermal annealing at low oxygen partial pressure, combined with methodologies for the control of the sample defect structure, surface chemistry and sample geometry. Furthermore, *in-situ* diffraction and *in-situ* spectroscopy techniques have been employed to study and disentangle the bulk and surface material response of the perovskite during metal exsolution.

Collectively, the combined chemical, structural and morphological investigations under reducing conditions reveal strong surface limitations of metal exsolution. The surface and bulk properties of the material response shows widely different dynamics and appear to be mostly uncorrelated. In accordance, the exsolution volume, *i.e.* the volume of the self-assembled surface nanoparticles is restricted to a small fraction of the total amount of Ni present in the perovskite bulk.

In accordance surface properties were found to govern the exsolution kinetics. In this context, space charge regions at the perovskite surface have emerged to play a key role for the process. The formation of space charge regions was probed under oxidizing and reducing conditions by *in-situ* spectroscopy, and found to be interrelated with the exsolution dynamics. Based on the observations, a novel model of the exsolution process as well as strategies for the control of the metal exsolution behavior by surface engineering is presented.

Achieving control over the surface properties of perovskites is pivotal for the rational design of high-performance energy materials, where the concept of metal exsolution opens novel possibilities for the generation of catalytic centers of high stability.

Kurzfassung

Die Entwicklung aktiver und langlebiger Katalysatoren ist eine wichtige Voraussetzung für die Entwicklung effizienter Energieumwandlungstechnologien, die dringend benötigt werden, um den Herausforderungen der globalen Erwärmung zu begegnen. Die Festkörperausscheidung (exsolution) metallischer Nanopartikel aus Oxidkristallen ist ein eleganter Syntheseweg für nanostrukturierte Perowskit-Katalysatoren. Bei der thermischen Reduktion des Ausgangsoxids werden reduzierbare Kationen aus der Wirtsphase freigesetzt, welche metallische Nanopartikel an der Perowskitoberfläche bilden. Bislang sind die atomistischen Prozesse, die diesen Prozess in Perowskiten bestimmen, nur unzureichend verstanden. Hierbei erschwert die Vielfalt der Materialzusammensetzungen und die strukturelle Komplexität der entsprechenden Ausgangsmaterialien häufig die systematische Untersuchung.

In dieser Arbeit wird die Ausscheidung von Nickel-Nanopartikeln in Nb- und Ni- co-dotiertem Strontiumtitanat anhand von definierten epitaktischen Dünnschicht-Modellsystemen untersucht. Die wichtigsten Aspekte, die behandelt werden, sind die Prinzipien, die der Aufnahme von Ni-Dotierstoffatomen im Perowskit-Wirtsgitter zugrunde liegen, der Einfluss von Defekten und Oberflächenrekonstruktionen auf die Bildung von Nanopartikeln an der Oberfläche und, insbesondere, die Dynamik des Prozesses sowie die Rolle von Raumladungszonen für die Reaktionsdynamik.

Die Grundlage dieser Arbeit bildet eine umfassende Studie über die Synthese und Strukturanalyse von keramischen Oxiden und epitaktischen Dünnschichten. Die Charakterisierung der Nanopartikelbildung basiert auf der detaillierten Analyse der Änderungen in der Oberflächenmorphologie beim thermischen Reduzieren bei niedrigem Sauerstoffpartialdruck, kombiniert mit Methoden zur Kontrolle der Defektstruktur, der Oberflächenchemie und der Geometrie der Proben. Darüber hinaus werden Beugungs- und Spektroskopietechniken eingesetzt um die Änderungen der Materialeigenschaften im Volumen und an der Oberfläche separat voneinander zu untersuchen. In Kombinaton zeigen die chemischen, strukturellen und morphologischen Untersuchungen unter reduzierenden Bedingungen, dass der Prozess welcher die Bildung der Nanopartikel an der Oxidoberfläche verursacht im Wesentlichen auf die oberflächennahe Region des Materials beschränkt ist. In diesem Zusammenhang, wurden signifikante Unterschiede in der Dynamik der (strukturellen und chemischen) Änderung der Oberflächen- und Volumeneigenschaften des Oxids nachgewiesen, welche auf weitgehend separate, unkorrelierte Prozesse hinweisen. Dementsprechend ist das Volumen der an der Oberfläche gebildeten Nanopartikel, auf einen kleinen Bruchteil der Gesamtmenge des im Perowskit vorhandenen Ni beschränkt.

Es wurde festgestellt, dass die Oberflächeneigenschaften die Nanopartikelbildung bestimmen. In diesem Zusammenhang hat sich herausgestellt, dass Raumladungszonen an der Perowskit-Oberfläche eine Schlüsselrolle für den Prozess spielen. Die Bildung von Raumladungszonen wurde *in-situ* unter oxidierenden und reduzierenden Bedingungen mittels Spektroskopie untersucht, und mit der Reaktionsdynamik korreliert. Auf Grundlage der Beobachtungen werden ein Modell der Festkörperausscheidung sowie Strategien für die Steuerung der Nanopartikelbildung durch gezielte chemische Veränderungen der Oberfläche vorgestellt.

Die Kontrolle der Oberflächeneigenschaften von Perowksiten ist von zentraler Bedeutung für die Entwicklung von Hochleistungs-Energiematerialien, wobei das Konzept der Festkörperausscheidung neue Möglichkeiten für die Synthese stabiler katalytischer Zentren eröffnet.

Chapter 1

Introduction

A sustainable energy management that ensures a transition towards net zero carbon emissions is urgently required to limit global warming.[1, 2] Innovative strategies for the design of active and durable catalysts are a key enabler in the development of technologies for the efficient conversion of electrical energy into chemical energy carriers, essential to buffer the inherent intermittency of renewable energy sources.[3–6] In this context, nanostructuring of materials came into focus as an efficient concept to precisely modify the chemical and electronic properties of energy materials, to tailor reaction pathways and to improve the active surface area.[7–12] Furthermore, the application of nanostructured materials is a valuable approach to reduce the load of catalytically active metals that are often scarce.[13]

Lately, the concept of metal exsolution that allows for the nanostructuring of perovskite oxides in a simple, one-step reduction process has received growing attention within the scientific community.[14–18] Here, perovskite oxides are doped with reducible, catalytically active elements that are subsequently exsolved by a reducing thermal treatment to fabricate a nanocomposite. The reaction is driven at low oxygen pressures by the change in the Gibbs free energy ΔG associated with the transition of the respective dopants from the oxidized state to the metallic state.[19–21] In this thesis, I will address the open questions in the mechanistic understanding of metal exsolution processes.

The stoichiometry of exsolution-active perovskites plays a major role for the control of metal exsolution processes. A-site deficient perovskite oxides are often applied in order to increase the nanoparticle yield.[19, 21, 22] The effect is based on the destabilization of the perovskite structure, to promote the spontaneous exsolution of B-site cations by the introduction of a large density of A-site vacancies.[19] Although remarkably large amounts of A-site vacancies can be accommodated by the perovskite structure without causing a loss in the structural coherency[23], high A-site deficiencies are likely to render the stabilization of cations at the perovskite B-site difficult. However, the effects of demixing phenomena and their implications for the strategies to control exsolution processes, typically targeting the global stoichiometry of the perovskite parent materials, has not been investigated so far.

Whilst the driving force for the exsolution of reducible cations is indisputable, the mechanisms that underpin the transport of dopants to the perovskite surface are not fully understood and controversially discussed. While often defect chemical reactions are applied to describe metal exsolution on the basis of ionic diffusion[19, 24, 25], on the contrary, subsurface formation and subsequent migration of extended metallic nanoparticles serve as a basis for the discussion.[26–29]. Diffusive ionic movement during metal exsolution may be subject to similar influences that affect cation segregation processes, such as differences in the ionic radii or the ionic charge that result in strain and electrostatic interactions.[30, 31] For the exsolution of extended particles, however, the minimization of the surface free energy as well as elastic strain at the interface between the metallic nanoparticles and the oxide host lattice, are considered to promote the mass transport.[27, 28]. A systematic understanding of the physical and chemical gradients underlying to the mass transport is lacking. In this context, also the time and length scales at which metal exsolution takes place are inadequately understood[17], which is further complicated since the parameters applied during reducing annealing, such as temperature, oxygen partial pressure and time, are typically chosen on a mere phenomenological basis and widely vary between different studies.

Considering the aspects of metal exsolution processes and the strategies utilized to control the exsolution response that have been discussed above, a clear focus on the bulk properties of exsolution-active perovskites becomes apparent. On the contrary, surface properties have received scant attention[19, 29, 32] and are widely neglected for the rational design of exsolution-type catalysts, despite the fact that the technically relevant process (the self-assembly of nanoparticles at the oxide surface) is a surface process. In view of the significant deviations between bulk and surface properties of (oxide) materials, often associated with the formation of surface space charge regions[30, 33–43], a systematic investigation of the surface properties in ambient reducing and oxidizing environment is of utmost importance. In this respect, also the interrelation between surface reconstructions and the chemical and physical properties of perovskite surfaces deserves further attention.

The questions raised are addressed in this thesis. For this purpose, epitaxial thin film model systems are used to reduce the complexity of the $SrTi_{0.9}Nb_{0.05}Ni_{0.05}O_{3-\delta}$ (STNNi) model material, which is inherent to oxide ceramics due to their microstructure. In comparison, epitaxial thin films can be synthesized with a single crystallographic orientation, with atomically smooth surfaces and without the presence of grain boundaries. Furthermore, reflection high-energy electron diffraction (RHEED)-controlled pulsed laser deposition allows for the precise control of the material thickness and for the control of the defect structure within the perovskite lattice. Epitaxial model systems have proven a valuable tool for the investigation of surface processes due to the high degree of freedom for the control and manipulation of the material properties, advancing the research on energy materials.[27, 29, 44–51]

Outline. The thesis has been organized as follows. Chapter 2 provides a brief review about the fundamentals on theories and concepts which may serve as a background for the discussions made throughout the thesis. Here the fundamentals of metal exsolution, the basic properties of perovskites and their application as energy materials, the defect chemistry of strontium titanate and the principles of mass transport in solids are covered. In chapter 3, the methods applied for the synthesis and analysis of ceramic oxides and epitaxial thin films are introduced and the experimental details of the experiments are depicted.

In chapter 4 the structural and chemical properties of the STNNi ceramics and of the epitaxial thin films in particular are analyzed in detail. Here, a special focus is on the accommodation mechanism of Ni dopants within the perovskite parent material. In addition, the exsolution-activity of the material is demonstrated. Based on the insights gained in chapter 4 a study on the influence of non-stoichiometry for the exsolution of embedded nanostructures, that form during the synthesis process by phase separation from the perovskite host lattice, is discussed in chapter 5.

A methodology that allows the entanglement of the surface and the bulk response of the material is developed in chapter 6. Here, *in-situ* analysis techniques are applied to study the dynamics of the material response under reducing conditions *i.e.* during metal exsolution. In view of the findings, an investigation of the exsolution volume and the exsolution width is presented. In chapter 7, an in-depth analysis of the electrostatic surface potentials that form at the surface of doped perovskites under thermal annealing is given. Essentially, the correlation between the space charge potential, that is intrinsically altered *via* temperature and oxygen pressure, and the metal exsolution kinetics is revealed. A novel model on the mechanistic processes that govern metal exsolution is presented, which takes into account the central role of the surface potential. In this context, a surface engineering strategy is introduced in which the chemistry of the top atomic layers is modified to control the exsolution behavior. Finally, a brief study of the orientation-dependent exsolution response using polycrystalline epitaxial thin films is presented in chapter 8. Here, a discussion of the role of surface reconstructions as exsolution barrier is given on the basis of these more realistic multi-grain model systems.

Chapter 2

Background

This chapter introduces strontium titanate-based perovskite oxides as a material class for energy conversion technologies, as well as the concept of metal exsolution for the nanostructuring of perovskite surfaces. Furthermore, it deals with the fundamental principles of mass transport in solids as well as the defect structure and redox chemistry of (doped) $SrTiO_3$. The chapter provides a background for the discussions on the metal exsolution behavior of co-doped strontium titanate $SrTi_{0.9}Nb_{0.05}Ni_{0.05}O_{3-\delta}$ (STNNi).

2.1 Perovskite energy materials

Functional perovskite oxides

Perovskites exist in manifold compositions, and therefore exhibit numerous interesting properties which make them a promising material class in the field of energy materials.[52, 53] For instance, perovskite oxides may exhibit metallic conductivity[45, 54, 55] or fast oxygen ion conductivity[56, 57] as well as mixed ionic and electronic conductivity.[58]. Their rich variety, and the possibility to control their material properties by tailoring the elemental composition and non-stoichiometry makes them potential candidates for the application as electrode materials in solid oxide cells.[56, 58, 59]

Here, donor-doped titanates have been identified as potential materials to replace the conventional Ni / YSZ fuel electrode[55, 60–64], which suffers from limitations in its redox stability[63], coking[64] and requires high operation temperatures.[8, 59] However, the catalytic activity of donor-doped perovskites for the oxidation of the fuel is often low and therefore strategies to increase the electrocatalytic activity are necessary. Here nanostructuring of the perovskite surface plays a particular role, for instance by means of infiltration or impregnation.[61, 63, 65, 66] Lately, metal exsolution has attracted a lot of attention, as synthesis route for supported nanoparticles.

Metal exsolution as synthesis route for nanostructured perovskites

In recent years, a considerable literature has grown up around the concept of metal exsolution, which was reported to exhibit several advantages over conventional techniques for nanostructuring of perovskite surfaces. The principles of the process are briefly introduced in the following section.

Metal exsolution is based on doping of the perovskite host lattice with reducible, catalytically active elements, that are subsequently exsolved from the oxide host by thermal reduction (Fig. 2.1). The release of the metal cations from the oxide lattice is driven by the change in Gibbs free energy ΔG associated with the transition from the oxidized state to the metallic state.[19–21] Since the exsolution process is induced by a reducing treatment, the concept furthermore allows for the *in-situ* control of the nanoparticle assembly at conditions (T, $p(O_2)$) that are relevant for fuel electrodes of solid oxide fuel cells, which has drawn a lot of attention to the topic.

In this way, perovksites with high electronic conductivity and high redox stability, but typically low catalytic activity serve as parent material for the self-assembly of metallic nanoparticles. The process hence enables to activate perovksite oxides in order to generate electrocatalytic functionality by tailoring their surface properties, most relevant for the activity of catalysts.[16, 58] Based on this concept, the fabrication of high-performance catalysts materials was demonstrated[67–71]

Besides the high simplicity of the exsolution route for the fabrication of uniformly dispersed nanoparticles, and the high efficiency of the method that requires only a very low volume fraction of reducible metals, exsolution nanoparticles were shown to be partly anchored in the oxide support (Fig. 2.1).[32, 72] Consistently, exsolution-type electrodes were shown to exhibit a remarkably high stability with respect to agglomeration.[6, 72–74] Additionally, the process was shown to be in principle reversible [26], which opens the possibility to regenerate catalysts by oxidizing treatment. Ideal exsolution-type catalysts hence may dynamically adapt to the oxygen chemical potential by exsolution and dissolution of dopant cations. Yet, it is still an controversial discussion under what conditions metal exsolution may be reversible.[74]

A considerable amount of research has been published on the effect of non-stoichiometry of the host lattice on the exsolution response. Here, A-site defi-

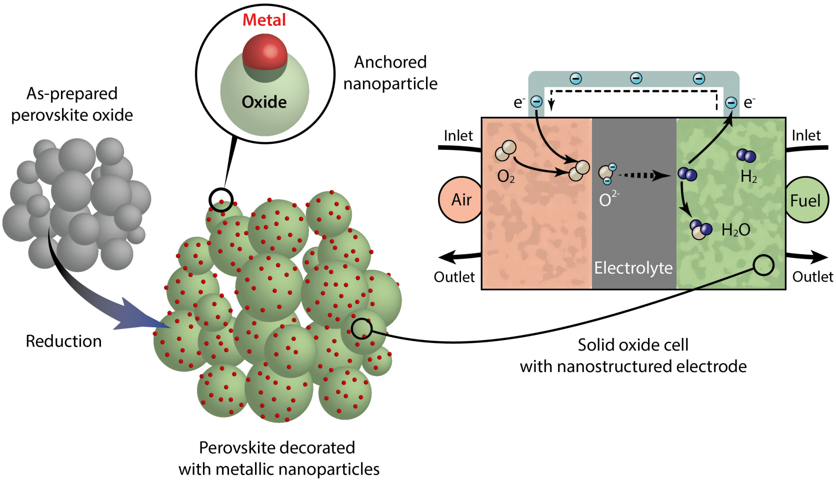

Figure 2.1: Schematic illustration of the concept of metal exsolution. Exsolution-active perovskite parent materials accommodate reducible dopants that are exsolved to the surface upon a reducing thermal treatment, which results in the self-assembly of metallic nanoparticles that are anchored at the surface of the oxide support. For instance, exsolution-type, nanostructured materials may be promising candidates for the application in fuel electrodes in solid oxide cells.

ciency has established as valuable tool to destabilize the perovskite structure and to promote the spontaneous exsolution of B-site cations from the crystal lattice in order to increase the nanoparticle yield at the perovskite surface.[19, 21, 22] Beyond this (effective) lever, several parameters have been identified that potentially influence exsolution processes which have been summarized in several review articles.[17, 18, 31, 53, 75] However, the exact mechanisms underlying to metal exsolution remain unclear. The questions that will be addressed in this thesis have been elaborated in the introduction (chapter 1) and can be summarized as follows.

- How are Ni dopants accommodated in the perovskite lattice and what is the influence of defects on the exsolution behavior?
- Where does the reduction process takes place (bulk *vs.* surface), what is the exsolution width and what is the dynamics of the exsolution process?
- What is the role of the surface properties and the formation of surface space charge regions in particular and how can surface engineering be utilized to control the exsolution behavior of perovskite oxides?

Metal exsolution and cation segregation

Exsolution processes are known since many decades and generally describe the release of cations from a crystal by partial consumption of elements from the crystal lattice, which is often accompanied by the formation of a secondary phase at the surface. Another term frequently used to describe the release of cations from the host phase is cation *segregation*. While both processes appear to be macroscopically similar, the connotation of both terms is different, where researchers commonly refer to segregation when the release of cations results in undesirable changes of the material properties such as stability issues.[76–79] In contrast, the term (metal) *exsolution* is often used when such processes are utilized to actively change the material properties for the purpose of functionalization, *i.e.* the self-assembly of metallic nanoparticles at perovskite surfaces.

In this context, exsolution processes may share similarities with cation segregation processes with respect to parameters that impact both phenomena. [30, 31] However, one major difference is that exsolution processes are typically induced by a reducing thermal treatment. Here, the exsolution concept makes use of the instability of the reducible cations, and high stability of the host lattice under reducing conditions. Cation segregation, however, usually describes the formation of surface phases under *oxidizing* conditions.

Throughout this thesis, the term exsolution will be used to describe the self-assembly of reducible dopants, that are accommodated in the perovskite bulk, in the form of metallic nanoparticles at the perovskite surface.

2.2 The defect structure of $SrTiO_3$

$SrTiO_3$ (STO) is an ionic crystal of perovskite structure with a face centered cubic unit cell. The Ti B-site is located in the center, while the Sr A-sites occupy the corners and the oxygen anions are located at the face centered sites of the ABO_3 unit cell (Fig. 2.2a). Here, the B-site is six-fold coordinated to the oxygen ions (TiO_6 octahedral), while the A-site occupies a site with twelve-fold oxygen coordination.[80]

Transition metal oxides such as STO exhibit a strong tendency to incorporate defects which results in deviations from the ideal perovskite structure.[80] The defect structure fundamentally influences the properties of functional oxides, such as electronic and ionic conductivity. Understanding the nature of the defect structure hence is fundamental for the understanding and control of the material properties.

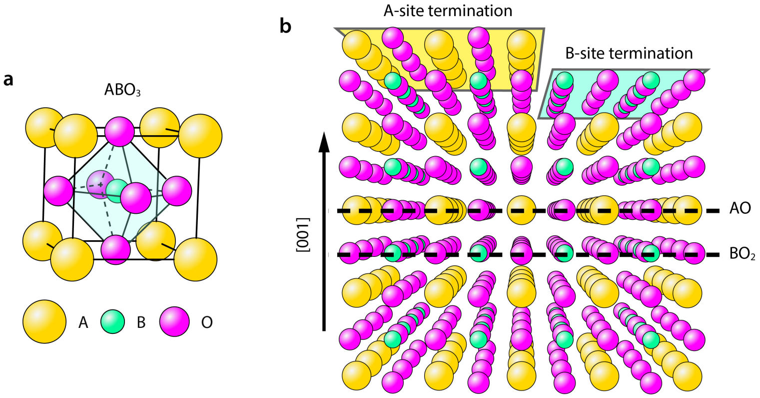

Figure 2.2: (a) Schematic sketch of a cubic perovskite unit cell. (b) Illustration of the perovskite crystal lattice in [001]-orientation, which consists of alternating AO and BO_2 planes. The model is constructed by 4 x 4 x 4 perovksite unit cells. To improve visibility of the B-site cations, the first atomic layer was removed from the model. According to the stacking sequence, the surface may be either AO or BO_2 terminated.

Point defects

Point defects are the simplest kind of defect in a crystal lattice (0D). In perovskites, the only intrinsic point defects are oxygen or cation vacancies, since the formation of interstitials can be neglected in consequence of the high packing density of the perovskite structure.[81] The formation of point defects in STO hence can be described by the formation of Schottky vacancy pairs in accordance with the charge neutrality condition. Here, the formation of a point defect is compensated by one or multiple electronic or ionic charges (defects) of opposite sign. Moreover, extrinsic point defects may be accommodated within the STO lattice. Extrinsic defects substitute a regular ion of the material by occupying the respective lattice site, for instance by incorporation of impurities or due to deliberate doping of the crystal lattice.

With increasing point defect concentrations, the probability for interactions between the charged defects increases (electrostatic and strain interactions), which may finally result in the formation of defect structures of higher dimension, such as vacancy clusters or secondary phases.[80]

Surface

Surfaces may be considered as crystal defect that results from the truncation of the periodic lattice. As illustrated in Fig. 2.2b, the [001]-oriented perovskite lattice can be described as a stack of alternating AO and BO_2 planes. Therefore either an AO plane or a BO_2 plane may be present as terminating atomic layer. Naturally, native perovskite surfaces exhibit a mixed AO / BO_2 termination. Notably, the atomic surface composition deviates for surfaces of different crystallographic orientation, which influences the surface termination.

For instance native (001) STO single crystals typically exhibit a termination ratio of 5 - 25% SrO / 95 - 75% TiO_2 [82], while chemical etching may allow to prepare a close to perfectly TiO_2-terminated crystal surface.[82, 83] The surface termination may considerably influence characteristic properties such as oxygen exchange kinetics.[84] It is worth pointing out that with increasing surface-to-volume ratio the surface becomes more and more important for the overall material properties and hence is of particular significance for thin film materials.

In general, the characteristics of surfaces significantly deviate from the bulk properties of (perovskite) materials. The truncation of the coherently ordered crystal lattice results in the presence of unsaturated bonds, *i.e.* ions located in the topmost atomic layer exhibit a reduced coordination compared to ions which occupy lattice sites that are located in the interior of the crystal bulk (assuming no defects as direct neighbor). Due to the broken symmetry of the crystal lattice, the redistribution of defects or and even the reconstruction of the surface may become energetically favorable.[85–87] As a result the density and distribution of point defects and extended defects may be different in the near-surface region compared to the bulk.[42, 88, 89]

Defects of higher dimension

Edge- and screw dislocations may be present in the crystal lattice. Dislocations are one-dimensional (1D) defects, and describe the deviation of the regular crystal lattice along a dislocation line. An edge dislocation describes the presence of an extra half plane of atoms within the lattice, which results in deviations in the regular ordering of the adjacent crystallographic planes. Screw dislocations describe a structural feature which results from a partial displacement (slip) of a crystallographic plane in direction of the dislocation line. Moving along the dislocation line consequently results in an extended defect structure that helically penetrates the crystal.[90] Dislocations are frequently observed for STO single crystals[91, 92] and may become visible as etch pits by preferential etching of screw dislocations after chemical treatment of the STO surface.[93]

Stacking faults are another common type of (2D) defect in the crystals lattice of perovskite structure. Here, the regular stacking sequence of atomic planes *AO*-BO_2-*AO*-BO_2 is locally altered to *e.g.* BO_2-*AO*-*AO*-BO_2. Stacking faults hence describe planar defects that are based on a double layer of either AO or BO_2 crystallographic planes that disrupt to the nominal atomic order. In perovskites, stacking faults can be considered as anti-phase boundaries. In STO the formation of Ruddlesden-Popper (RP) type anti-phase boundaries is frequently observed.[94]

Grain boundaries are (2D) defects that describe the perturbation of multi-grain bulk materials on the basis of interfaces between two adjacent grains of different crystallographic orientation. Phase boundaries are defects (2D) that separate grains of different crystal structure, *e.g.* different phases. Such phase boundaries may occur at the interface between inclusions and their a host phase, but may also describe the interface between the substrate and the thin film material during epitaxial growth. The interface may be coherent if the mismatch between the structural properties of both phases (orientation, lattice parameter, etc.) is low. With increasing deviation of the lattice parameters, edge dislocations may be introduced close to the interface to compensate for the increasing elastic energy. At large deviations the interface is non-coherent.[90] In particular cases, so-called semi-coherent interfaces may be energetically favorable.[95, 96] Here, the mismatch at the interface is compensated by matching not single unit cells, but registries of several unit cells of both phases. Moreover secondary phases present within the crystal lattice in form of inclusions may be considered as (3D) defects, similarly to voids, pores or cracks.

The accommodation of non-stoichiometry is entangled with the defect structure of perovskites. The nature of the defect structure, however strongly depends on the synthesis conditions. Therefore, sintered ceramics that are synthesized under thermodynamic equilibrium conditions can be expected to exhibit a different defect structure compared to epitaxial thin films deposited by non-equilibrium techniques. A brief comparison on the different mechanisms that apply for sintered ceramics and epitaxial thin films of strontium titanate is given in reference [97] and references therein. Furthermore, mechanical stress due to material processing, such as surface polishing may influence the density of dislocations in the near-surface region.[88]

Notably, extended defects and in particular surfaces or grain boundaries may serve as sinks (and sources) for point defects. For instance, the release of a crystal atom to the surface enables the formation of a vacancy. Surface atoms may either contribute to the native crystal lattice or form precipitates *i.e.* secondary phases.[90]

2.3 Mass transport in solids

Mass transport in solids proceeds *via* diffusion, which is based on the mobility of point defects within the crystal lattice. Therefore, any process that involves mass transport, such as metal exsolution or oxygen exchange is coupled to the defect structure. Diffusive jumps of crystal atoms between vacancies enable the migration of ions in perovskites upon thermal activation (since interstitials can be ruled out, *cf.* section 2.2).[98]

Fick's first law describes the relation between local variations in the concentration of a species and the diffusive flux

$$j_\mathrm{i} = -D_\mathrm{i} \cdot \frac{\partial c_\mathrm{i}}{\partial x} \tag{2.1}$$

where j_i is the diffusive flux, D_i is the diffusion coefficient and c_i is the concentration of the diffusing species i. The position is denoted by x. Notably the driving force for diffusion is a difference in the chemical potential of a species that is correlated to local variations in the concentration of the species in a homogeneous material and generates a gradient in its mobility. If no concentration gradient is present there is no net flux (self-diffusion). Here, the thermally activated ion jumps are considered to be uncorrelated (random walk). In contrast, random walk diffusion leads to mass transport that is proportional to the diffusion coefficient when a concentration gradient is present (chemical diffusion). [99]

The diffusion coefficient is mainly determined by the jump rate and the jump distance. The total jump rate is proportional to the concentrations of vacancies, since mass transport *via* vacancy diffusion requires the exchange of an atom with a vacancy at a neighbouring lattice site. Furthermore, the jump rate, and hence diffusion processes in general are temperature dependent, as the thermally activated diffusion process proceeds by successive jumps from one lattice site to another.[87, 99]

While diffusion relies of the mobility of vacancies, defects of higher dimension as well as grain boundaries in multi-grain materials may considerably influence the diffusion kinetics. For instance anti-phase boundaries were shown to serve as fast diffusion pathways for cations in STO.[100] In ceramic materials, diffusion along and across grain boundaries may strongly influence the diffusion characteristics, which can result in facilitated or hampered oxygen diffusion.[98, 101, 102] Notably, mass transport processes that involve the exchange between the ambient gas phase and a solid, such as the incorporation of oxygen into STO, additionally depend on the surface exchange coefficient k^*. Since the surface reaction is a complex multi-step reaction, the surface exchange rate may considerably influence the diffusion process of oxygen into solids.[103]

All kind of solid-state reactions that are subject of this thesis, such as nucleation, crystal growth, reduction / oxidation or sintering proceed in order to obtain a state of minimal free energy with respect to the ambient thermodynamic conditions.[104] The kinetics of these solid-state reactions, however, rely on thermally activated diffusive mass transport.[98]

2.4 Defect chemistry of donor- and acceptor-doped $SrTiO_3$

To understand the interplay of extrinsic and intrinsic defects in acceptor- and donor-doped STO, the respective defect equilibria need to be considered in view of the conservation of charge and mass. The bulk defect chemistry of STO can be described by Brouwer diagrams that show the defect concentrations as a function of the oxygen partial pressure $p(O_2)$. Here, the mechanisms for charge compensation and hence the electronic and ionic properties of STO strongly depend on the $p(O_2)$ as well as the sample temperature. Elevated temperatures allow for an active Schottky-equilibrium which triggers charge compensation on the basis of defect chemical reactions that are different from the room temperature case (*cf.* section 2.3). Therefore, it is necessary to differentiate between the case of an active Schottky equilibrium and an inactive Schottky equilibrium. In the following, the redox chemistry of doped STO is briefly depicted (Kröger-Vink notation is used [105]). For an in-depth discussion of the defect chemistry of STO, the reader is referred to [106–108]. The bulk characteristics often significantly differ from the surface properties and hence shall be briefly depicted in the following section.

Bulk

Acceptor-doped STO

The Brouwer diagrams for acceptor doped STO is shown in Fig 2.3a. In the *intrinsic* regime, the defect equilibria are depicted for low $p(O_2)$, *i.e.* for highly reducing conditions. Here oxygen vacancies are incorporated into the perovskite lattice that are partly compensated by extrinsic acceptor-dopants A'. In the case that the oxygen vacancy concentration exceeds the extrinsic dopant concentration, the excess charge related to the additional fraction of oxygen vacancies is compensated by electrons. In contrast, an increase of the the oxygen partial pressure results in the successive decrease of the oxygen vacancy concentration $[V_O^{\bullet\bullet}]$ until it is one half of the acceptor-doping level. In the *extrinsic* (n-type) regime, further increase of the $p(O_2)$, however does not result in a further decrease of $[V_O^{\bullet\bullet}]$, which is now pinned with respect to the acceptor-doping level. Instead, the electron concentration decreases with decreasing $p(O_2)$, while in turn the hole concentration increases. At a certain $p(O_2)$, the hole concentration crosses and exceeds the electron concentration, which marks the p-type regime of acceptor-doped STO.

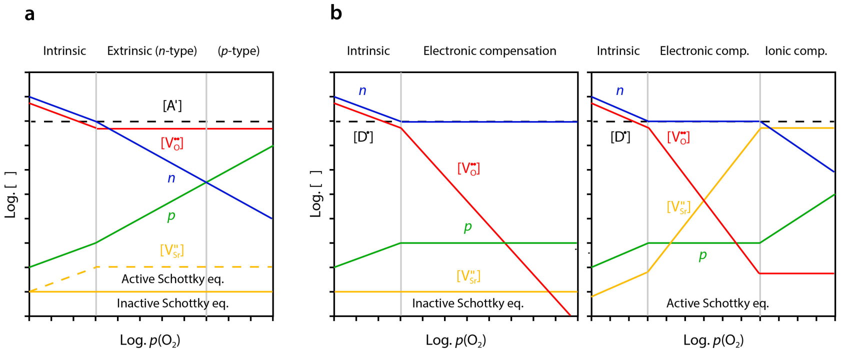

Figure 2.3: Schematic Brouwer diagrams for (a) acceptor-doped STO and (b) donor-doped STO. The diagrams illustrate the defect concentration as a function of the oxygen partial pressure. The figure design was adapted from reference [106].

Under certain conditions, another defect chemical reaction, namely the Schottky-equilibrium needs to be considered to accurately describe the STO defect chemistry. It comes into play at elevated temperatures. Here, strontium vacancies V''_{Sr} act as mobile acceptors and contribute to the interplay of the defect equilibria. The strontium vacancy concentration $[V''_{Sr}]$ may increase with increasing oxygen partial pressure within the *intrinsic* regime and remains constant after transition to the *extrinsic* regime.

Donor-doped STO

The Schottky-equilibrium plays a more important role for the defect chemistry of donor-doped STO and renders the defect equilibrium more complex. Therefore two different Brouwer diagrams are shown, which depict the defect chemistry of donor-doped STO for the case of a frozen Schottky equilibrium (Fig 2.3b, left) and for the case of an active Schottky-equilibrium (Fig 2.3b, right). As for the discussion of acceptor-doped STO, initially the case of a frozen Schottky-equilibrium is considered.

In highly reducing conditions, *i.e.* in the *intrinsic* regime, large oxygen vacancy concentrations dominate the conductivity of *n*-STO. The $[V_O^{\bullet\bullet}]$ decreases with increasing oxygen partial pressure. When $[V_O^{\bullet\bullet}]$ falls below the concentration of extrinsic donors $[D^{\bullet}]$ the electron concentration is pinned to the donor concentration. $[V_O^{\bullet\bullet}]$ decreases further with increasing oxygen partial pressure within the regime of *electronic compensation*, which is maintained toward highly oxidizing conditions as long as the Schottky-equilibrium is not active.

When the Schottky-equilibrium is active, the contribution of mobile strontium vacancies results in a modification of the defect chemistry of *n*-STO. Here, the oxygen vacancy concentration $[\mathrm{V_O^{\bullet\bullet}}]$ is coupled to the strontium vacancy concentration $[\mathrm{V_{Sr}''}]$. Consequently, the amount of $\mathrm{V_{Sr}''}$ increases with increasing oxygen partial pressure within the *intrinsic* region and the region of *electronic compensation* in order to compensate the positive charge of the donor dopants.

When all donor dopants are compensated by strontium vacancies $\mathrm{V_{Sr}''}$ the regime of *ionic compensation* is reached. Further increase of the oxygen partial pressure results in a decrease in the electron concentration, which is related to the 'over-oxidation' of the perovskite. Here, molecular oxygen is reduced by consumption of electrons and a SrO phase is formed at the perovskite surface.

Surface

As discussed above, the distribution of mobile charge carriers in the near-surface region is often considerable altered compared to the bulk (*cf.* section 2.2). Here, the defect chemistry within a space charge region (SCR) at the perovskite surface often dictates the material properties, as will be addressed below. The magnitude of the resulting space charge potential depends on the oxygen partial pressure and the temperature, while the width of the extended space charge region is predominantly determined by the concentration of acceptor or donor dopants.

Acceptor-doped STO

As a consequence of the truncated crystal lattice (*cf.* section 2.2), the formation energy for oxygen vacancies is decreased at the surface of STO, which results in the formation of a positive surface charge by accumulation of oxygen vacancies (Fig. 2.4a).[42, 43, 84, 109, 110] As a result of the redistribution of oxygen vacancies from the perovskite bulk to the surface, a region of decreased oxygen vacancy concentration is formed adjacent to the positively charged layer that is confined to the topmost perovskite surface.[42, 43, 84] The space charge region is enriched by electrons which accumulate in order to compensate the positive surface charge. The electron accumulation layer results in enhanced electronic conductivity, but low oxygen ion conductivity within the space charge region, directly coupled to the space charge potential. The magnitude of the positive surface charge decreases with decreasing oxygen partial pressure.

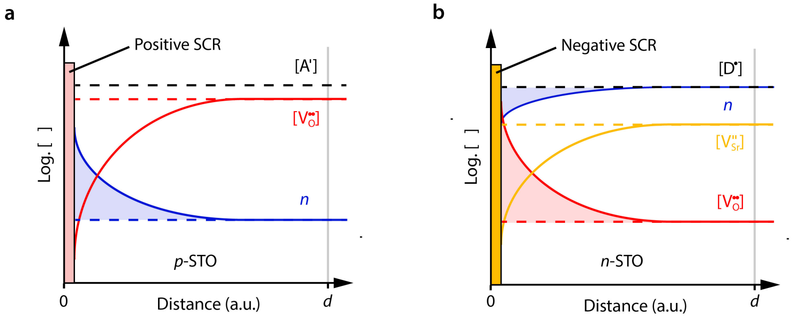

Figure 2.4: Simplified illustration of surface concentration of defects in the surface region after thermal activation of the ionic sublattice under oxidizing conditions. (a) Acceptor-doped STO and (b) donor-doped STO. Dashed lines denote bulk concentrations. The position of the solid-gas interface is denoted by 0 while bulk-like defect concentrations can be found a increased distance from the surface region *d*. The figure design is inspired by (a) reference [89] and (b) [108, 109]

Donor-doped STO

In comparison, a negative space charge region is typically established at the surface of *n*-STO in oxidizing conditions (Fig. 2.4b). Here, the annihilation of oxygen vacancies is promoted, while the formation of negatively charged strontium vacancies is mediated by the Schottky-equlibrium.[107–109, 111–113] Notably, the Schottky equilibrium is active at the topmost surface of the perovskite even at moderate temperatures.[111, 114]

The acceptor-type cation vacancies compensate the charge of donor-dopants that were initially compensated by electrons. Simultaneously, the surface becomes depleted from electrons due to the reduction of molecular oxygen from the ambient atmosphere, forming an SrO surface phase.[108] In consequence, a negative surface potential is established due to the accumulation of negatively charged Sr vacancies, which are kinetically trapped in the surface region.[108] The magnitude of the negative surface potential decreases (becomes more positive) with decreasing oxygen partial pressure. At highly reducing conditions, the formation of Sr vacancies may be widely suppressed while the introduction of oxygen vacancies into the perovskite lattice is promoted, which are energetically trapped in the surface region.[43, 109, 110, 115]

Chapter 3

Experimental methods

This chapter provides a brief overview about the various experimental techniques used for the preparation and characterization of ceramics and thin film samples. It covers the fundamentals of solid state synthesis, structural and chemical analysis as well as surface imaging methods. Many of the methods described below are based on the interaction of photons, electrons or ions with matter. Here, the various processes inherent to these interaction can be used to obtain a comprehensive picture of the materials' characteristics. Please note that some schematic figures where were adopted in a modified form from my previous work [116].

3.1 Sample synthesis and processing

3.1.1 Powder synthesis

Pechini synthesis

The Pechini method is a sol-gel route for the synthesis of complex oxide powders from a liquid phase. The solid educts (typically nitrate salts) are dissolved in deionized water, and citric acid is added to stabilize the metal ions by complexation and to achieve a homogeneous distribution of the elements. On the basis of the aqueous solution a gel is prepared using a polyhydroxy alcohol (ethylene glycol) to preserve the homogeneous distribution of the elements during the subsequent high temperature calcination. For that purpose, the water content of the gel is continuously reduced by a long-term heat treatment at low temperatures until a highly viscous resin is formed. Subsequently the organic constituents are decomposed by a high temperature treatment and calcination is performed after milling of the product.[117, 118]

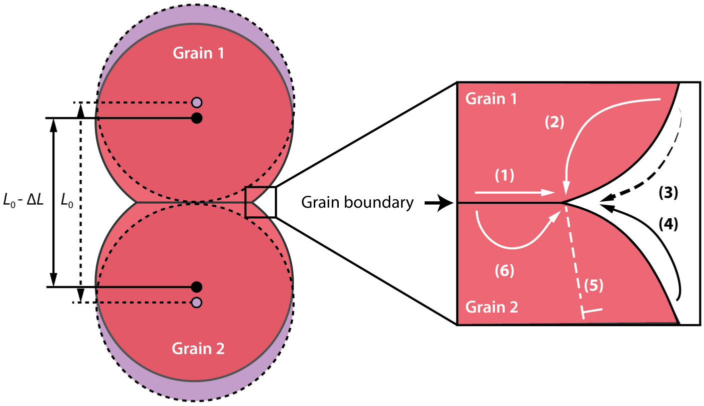

Figure 3.1: Schematic illustration of grain growth by joining of two adjacent grains. The grain growth proceeds *via* mass transport from the grains to the neck region, where the initial distance L_0 decreases in the course of sintering. The different pathways for the mass transport are depicted in the right panel. (1) Diffusion along grain boundary (2) volume diffusion from surface (3) evaporation-condensation (4) surface diffusion (5) plastic flow (dislocations) (6) volume diffusion from grain boundaries. The figure design is inspired by reference [119].

Mixed oxide synthesis

The mixed oxide synthesis route (MOR) is based on a solid state reaction between the compounds of a mixture that contains the elements of the desired product in stoichiometric amounts. The compounds are homogenized and heated in air in order to decompose the original compounds (*e.g.* carbonates) and form oxides. Here, the reaction of the powders to the desired product proceeds by transport of elements from one phase to another and *vice versa*. The reaction therefore proceeds by the formation of a reaction layer at the surface of both phases, that increases in thickness during the time of calcination until the reaction is completed over the entire grain thickness. Here, the oxidizing treatment at high temperatures, provides for the thermodynamic driving force and the kinetic conditions (large diffusion lengths) that are required to favor the reaction towards the oxide product.[117]

Processing and sintering

For the fabrication of oxide ceramics, green bodies are prepared from the calcined powders to define a shape and optimize the materials density for the sintering process. Uniaxial pressing results in the partial densification of the material. Here, pressure is put onto the powder by means of two metallic punches. Due to the pressing geometry and the complexities of mass flow in the powder compact, however, considerable variations in the packing density can result, especially for powder with irregular particle size distributions or particle shape. Therefore, additional isostatic pressing is carried out at room temperature to improve the uniformity and green density before sintering. For this purpose the green bodies are sealed and compressed in a pressurized oil bath.[117]

The green bodies are densified by sintering at high temperatures. Here, grain growth is typically based on joining of particles by mass transport from the grains to the neck region. The pathways of mass transport are manifold (Fig. 3.1) and may involve surface diffusion, volume diffusion from the surface and the grain boundary, diffusion along the grain boundary, plastic flow on the basis of dislocations or evaporation and condensation processes.[119]

Experimental details

In the first step, the Pechini synthesis route and the MOR were applied for the preparation of strontium titanate powders of different doping compositions with the general chemical formula $SrTi_{1-(z+x)}Nb_zNi_xO_{3-\delta}$. In a second step, ceramic pellets were sintered which were used to confirm the exsolution activity of the material, and further, for the application as target materials for the growth of epitaxial thin films by pulsed laser deposition.

For the powder synthesis *via* the Pechini method, stoichiometric amounts of the educts (titanium (IV) isopropoxide (97 %) pre-processed as described by reference [120], strontium nitrate (99 %), ammonium niobate (V) oxalatehydrate (99.99 %), and nickel(II) nitrate hexahydrate (99.99 %)) were dissolved in deionized water and the metal ions were stabilized by complexation with citric acid. Ethylene glycol was added while the solution was stirred and after homogenization of the mixture for 24 h at a temperature of T = 50°C, polymerization was induced by a successive increase of the temperature to T = 350°C. The product was calcined in a two-step process at T = 700°C and T = 900°C for 3 h respectively, using a tube furnace. After preparation of a slurry in isopropanol, the powder was ball milled for 24 h and dried by means of a rotary evaporator. Using an organic binder (3.5 wt%) ceramic pellets were uniaxially and cold-isostatically pressed and, after debinding at T = 600°C for 12 h, the green bodies were sintered at T = 1100°C for 6 h in air. The cation stoichiometry was quantified by ICP-OES analysis using a piece of the ceramic pellet which was cut with a diamond wire saw from the bulk sample.[1] For this purpose, a fusion of the sample was prepared with lithium borate in a Pt / Au crucible (30 min, T = 1000°C), which was subsequently dissolved in HCl / H_2O_2. Based on the dissolved material, a composition of $Sr_{0.97}Ti_{0.905}Nb_{0.046}Ni_{0.048}O_{3-\delta}$,

---

[1] The ICP-MS measurements were performed by V. Nischwitz (Central Institute for Engineering, Electronics and Analytics (ZEA-3), Forschungszentrum Jülich GmbH, 52425 Jülich, Germany) whose support is highly appreciated.

close to the nominal stoichiometry of the Nb- and Ni-(co)-doped strontium titanate (STNNi), was determined. Furthermore, $SrTiO_{3-\delta}$ (STO), single-doped $SrTi_{0.95}Nb_{0.05}O_{3-\delta}$ (STNb) and single-doped $SrTi_{0.95}Ni_{0.05}O_{3-\delta}$ (STNi) were synthesized as reference materials.

Additionally, ceramic pellets with systematically varying substitution level of the titanium cations by Ni dopants at the perovskite B-site were prepared. Here, $SrTi_{0.95-x}Nb_{0.05}Ni_xO_{3-\delta}$ with x = 0.005, 0.01, 0.03, 0.05 and 0.1 were fabricated by the MOR. For this purpose a slurry of the educts was prepared by mixing STOichiometric amounts of titanium (IV)oxide nanopowder (99.7 %), strontium carbonate ($\geq$98 %), niobium-(V) oxide (99.99 %), and nickel (II) oxide nanopowder (99.99 %) with isopropanol of analytical grade. The mixture was homogenized by ballmilling (24 h) and the powder was calcinated at T = 1100°C for 8 h. The product was ground by mortar and pestle and a slurry (in isopropanol) was ball milled for 24 h. The product was dried using a rotary evaporator and, after adding an organic binder (3.5 wt%), ceramic pellets were prepared by uniaxial and cold-isostatic pressing. After debinding at T = 600°C for 12 h, the pellets were sintered in air for 12 h at T = 1200°C. Here, the sintering temperature was limited to T = 1200°C, since pre-studies have shown that higher temperatures result in the partial depletion (evaporation) of nickel from the oxide sample.

3.1.2 Pulsed laser deposition

Pulsed laser deposition

Pulsed laser deposition (PLD) is a non-equilibrium technique for the deposition of thin films, that can be utilized for the epitaxial growth of complex oxides. For the growth processes of stoichiometric samples, the fine-tuning of several parameters is required, which jointly influence the growth process and, eventually, determine the sample properties. Accordingly, slight adjustments of the growth parameters can be utilized to manipulate the sample characteristics, such as the material's stoichiometry.[121]

Highly energetic laser pulses are directed onto the ceramic target that is located in an enclosed chamber under low oxygen partial pressure, to ablate the oxide material (Fig. 3.2a). Multi-photon excitation processes result in the generation of a plasma. Based on the conversion of the ionization (and thermal) energy that is introduced into the ceramic material during ablation, the plasma plume expands in direction of the substrate, which is oriented in parallel to the target surface. In consequence the ablated species (ionic and neutral single elements and clusters) are transported towards and deposited at the substrate surface.

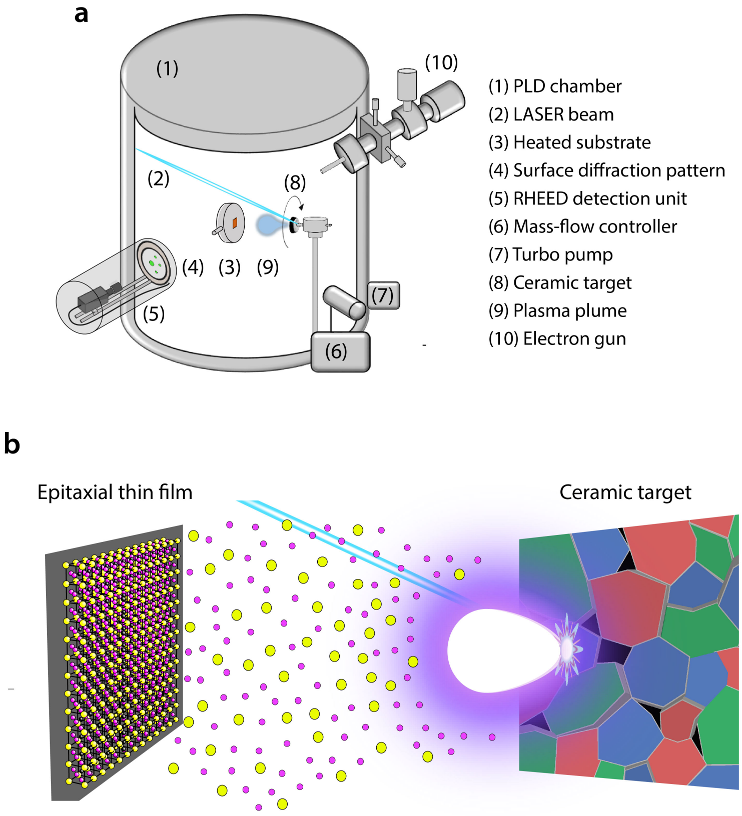

Figure 3.2: (a) Schematic illustration of the pulsed laser deposition setup. The heated substrate is located in an enclosed chamber which is equipped with a vacuum pump and a mass-flow controller. The spinning ceramic target is located in front of the substrate, where the substrate surface and target surface are oriented parallel to each other. An excimer laser is used for the ablation of the ceramic material. The growth kinetics is monitored *in-situ* by reflection high-energy electron diffraction utilizing a deferentially pumped electron gun. The electron surface diffraction pattern is recorded on a phosphor screen. (b) PLD allows the stoichiometric transfer of complex materials from multi grain ceramic material into thin films with single crystalline character.

The kinetic energy of the ablated species is determined by mass- and energy-dependent scattering with the ambient gas molecules and hence strongly depends on the oxygen partial pressure. A fraction of the ablated material impinges on the substrate and remains at the surface. Since the substrate surface exhibits a characteristic step terrace morphology, the energetic landscape is anisotropic and certain locations are energetically favorable for the nucleation of the adspecies. Therefore, the nature of the growth kinetics, is widely determined by the interplay of kinetic energy of the mobile adspecies, the surface energy of the substrate and the interface energy of the substrate and thin film material, which manifests in the effective diffusion length of the adspecies.[121]

By optimization of the growth parameters, high quality epitaxial layers can be deposited, where the ablated material adapts the atomic ordering of the crystalline substrate serving as a template for the nucleation. In this way, epitaxial growth enables the stoichiometric transfer of multi-component oxide targets, that are composed of multiple grains with randomly distributed crystallographic orientations and often exhibit a porous structure to a thin film of single-crystalline character (Fig. 3.2b).

Reflection high-energy electron diffraction

The thin film growth by non-equilibrium techniques is fundamentally different from the processes that occur during crystal growth during sintering. Yet, both processes are considerably influenced by the mobility of the involved species. Based on the pulsed nature of the ablation and due to the fact that the deposition time is typically short compared to the diffusion time, the deposition and the nucleation process during epitaxial growth can be considered as separate processes.[122] Different growth modes can be distinguished to describe the growth characteristics. The growth mode is analyzed *in-situ* by reflection high-energy electron diffraction (RHEED). Here, highly-energetic electrons are directed in a grazing angle on the substrate / thin film surface. The RHEED pattern is monitored using a phosphor screen, that is recorded by a CCD camera (Fig. 3.2a).

A high mobility of the adspecies results in large diffusion lengths and enables intra- and interlayer diffusion, which typically manifests in a 2D-growth mode. Here, facile migration of the adspecies to the energetically favorable step ledges results in layer-by-layer (FRANK-VAN-DER-MERWE) growth. At very high mobility of the adspecies, step flow growth takes place. With decreasing mobility the probability for the nucleation of the adspecies on top of the terrace steps increases. Here, nucleation events may occur before the underlying monolayer is completed. This multilayer nucleation (STRANSKI-KRASTANOV growth) may result in the formation of 3D-islands when the adspecies' mobility is very low (VOLMER-WEBER growth).[123–126]

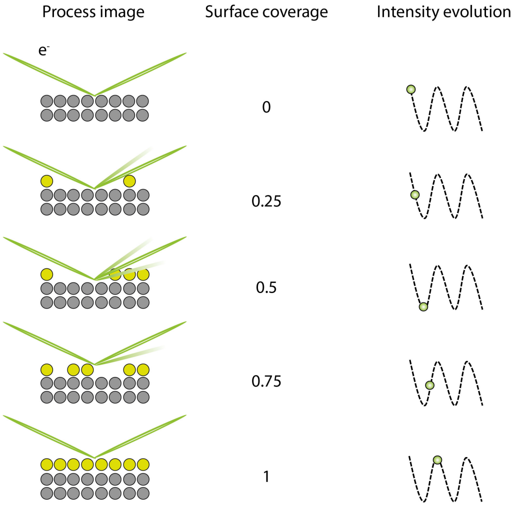

Figure 3.3: RHEED-monitoring of the growth process. Electrons are directed onto the thin films surface in a grazing angle. The diffracted signal is sensitive to the surface coverage with adspecies, which alternately increases and decreases over the course o material deposition and monolayer nucleation. The growth process hence can be analyzed on the basis of the intensity evolution.

The surface diffraction pattern provides information about the atomic structure, the roughness and the termination of crystal surfaces. Most importantly, however, evaluation of the intensity evolution of the diffraction signals over time provides information about the growth kinetics and allows to control the deposition rate and to optimize the deposition parameters with respect to the growth mode.

Since the RHEED intensity is sensitive to the step density (step ledges, nucleates, 3D-islands) which depends of the surface coverage, it allows to follow the growth kinetics with monolayer accuracy (Fig. 3.3). Consequently, layer-by-layer growth is visible by distinct intensity oscillations. During step flow growth, the step density remains constant and hence a constant RHEED intensity is evident. The growth of 3D-island results in the evolution of a 3D-pattern and eventually in a drop of the RHEED intensity due to extensive roughening of the surface.

More details on the growth of complex oxides by PLD and RHEED analysis can be found in ref. [121, 125].

Experimental details

Preparation of single-crystalline $SrTiO_3$ substrates

Single-crystalline [001]-oriented STO substrates (*Shinkosha Co. Ltd.*) are applied for the deposition of epitaxial STNNi and STNi thin films. Prior to the thin film growth the as-received, epi-polished oxide substrates of mixed SrO / TiO_2 termination are typically etched in buffered hydrofluoric acid (BHF, ~10% HF) for 2 min 30 s to remove SrO from the surface in the form of $Sr(OH)_2$, leaving behind a uniformly TiO_2-terminated STO crystal.[83] The standard procedure for the preparation of TiO_2-terminated STO and Nb:STO substrates is given in table 3.1.[2] Apart from BHF etching, the termination procedure involves several cleaning steps. Subsequent high-temperature annealing of the substrates under continuous flow of a Ar/O_2 (80 : 20) gas mixture at T = 950°C for 2 h induces the reconstruction of the surface. After the thermal reconstruction, a well-ordered step terrace structure is obtained, which is beneficial for the epitaxial growth of high-quality thin films.[127–129]

While ideal STO surfaces show straight step ledges[130], variations in the crystals' surface morphology may naturally occur, which go beyond the differences in step width which considerably hamper the quality and reproducibility of the epitaxial growth. Therefore the quality of each substrate was routinely investigated by AFM imaging after thermal annealing and solely substrates with an atomically flat surface morphology were selected for thin film growth. However, the presence of occasional surface features, such as etch pits is inevitable.

Notably, in a few cases STNNi thin films were deposited on 0.5 wt% Nb-doped strontium titanate substrates (Nb:STO) (*Shinkosha Co. Ltd.*) when a conductive substrate material was required. Furthermore, $NdGaO_3$ (*Crystec GmbH*) substrates were applied for the epitaxial growth of STNNi, when bulk-sensitive analysis of the thin film stoichiometry was performed, to enable the quantification of strontium and titanium cations without a distortion of the results by cations which dissolve from the substrate material.

Preparation of polycrystalline $SrTiO_3$ substrates

STO powder was synthesized by the Pechini method and cylindrical ceramic pellets with ~1 cm in diameter were synthesized as depicted in section 3.1.1. Subsequently, discs of ~2 mm thickness were cut from the pellets. The surface of the oxide discs were polished with SiC paper and subsequently by application of a diamond suspension. The final polishing step was carried out with Al_2O_3 nanopowder. Ultimately, a high-temperature annealing process was applied under contin-

---

[2] The substrate termination was performed by R. Borowski and G. Potemkin (Forschungzentrum Jülich, Peter Grünberg Institut (PGI-7), 52425 Jülich, Germany) whose support is highly appreciated.

Table 3.1: Processing parameters for the preparation of TiO_2-terminated STO substrates.

Step	Substrate processing
1	Brush substrates in acetone and sonicate for 3 min
2	Transfer wet substrates in isopropyl, sonicate for 3 min
3	Dry substrates with pressurized nitrogen
4	Transfer substrates in ultrapure H_2O, sonicate for 3 min
5	Transfer substrates in a Teflon jar half-filled with BHF
6	Dispose excess BHF and transfer substrates in a water bath
7	Rinse with water for 3 min
8	Dry substrates with pressurized nitrogen
9	Transfer substrates in acetone and sonicate for 2 min
10	Transfer substrates in isopropyl and sonicate for 2 min
11	Dry substrates with pressurized nitrogen
12	Annealing under Ar / O_2 (80 : 20) gas flow, T = 950°C for 2 h

uous flow of a Ar / O_2 (80 : 20) gas mixture at T = 950°C for 2 h and the surface quality was investigated by AFM.

Epitaxial growth

Two different PLD systems were used for the thin film growth throughout this work. Here all parameters were kept as equal as possible. The thin film deposition was carried out at an oxygen background pressure of $p(O_2) = 0.108$ mbar and a temperature of T = 650°C - 730°C. For the deposition of stoichiometric STNNi thin films a laser fluence of about $F = 1.14\,\mathrm{J{\cdot}cm^{-2}}$ was applied. A KrF excimer laser with a wavelength of $\lambda = 248$ nm was used for the ablation of the spinning ceramic target (5 RPM). The laser was operated with a repetition rate of $f = 5$ Hz. After the growth process, the sample temperature was typically quenched down to room temperature in deposition conditions. Notably, a post-annealing procedure at deposition conditions was performed for samples discussed in chapter 4 and chapter 5. Furthermore post-annealing at a temperature of T = 400°C was applied for individual samples or sample series, as will be stated where relevant. In order to tune the stoichiometry of the epitaxial layers the deposition was performed with a laser fluence in the range between $F = 0.88\,\mathrm{J{\cdot}cm^{-2}}$ - $1.44\,\mathrm{J{\cdot}cm^{-2}}$ (*cf.* chapter 5).

The main difference between both PLD systems that has proven relevant for the comparability of the sample behavior is the type of substrate heating. Here, the *Surface GmbH* setup is equipped with a IR-diode laser with a wavelength of $\lambda = 925$ nm, while the substrates were heated by a resistive heater in the *Twente solid state technology - TSST* setup. The cooling rate depends strongly on the heating method, where laser-heating allows to rapidly quench the sample temperature down from deposition conditions to room temperature in about ~ 1 min, while resistive heating relies on a cooling rate of about $\sim$ 50°C / min. As will be discussed in detail in chapter 7 of this thesis, the thermal history impacts the exsolution response and therefore, the relative comparison of the exsolution behavior is only rational when comparing samples of equal treatment. Additionally a slight difference in the target-to-substrate distance needs to be noted, which was $d = 57\,\mathrm{mm}$ for the *Surface GmbH* PLD setup, while it was $d = 60\,\mathrm{mm}$ for the *TSST* setup.

3.1.3 Thermal annealing

Exsolution processes are typically induced *via* a reducing treatment, *i.e.* thermal annealing in reducing environment. Therefore, methods for the control of the oxygen chemical potential are applied, that are based on the control of the ambient oxygen partial pressure at elevated temperatures. When changing the oxygen partial pressure from standard conditions, the solid material is forced to adjust with respect to the new oxygen chemical potential in order to re-establish equilibrium conditions. In consequence, the oxygen stoichiometry may be changed or phase transitions may be induced. Elevated temperatures are required for the kinetic activation of the defect equilibria that provide the basis for sufficient mobility of the involved ionic species and hence for the stoichiometric adjustment of the material.

Experimental details

In general, two different methods are used to control the oxygen chemical potential. On the one hand, the samples are annealed at controlled oxygen partial pressures in the PLD system for mild oxidation. The system offers direct measurement of the ambient pressure and after evacuation of the PLD chamber, a continuous flow of oxygen gas can adjusted to maintain a constant oxygen pressure. On the other hand, chemical reduction with 4% H_2 / Ar gas is performed. Here, the inert Argon fraction displaces oxygen from the sample environment, which results in a decrease in the oxygen partial pressure. Moreover, the reactive hydrogen fraction directly interacts with oxygen to form H_2O which results in a further decrease of the oxygen chemical potential.

For this purpose thermal annealing is performed in a tube furnace which allows for the direct transfer of samples from a cool zone (room temperature) into the heating zone and *vice versa* using a sample slide. The main tube and the slide are made from quartz glass, where a grommet enables to change the sample position using a platinum wire. The annealing atmosphere is controlled by means of a mass-flow controller. Typically, a gas flow of 50 sccm was used. The setup hence ensures rapid heating and cooling rates, which enables freezing of the equilibrium defect concentrations established under the respective annealing conditions. Notably, reproducibility of the applied conditions was ensured by occasional measurements of the oxygen partial pressure using an oxygen sensor (*Zirox GmbH*).

Similarly, *in-situ* techniques that are used for the investigations of redox reactions offer control of the sample temperature and the ambient atmosphere. Here, annealing in a 4% H_2 / Ar gas mixture was performed for high-temperature X-ray diffraction while vacuum annealing in hydrogen was performed during near ambient pressure X-ray photoelectron spectroscopy as well as grazing incidence X-ray scattering analysis.

3.2 Characterization techniques

Many of the methods depicted below are based on the interaction of electromagnetic waves and particles with the heterogeneous electron distribution related to the ordered atoms or with the atomic nuclei of a sample. For the different analysis principles, electromagnetic radiation may be either considered as waves or particles to make use of different mechanisms of interaction between radiation and matter for the analysis of specific material properties.

The kind of interaction of the photons, electrons and ions used to probe the material strongly depends on the measurement conditions, such as their wavelength or the incident angle and the control of their properties enables to obtain specific qualitative and / or quantitative information about a sample.

Here the energy of photons is given by Planck's equation 3.1

$$E = h \cdot \nu = \frac{h \cdot c}{\lambda} \tag{3.1}$$

where E is the photon energy, h is Planck constant, ν is frequency, c is the speed of light and λ is the wavelength. The wavelength of photons is hence given by equation 3.2

$$\lambda = \frac{h \cdot c}{E} \tag{3.2}$$

The wavelength of a particle with the charge q is related to it's kinetic energy. The kinetic energy E_{kin} of a charged particle that is accelerated by a defined electric field E_{acc} is given by equation 3.3

$$E_{\mathrm{kin}} = \frac{1}{2} m \cdot v^2 = q \cdot E_{\mathrm{acc}} \tag{3.3}$$

where m is the particle mass and v is the velocity of the particle. The wavelength is given by the de Broglie relation 3.4

$$\lambda = \frac{h \cdot c}{p} = \left(\frac{h}{2 \cdot m \cdot q \cdot E_{\mathrm{acc}}} \right)^{1/2} \tag{3.4}$$

where p denotes the particle momentum.[131]

3.2.1 Imaging techniques

Atomic force microscopy

Atomic force microscopy (AFM) was carried out in tapping mode (AC-mode) to investigate the surface morphology of each substrate and thin film sample (*Cypher AFM, Oxford Instruments Asylum Research Inc.*). Here, a sharp silicon tip is used to probe the surface on the basis of repeated line scans across the surface (Fig. 3.4). The tip oscillates close to its' resonance frequency, where the basis remains at a fixed distance relative to the sample. The oscillation is recorded on the basis of a reflected laser beam by means of a multiple segmented photodiode. Here, the characteristic phase and amplitude of the oscillation is sensitive to the interaction between the surface atoms and the tip, where attractive Van-der-Waals forces (for increasing distances) and Coulomb repulsion (for decreasing distances) contribute to the modulation of the recorded signal. The difference between the drive oscillation and recorded oscillation provides information about the surface topography.[132]

Silicon tips with a curvature $< 8\,\mathrm{nm}$ were used for the surface analysis. Here, typically a scan frequency in the range between 1.0 - 1.7 Hz was used to record images with a number of 512 scanned lines. Based on the topological data the surface characteristics were analyzed with particular focus on the nanoparticle properties exsolved at the crystal surface using *Gwyddion* version 2.52. Here, plane levelling and the align rows (median) function were applied and the (z)-zero level is set on top of a step terrace before thresholding of 1 nm was used to detect nanoparticles with a specific height on top of the crystal surface (exceptionally 10 nm in chapter 5). Subsequently, the grain statistics function was used to export the nanoparticle number, nanoparticle radius, nanoparticle height as well as the nanoparticle volume.

For statistical evaluation of the nanoparticle characteristics three AFM scans were performed at different locations of each sample and averaged values of the particle

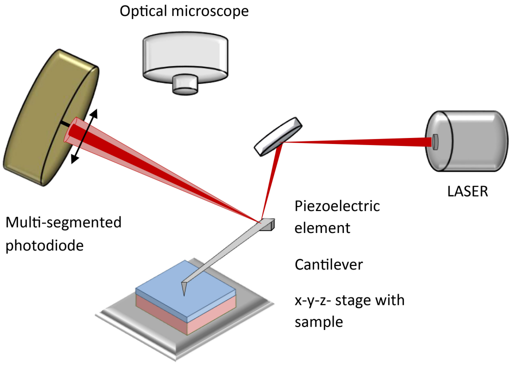

Figure 3.4: Schematic illustration of an atomic force microscope.

properties were calculated (average particle number, average sum of the nanoparticle volume, median diameter, median height). The error calculated based on the standard deviation of three measurements.

Scanning electron microscopy

Scanning electron microscopy (SEM) is applied to study the surface morphology of polished ceramics and polycrystalline, epitaxial thin films. A focused electron beam is scanned across the sample surface that interacts with the sample where different types of secondary signals are generated. Common analysis modes are based on the detection of secondary electrons (SE) that are emitted from the atoms of the sample due to excitation with the primary electrons or backscattered electrons (BE) resulting from elastic scattering events. Among other parameters, the signal depends on the topography of the sample and can be used to resolve features on the nanometer scale.[133]

The polished surface of STNNi oxide ceramics was investigated in SE detection mode with an acceleration voltage of 5 kV (*SU 800, Hitachi High-Technologies Corporation, Japan*). The surface of polycrystalline epitaxial thin films was analyzed after evaporation of a thin conductive carbon layer with an acceleration voltage between 10 kV - 20 kV (*Zeiss Cross Beam XB540*).

Transmission electron microscopy (TEM, TEM-EDXS, TEM-SAED)

Transmission electron microscopy (TEM) is used to investigate the structural properties of the oxide samples. Here, the sample is irradiated with an electron beam. The electrons are partially scattered during the transmission through the sample, where the electrons that emerge from the exit surface of the sample are detected. To this end, thin lamellae of the material are prepared by a focused ion beam, that allow for the transmission of electrons with sufficient intensity.

Generally, TEM is operated either in imaging mode or diffraction mode, where the imaging mode is controlled by modifications of the electron beam path. In imaging mode a contrast image is recorded which is based on the spatial distribution of the scattered electrons and that reflects the atomic ordering of the sample. In diffraction mode, the electron diffraction pattern, *i.e.* the angular distribution of the scattered electrons is recorded. The scattering processes strongly depends on the sample thickness as well as the atomic number of the nuclei and therefore on the elemental composition and structural ordering of the atoms.[131]

In contrast to conventional TEM using a parallel electron beam, scanning transmission electron microscopy (STEM) is performed by scanning the sample with a focused electron beam. Scanning of the focused primary electron beam enables the simultaneous chemical analysis and correlation of the structural and chemical information (elemental mapping). High-angle annular dark-field imaging (HAADF) enables structural investigations on the atomic order. Here, electrons that are scattered to large angles are detected in order to record Z-contrast images where the imaging contrast is directly correlated to the atomic number Z.[131, 134]

Selected area electron diffraction

Selected area electron diffraction (SAED) is applied to laterally resolve the structural properties of a sample based on the investigation of the electron diffraction pattern. Here, an aperture is used to restrict the electron beam to a specific region of the sample.

Energy-dispersive X-ray spectroscopy

Energy-dispersive X-ray spectroscopy (EDXS) is carried out to investigate the elemental composition during STEM investigations. Here, the excitation of sample electrons from their ground state to states of higher energy is induced by the focused electron beam. The energy difference is emitted in form of photons during transfer from the excited state and the ground state. The element-specific emission spectrum is detected and utilized for the analysis of the (lateral) elemental composition of a sample.

Experimental details

The samples were typically covered with 30 nm of evaporated Pt prior the FIB preparation in order to minimize surface amorphization due to beam damage. The ceramic samples were analyzed with an acceleration voltage of 200 kV (*Tecnai G2 F20 S-Twin, Thermo Fisher Scientific*). Furthermore, EDXS was performed to analyse the elemental composition at different locations of the sample. The epitaxial thin films were investigated in zone-axis using high-angle annular dark-field imaging mode (*FEI TitanG2 80-200 ChemiSTEM*). The microscope was equipped with a high-brightness field emission gun, a spherical aberration corrector for the probe forming lens, and a *super-X EDS* system. The convergence semi-angle for HAADF imaging was about 25 mrad, while the collection semi-angle was 70 - 200 mrad. The TEM dark-field images and selected area electron diffraction patterns were recorded in an *FEI Tecnai F20 microscope*. Both microscopes were operated with an acceleration voltage of 200 kV.

STEM (EDXS, SAED) analysis of the epitaxial thin films was preformed at Forschungszentrum Jülich (ER-C) in collaboration with L. Jin. STEM (EDXS) analysis of the ceramic samples was performed at RWTH Aachen (GFE) and was supported by K. Kistermann, S. Zischke and C. Herwartz.

3.2.2 Diffraction and scattering analysis

X-ray diffraction and electron diffraction can be used to study the (bulk) crystallographic properties of the samples. Additionally, scattering techniques which operate in non-Bragg conditions enable the investigation of the surface properties of nanostructured materials. Furthermore, (back) scattering of electrons and ions can be used to study the crystallographic (surface) orientation or elemental composition of a material.

X-ray diffraction analysis

The diffraction of waves by periodically ordered crystallographic planes is described by Bragg's law

$$n \cdot \lambda = d_{(\mathrm{hkl})} \cdot 2 \cdot sin(\theta) \tag{3.5}$$

where n is the diffraction order, λ is the wavelength and θ is the incident angle of the radiation and $d_{(\mathrm{hkl})}$ is the lattice spacing of the crystallographic planes. Waves that are coherently scattered at adjacent crystallographic planes of a crystal exhibit a difference in phase (Fig. 3.5). In consequence, constructive and destructive interference results in distinct diffraction signals. The measurement of the diffraction pattern therefore can be utilized to investigate the crystallographic structure and to the determine the lattice parameters of crystalline materials.

The crystallographic properties of the oxide powders and oxide ceramics were investigated by X-ray diffraction (XRD) using a Cu-K_α anode (*D4 Endeavor, Bruker*). For this purpose, the oxide powders were dispersed on a glas plate using double-sided adhesive tape. The XRD measurements were carried out in 2θ-ω geometry with a measurement increment of 0.02°.

XRD analysis of the epitaxial thin films was performed using a XRD setup equipped with a Cu-K_α anode, a goebel mirror, a monochromator, a centric eulerian cradle and a LYNXEYE XE detector (*D8 Discover, Bruker AXS GmbH*). Usually, a pinhole adapter with a diameter of 2 mm was used to focus the incident X-rays central on the thin film samples. The thin films were aligned with respect to the sample height (z), rotation (Φ) and tilt (Ψ) of the sample using rocking curve analysis in the vicinity of the (002) diffraction peak of the substrate. All measurements were performed in the high-resolution mode.

Measurements were typically performed with a divergence slit of 0.6 mm on the primary side. The width of the motorized secondary slit was set to 0.8 mm. The linear opening of the LNYXEYE detector was set to 0.6 mm which equals 8 channels of the detector array. A measurement increment of 0.01° was used for measurements in 2θ-ω geometry, while the measurements were performed with a time of 1 s/step. For XRD rocking curve analysis the 2θ and ω position of the motors were aligned to the maximum of the (002) thin film signal. The rocking curve measurements were performed with an increment of 0.001° while a the measurement time was set to 0.5 s/step. Both, 2θ-ω and rocking curve measurements were carried out in

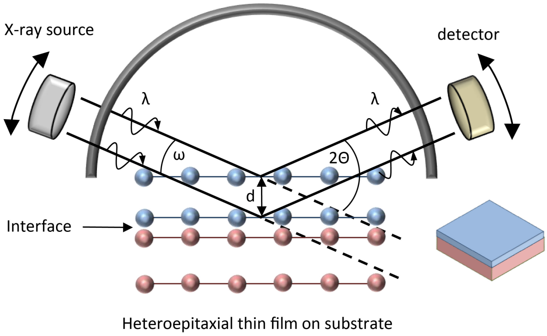

Figure 3.5: Schematic illustration of X-ray diffraction in Bragg condition.

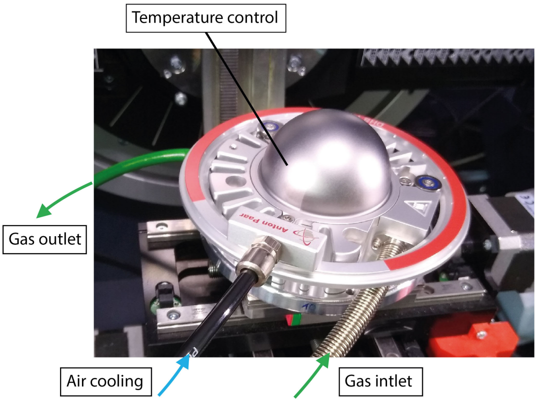

Figure 3.6: High-temperature XRD setup. The sample is located on a ceramic plate which is heated from the backside and covered by the graphite dome. Pressurized air is used for temperature control. The ambient atmosphere is controlled by continuous flow of O_2 or 4% H_2 / Ar gas.

0D detector mode. Reciprocal space mapping (RSM) around the asymmetric (013) diffraction peak were carried out in grazing exit geometry using the 1D-detector mode. Here, the motorized secondary slit (9.5 mm) and the linear opening of the detector was fully opened (14.325 mm).

In-situ high-temperature X-ray diffraction analysis (HT-XRD) was performed by using a closed graphite chamber (*Anton Paar DHS 1100 Domed Hot Stage*) which offers temperature and gas control (Fig. 3.6). For this purpose, the thin film samples are placed on a single-crystalline MgO substrate that was located on the ceramic plate of the HT-stage. Backside heating of the ceramic plate and air cooling was used to control the sample temperature. During the measurement a constant gas flow of 0.1 LPM was applied to control the ambient atmosphere while the dome was purged with an increased flow rate of $\sim$5 LPM to provide for a fast gas exchange to initiate sample reduction. The sample was aligned with respect to the (002) substrate diffraction signal (room temperature value).

Electron backscatter diffraction (EBSD)

Electron backscatter diffraction (EBSD) is a SEM-based technique for the analysis of the crystallographic orientation of crystals. The technique is based on the detection of the so-called Kikuchi pattern which emerges upon the diffraction of backscattered electrons that are escaping from the excitation volume of the sample. The Kikuchi lines represent the angular distribution of the backscattered electrons that are emitted from the subsurface region of the sample. The Kikuchi patterns, that are recorded at the surface of the different oxide grains of a sample can be used to construct an orientation map, which shows the crystallographic orientation of the grain and hence the surface orientation of the grains.[133, 135] Orientation mapping by EBSD was performed to study the surface orientation of the crystal facets of the epitaxially deposited, polycrystalline STNNi thin films (*Oxford instruments*).

SEM-EBSD analysis of the polycrystalline epitaxial thin films was performed at Forschungszentrum Jülich (IEK-2) in collaboration with E. Wessel.

Low-energy ion scattering

Low-energy ion scattering (LEIS) is based on the detection of ions after scattering of the primary ions and sample atoms at the near-surface region. Information about the elemental composition of the outer surface (high surface sensitivity) is based on (elastic) binary collisions with surface atoms which results in the detection of distinct surface peaks. The energy of the backscattered ions which is determined by the primary energy, the incident angle and, importantly, the mass ratio of the primary ion and the probed atom is detected by means of a time-of-flight analyzer. [136, 137]

LEIS analysis of the as-prepared STNNi surface of thin films with thicknesses of 20 nm, 50 nm and 100 nm was performed. The system was operated with normal incidence of 3 keV He^+ a primary beam source (*Qtac100, IONTOF GmbH*). The analysis area was 1000 x 1000 μm^2. Prior to the measurement, the analysis areas was cleaned by Ar^+ sputtering in order to remove adsorbed carbon species with a dwell time of 5 s. The sputter area was 1500 x 1500 μm^2. A flood gun was used during the analysis. The relative peak areas were determined by using *CasaXPS* after subtraction of a Shirley-type background. The intensity was normalized to the Sr signal.

The oxygen exchange analysis was performed at Imperial College London in collaboration with A. Aguadero, A. Cavallaro and S. Fearn.

Simultaneous near ambient pressure x-ray photoelectron spectroscopy and grazing incidence x-ray scattering

Coupled *in-situ* NAP-XPS and *in-situ* grazing incidence X-ray scattering (GIXS) analysis was developed by the group of Slavomir Nemšák at *Advanced Light Source - Lawrence Berkeley National Laboratory* for the simultaneous analysis of chemical and structural sample properties.[138] The specific geometry of the setup allows to utilize the incoming X-ray beam for scattering analysis as well as for the generation of photoelectrons, where the scattered signal and the photoelectron spectrum is detected simultaneously. For these synchrotron-based measurements, the X-rays are generated by controlled deflection of the circulating electrons or positrons in the storage ring, *e.g.* by a bending magnet or an undulator.

Here, scattering can be utilized to investigate the properties of nanostructured surfaces and based on the interaction of X-rays with the heterogeneous electron density of nanometric objects.[139, 140] Photoelectron spectroscopy is used to simultaneously obtain information about changes in the surface chemistry as depicted below.

The NAP-XPS / GIXS analysis was performed at Advanced Light Source - Lawrence Berkeley National Laboratory in collaboration with H. Kersell and S. Nemšák.

3.2.3 X-ray photoelectron spectroscopy

X-ray photoelectron spectroscopy (XPS) was carried out for the evaluation of the surface stoichiometry of the oxide samples as well as for the investigation of the Ni oxidation state. Additionally, *in-situ* spectroscopy is used to investigate the dynamics of metal exsolution on the basis of relative changes in the Ni oxidation state over time and for probing the formation of surface space charge regions at the surface of STNNi thin films.

XPS is based on the photoionization of elements and the detection of the kinetic energy of the generated photoelectrons, which provides information about the electronic structure of materials. The specific binding energies (B.E.) and relative peak areas of the XPS signals can be used for the qualitative and quantitative analysis of elements and, importantly, provides information about the chemical state of an analyte.

X-rays are generated by scanning an Al anode with an electron beam and subsequent monochromization of the characteristic X-ray spectrum and Bremsstrahlung (Fig. 3.7). The X-rays are focused on the sample and photoelectrons are extracted in a defined angle with respect to the surface and transferred into the spherical capacitor analyzer. The photoelectrons are separated with respect to their kinetic energy, where a multi-channel plate serves as a detector. A turbo pump provides for ultra high vacuum conditions.

The photoelectrons are extracted close to the sample surface and transferred to a spherical capacitor analyzer coupled with a multi-channel plate detector, where electrons of different kinetic energies are sequentially analyzed. Based on the energy of the X-rays and the detected kinetic energy E_{kin} of the photoelectrons, the binding energy can be determined by equation 3.6.

$$B.E. = h \cdot v - E_{\mathrm{kin}} - \Phi \tag{3.6}$$

Here h is Planck constant, v is the frequency of the X-ray photon, and Φ is the work function of the analyzer.

For the *in-situ* investigation of redox processes at the sample surface, near ambient pressure X-ray photoelectron spectroscopy (NAP-XPS) is carried out. The system offers a heated sample stage as well as supply of oxygen and hydrogen gas to drive reactions at elevated temperature (Fig. 3.7). The gas supply requires differential pumping of the analyzer *via* a small nozzle placed in close vicinity of the sample. This allows sufficient yield of photoexcited electrons from the sample and to avoid undesired scattering events of extracted electrons and gas atmosphere.[141]

The chemical shift, *i.e.* the shift in the binding energy of XPS signals in reference to the signal of the pure element provides information about the chemical and electronic state and hence the chemical environment of an element. The chemical shift depends on the electron density present during the photoionization and hence the chemical properties of an element. Here, chemical bonds result in charge transfer, where the electronegativity of the binding partner considerably influences the nature of the chemical shift. For instance, oxidation of a metal results in the transfer of the electron density towards the oxygen bond of high electronegativity. In consequence, the attractive interaction between the remaining electrons of the cation becomes stronger (Coulomb attraction) which results in a chemical shift towards higher binding energies. Therefore, XPS signals of a specific core-level spectrum obtained from metal species (*e.g.* Ni) are typically observed at lower binding energies relative to their oxide counterparts (*e.g.* NiO). Quantitative analysis of species is typically based on the relative peak areas of core-level spectra.

Furthermore, a shift in the binding energy may result from uncompensated charging of the sample. Extensive charging may occur for samples of low conductivity, where the compensation of photoelectrons by supply of electrons from the bulk is slow which results in the establishment of a positive charge in the surface region. Here, a rigid shift of all core-level signals can be expected since the charge affects all photoelectrons leaving the surface of the sample to ambient. However, a rigid shift in the binding energy may also originate due to the formation of a space charge zone at the surface of oxide samples elevated temperatures. Here, the nature of the surface potential depends on the doping level and, remarkably, depends on the ambient redox conditions. The magnitude of the surface potential and therefore the B.E. shift is a function of the oxygen partial pressure. For donor-doped STNNi, typically a shift of Δ B.E.. $\sim 0.7\,\mathrm{eV}$ is induced by the establishment of a space charge region under oxidizing conditions.[111, 142]

The surface stoichiometry was analyzed on the basis of the relative peak areas of the XPS Sr $3d$, Ti $2p$, Nb $3d$, Ni $2p$ and O $1s$ core-level spectra after subtraction of a Shirley type background. For quantification, relative sensitivity factors (RSFs) were referenced to the ceramic target. Binding energies of all spectra were

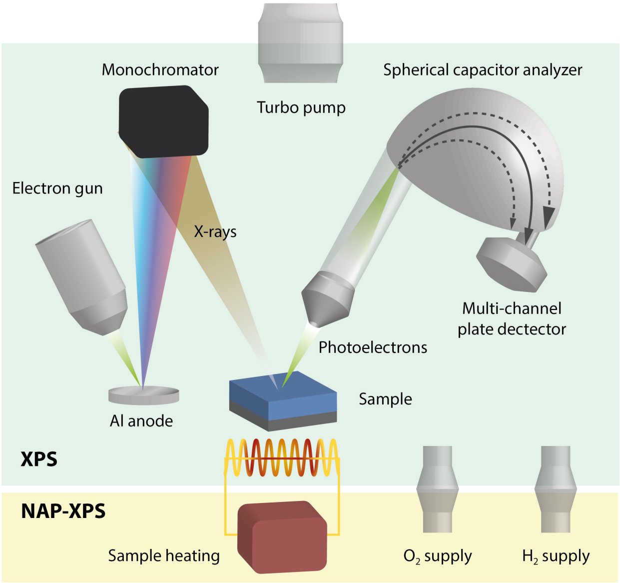

Figure 3.7: Schematic illustration of a XPS / NAP-XPS setup. The ionization process is induced by focused, monochromatic X-rays. Photoelectrons are detected with respect to their kinetic energy. For *in-situ* NAP-XPS measurements a heated sample stage allows for measurements at elevated temperatures. Furthermore, oxygen and hydrogen supply enables to drive redox reactions during the accumulation X-ray photoelectron spectra at low ambient gas pressures.

aligned to the C 1*s* signal. The measurements were performed using the Al Kα line (E_λ = 1486.6 eV, FWHM = 0.26 eV) of a monochromatized X-ray source and at a photoemission angle of 15° as well as constant pass energy (E_0 = 29.35 eV) in the fixed analyzer transmission mode (*Phi5000 VersaProbe, ULVAC Phi, Physical Electronics Inc.*).

In-situ spectroscopy was performed using a custom-designed laboratory-based XPS (*Specs Surface Nano Analysis GmbH*). Here, XPS core-level spectra were recorded during exposure of the samples to hydrogen or oxygen gas at a constant temperature of T = 400°C after a short heat-up of each sample to T = 500°C under oxygen atmosphere to remove adsorbed carbon species. The binding energy of the XPS spectra (if applied) was corrected to the Ti 2*p* position B.E. = 458.4 eV. The intensity was normalized to the pre-peak region. In case the surface potential-dependent binding energy shift was investigated, no binding energy correction was performed. Typically, 50 scans were averaged for each Ni 2*p* spectrum shown in chapter 6 and chapter 7. In a few cases, a smaller number of scans was used owing to slight shifts in the sample position over long probing times, in order to avoid a decreased signal-to-noise ratio. The core-level spectra were recorded with a pass energy of E_0 = 20 eV, a step size of 0.05 eV, a dwell time of 200 ms and with a spectral resolution of 0.8 eV. The *CasaXPS* and *SpecsLab Prodigy* software packages were used for the evaluation of the XPS data.

The NAP-XPS analysis was performed at Charles University Prague in collaboration with by B. Šmíd.

3.2.4 Quantitative bulk analysis

Inductively coupled plasma mass spectrometry (ICP-MS) and inductively coupled optical emission spectroscopy (ICP-OES) are techniques for the elemental quantification of liquid samples. Both techniques are relative analysis techniques, where typically an external calibration is performed by using a multi-element standard solution. The liquid sample is introduced in form of a fine dispersion into an argon plasma, generated by means of a high frequency induction coil. For ICP-MS analysis, the plasma plume serves for the evaporation, atomization and ionization of the sample compounds. The generated ions are transferred to a mass spectrometer, where they are separated according to their mass-to-charge ratio and detected by means of a mass-spectrometer (*e.g.* quadrupole). In comparison, the plasma plume is used in ICP-OES analysis for the excitation of electrons of the sample atoms into higher energy states. Relaxation in to the initial state results in the emission of photons of specific wavelengths that are characteristic for the electronic structure of the elements. The quantification is based on the intensity of element-specific emission lines relative to a standard solution of known element concentration.[143]

Due to its higher sensitivity and lower detection level, ICP-MS is typically used for the low concentration regime (trace analysis regime), while ICP-OES exhibits a higher detection limit and is therefore typically used for solutions of larger analyte concentrations.[144] Accordingly, ICP-MS (*Agilent 7500ce*) was used for the analysis of epitaxial thin films and ICP-OES (*iCAP7600, Thermo Scientific*) was applied for the analysis of oxide ceramics (bulk). For this purpose, [001]-oriented STNNi thin films were deposited on (110) $NdGaO_3$ substrates (*CrysTec GmbH*). The thin film material were dissolved in a mixture of HCl / H_2O_2 (volume ratio of 3 : 1) for 2 h at a temperature of T = 50°C. Three aliquots of the solution were analyzed for each sample, respectively. In order to dissolve ceramic samples, a fusion of the material with lithium borate was prepared in a Pt / Au crucible for 30 min at T= 1000°C. Subsequently, the product was dissolved in a mixture of HCl / H_2O_2 (volume ratio of 3 : 1). Before the analysis, the samples were diluted using deionized water. The ICP-OES and ICP-MS analysis were performed at Forschungszentrum Jülich (ZEA-3) with support of V. Nischwitz.

3.2.5 Secondary ion mass spectrometry

The cation distribution as well as the isotopic fraction of ^{18}O tracers (after oxygen exchange experiments) was investigated by secondary ion mass spectrometry (SIMS). Here a primary ion beam is focused on the sample to generate secondary ions of the material. The generated ions are extracted and analyzed on the basis of their mass-to-charge ratio by means of a time-of-flight mass spectrometer. The measurement of depth-profiles is performed by using an additional ion source for sputtering through the sample material. Here, alternating ion pulses from the sputter source and the primary ion source enables to record a depth-resolved mass-spectrum which provides information about the elemental and isotopic composition of an material across the sample thickness.

Cation distribution

The cation distribution across the thickness of the epitaxial thin films, presented in chapter 4 and chapter 6 was analyzed by depth profiling after a 30 nm Pt protection layer was evaporated on the surface using negative polarity mode (*ToF-SIMS 5.NCS, IONTOF GmbH*). Here, Ti^+, $^{86}Sr^+$, Ni^+, Nb^+ and Pt^+ signals were extracted from the data. The SIMS analysis of cation depth profiles analysis were performed at Forschungszentrum Jülich (ZEA-3) in collaboration with U. Breuer.

Oxygen exchange experiments

In a first step, the 100 nm thick STNNi and STNi thin film samples were equilibrated in $^{16}O_2$ gas. For this purpose the samples were placed in a quartz tube which was evacuated to $p < 10^{-7}$ mbar and subsequently filled by $^{16}O_2$ gas ($p = 200$ mbar). For equilibration a thermal annealing was performed at $T = 400°C$. In a second step, the gas environment was changed to $^{18}O_2$ enriched oxygen gas, without exposing the samples to air, and a thermal annealing step was carried out for different exchange times of 20 min, 100 min and 200 min. The equilibration step was performed for $t_{\mathrm{equilibration}} > 10 \times t_{\mathrm{exchange}}$, respectively. To ensure fast heating and cooling rates, the samples were transferred directly into the hot zone of the furnace and were transferred to the cool zone (room temperature) of the furnace for quenching down the sample temperature after the exchange experiment.

To investigate the exchange kinetics SIMS depth profiling was carried out with positive polarity and using burst mode[145]. Depth-profiles of $^{16}O^-$, $^{18}O^-$ (and Ni^-, NiO^-, NbO^-, SrO^-, TiO^-) were extracted. The measurements were performed with 1 keV Cs^+ primary ions mode using a flood gun for charge compensation. An argon cluster beam was used for sputtering of the material. For depth-profiling a sputter area of $300 \times 300\ \mu m^2$ and an analysis area of area of $100 \times 100\ \mu m^2$ was used.

For the evaluation of the tracer fraction $C'(x, t)$ incorporated in the samples during oxygen exchange, the measured tracer fraction $C(x, t)$ was corrected by the background concentration (natural abundance C_{bg} = 0.2 % and the isotope enrichment C_{g} = 83.45 % of the gas used for the exchange experiments. The ^{18}O isotope enrichment of the $^{18}O_2$-rich gas was determined by annealing a silicon wafer at T = 1000°C for 8 h and subsequent determination of the ^{16}O / ^{18}O ratio by SIMS analysis. The sputter depth was calculated from the sputter time by normalization to the sample thickness (determined by RHEED-analysis) using the nickel dopant profile.

The oxygen exchange analysis was performed at Imperial College London in collaboration with A. Aguadero, A. Cavallaro and S. Fearn.

3.2.6 Vibrating sample magnetometry

The magnetic properties of the epitaxial STNNi thin films were investigated using a vibrating sample magnetometer (VSM) in order to follow the oxide-to-metal transition upon reducing annealing on the basis of the magnetic signature of Ni. Here, the sample is placed in a magnetic field H, resulting in the magnetization of the sample M. Using a vibrating sample holder M can be detected using a pair of sensing coils *via* induction of a an electric field. The magnetic measurements were performed using a *Dynacool Physical Property Measurement System (PPMS) of Quantum Design*. Full hysteresis loops between ± 10 kOe were measured, and a linear background was subtracted to correct for the diamagnetic contribution of the STO substrate. The VSM analysis was performed at Forschungszentrum Jülich (PGI-6) in collaboration with M. Wilhelm.

Chapter 4

Synthesis, structural properties and exsolution response of STNNi

This chapter deals with the synthesis and the structural properties of exsolution-active STNNi ceramics and epitaxial thin films. Based on a systematic variation of the Ni-doping concentration, the B-site substitution level is investigated with respect to phase purity, and the solubility of nickel within the strontium titanate host lattice is discussed. The exsolution activity of the material is demonstrated for the ceramic samples and the oxide thin films and characterized in detail on the basis of the epitaxial model systems. Here, nanoparticle exsolution is addressed by comparison of the as-prepared and reduced state of the oxide thin films in terms of morphological evolution, structural relaxation, stoichiometry changes and the metallic character of the nanoparticles. Please note that the data discussed in this chapter was partly published in [146] and [147].

4.1 Sintered ceramics

Strontium titanate powders of different doping compositions with the general chemical formula $SrTi_{1-(z+x)}Nb_zNi_xO_{3-\delta}$ were synthesized by the Pechini method and the mixed oxide route (MOR). Based on the powders, ceramic pellets were sintered which were used to confirm the exsolution activity of the material. The details on the synthesis process are given in section 3.1.1.

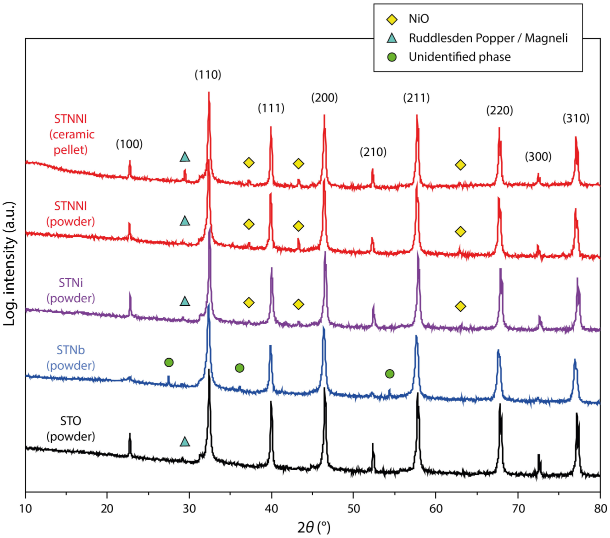

Figure 4.1: X-ray diffraction analysis of $SrTiO_{3-\delta}$ (STO), single-doped $SrTi_{0.95}Nb_{0.05}O_{3-\delta}$ (STNb) and $SrTi_{0.95}Ni_{0.05}O_{3-\delta}$ (STNi) as well as $SrTi_{0.95}Nb_{0.05}Ni_{0.05}O_{3-\delta}$ Nb- and Ni-(co)-doped strontium titanate (STNNi) powders prepared by Pechini synthesis. The diffractogram obtained from a sintered ceramic STNNi pellet fabricated from the co-doped Pechini powder is shown above. While all powders exhibit a predominant diffraction signature of the perovskite structure, several diffraction signals which are not related to the main perovskite phase are detected. Cyan-colored triangles indicate the presence of Ruddlesden-Popper / Magneli phases, green circles denote the presence of an unidentified (presumably Nb-rich) phase. A small fraction of NiO present as secondary phase is visible for STNi and STNNi as denoted by yellow rhombi.

Phase analysis

The crystallographic properties and phase purity of the synthesized powders and ceramic pellets were investigated by XRD analysis. Fig. 4.1 shows XRD diffraction patterns obtained from strontium titanate powders, co-doped by Nb and Ni (STNNi), as well as single Nb-doped STO (STNb), single Ni-doped STO (STNi) and undoped STO powder, which were synthesized by the Pechini method. A diffractogram obtained from the sintered ceramic STNNi pellet is shown as a reference. As can be seen, the oxide samples crystallize in the perovskite structure with the space group Pm3m. The Miller-indices assigned to the respective diffraction peaks are given in the figure. The formation of minor secondary phases is evident as reflected by additional diffraction signals of low intensity, which become visible on the logarithmic intensity scale. For instance, a small diffraction peak at $2\theta \sim 29.5°$ is visible for all samples (denoted by cyan-colored triangles) which was reported to be related to the formation of a small fraction of Ruddlesden-Popper (RP) and Magneli-phases in oxidizing conditions.[148]

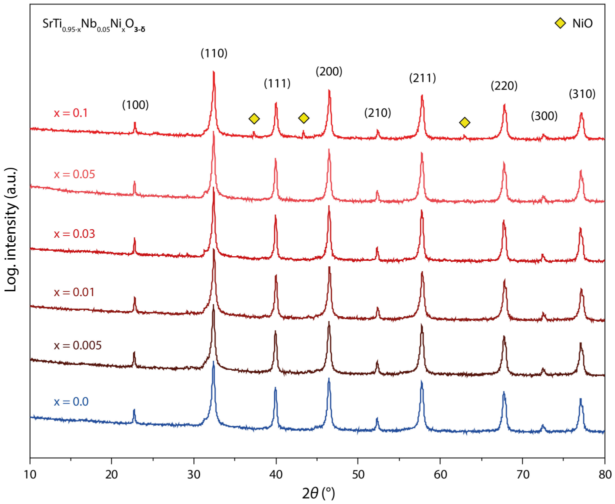

Figure 4.2: X-ray diffraction analysis of sintered ceramics of SrTi$_{0.95-x}$Nb$_{0.05}$Ni$_x$O$_{3-\delta}$ with different levels of Ni-substitution in the range between x = 0.0 to x = 0.1. No secondary phases can be observed for Ni-substitution between x = 0.0 to x = 0.05. A small fraction of NiO present as secondary phase is visible for a doping level of x = 0.1 as denoted by yellow rhombi.

Additional diffraction signals are visible in the diffraction pattern obtained from the STNb powder (denoted by green circles). Due to the low intensity of the diffraction signals (close to the signal-to-noise ratio), unambiguous identification of the secondary phase is difficult, however their presence may be related to the oxidizing calcination conditions applied. Typically, calcination under reducing atmosphere is required for (donor-doped) STNb to promote electronic compensation of the donors by the formation of Ti (III) states rather than the introduction of Sr vacancies, which in turn was reported to be the predominant compensation mechanism under oxidizing treatment[149, 150]. The non-ideal synthesis conditions for the donor-doped material are also reflected by a slight broadening of the ABO$_3$ diffraction peaks in comparison to the other perovskite samples as well as by the considerably reduced visibility of low-intensity signals (*e.g.* (210)- and (300)-diffraction peaks) that may indicate low crystallinity of the oxide powder.

Furthermore, the formation of a minor NiO secondary phase is evident for Ni-doped as well as co-doped STO (denoted by yellow rhombi). As can be seen, the NiO secondary phase also remains present after an additional sintering step applied to prepare a dense ceramic pellet. Therefore it appears that the Ni-dopants partly remain in the form of a secondary phase, while the Nb-dopants fully dissolve within the perovskite lattice. Notably, a pronounced RP / Magneli diffraction signal is also visible for the co-doped STO material system. These findings may indicate that charge compensation of Nb-dopants by Sr-vacancies may be preferred over the (intended) compensation by lower-valent Ni (III) dopants under the applied synthesis conditions.

To further investigate the solubility of Ni-dopants in the STNNi material system, a series of ceramic pellets with systematic variation of the Ni-doping level were prepared. In Fig. 4.2 diffractograms obtained from the samples are shown. No secondary phases were detected by XRD for a doping level up to x = 0.05, while a minor NiO phase is visible for samples with a doping level of x = 0.1 as denoted by yellow rhombi. Here, quantitative phase by Rietveld refinement analysis of the diffractogram revealed a NiO secondary phase of $\sim$ 0.4 wt%.[1]

Remarkably, no significant shifts in the position of the diffraction peaks can be observed compared to the purely Nb-doped perovskite (x = 0.0), independent from the Ni-doping level. Consistently, Rietveld refinement of the diffraction data shown in Fig. 4.2 did not reveal a systematic variation in the lattice constants of the ceramic samples with different Ni-doping level. Here, the lattice parameters of all oxide samples were found to be in the range between a = 3.910 - 3.913 Å. The lattice constant of the $\mathrm{SrTi_{0.95-x}Nb_{0.05}Ni_xO_{3-\delta}}$ ceramics is considerably increased compared to undoped $\mathrm{SrTiO_{3-\delta}}$ with a nominal lattice parameter of a = 3.905 Å[151] and is in good agreement with the observation of lattice expansion for Nb-doped strontium titanate[149, 152]. The Nb(V)-cations (r = 0.64 Å) exhibit a larger ionic radius compared to the Ti(IV)-cations (r = 0.605 Å) occupying the B-sites of the host lattice, while the ionic radius of Ni(III)-cations (r = 0.60 Å) is of similar size.[153] Hence, the lattice expansion is likely to mainly originate from a steric effect due to doping with larger niobium cations, while Ni-doping appears to have no measurable effect on the lattice parameter. Considering the electrostatic modifications of the crystal lattice typically involved in doping, the absence of a systematic variation in the lattice parameter of the perovskite depending on the Ni-substitution level is surprising. As a secondary effect, Nb-substitution may result in the formation of Ti(III) valence states (r = 0.67 Å)[153] which further contribute to the expansion of the crystal lattice. This effect might however be partially compensated by Ni doping and depends on the extend of Ni incorporation into the lattice. Notably, no significant differences in the structural properties were detected after additional sintering of the ceramic samples for 120 h.

---

[1] The Rietveld refinement was performed by Y. J. Sohn (Institute of Energy and Climate Research (IEK-1), Forschungszentrum Jülich GmbH, 52425 Jülich, Germany) whose support is highly appreciated.

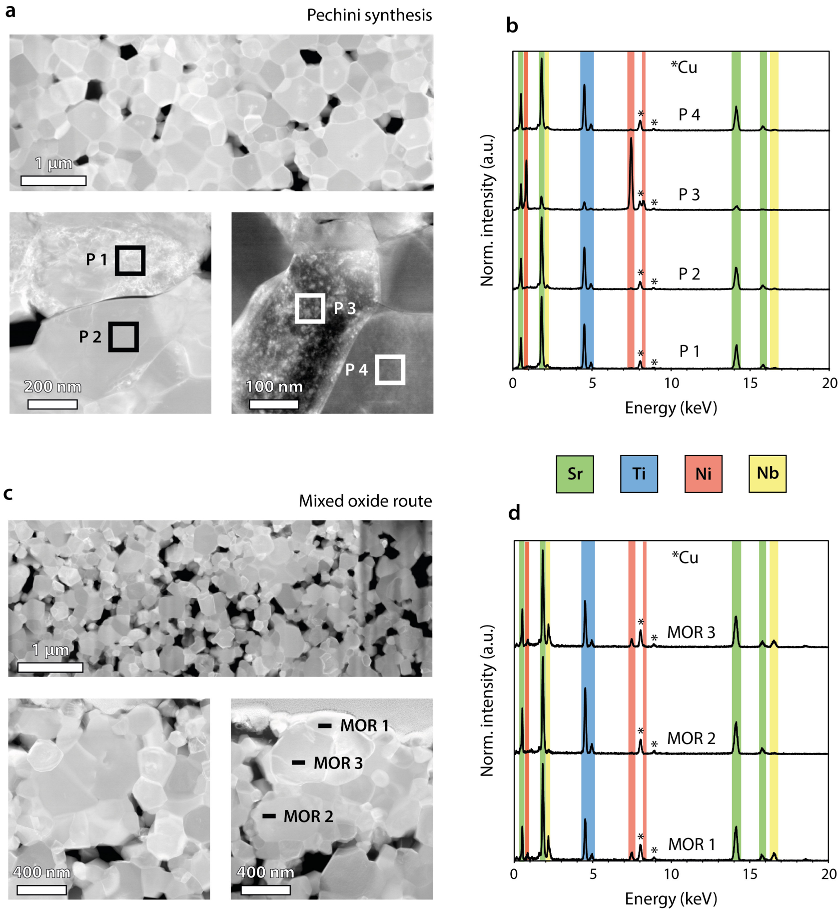

Figure 4.3: Scanning transmission electron microscopy in dark-field imaging mode and energy dispersive X-ray spectroscopy analysis. Investigation of microstructure and elemental distribution of sintered ceramics with a stoichiometry of SrTi$_{0.9}$Nb$_{0.05}$Ni$_{0.05}$O$_{3-\delta}$ obtained by Pechini synthesis (above) and by the mixed oxide route (below). Representative STEM images of are displayed on the left and normalized EDX spectra are given on the right respectively. EDXS measurements are compared for different probing locations.

Investigations of the microstructure and the dopant distribution is performed by TEM / EDXS analysis, comparing $SrTi_{0.9}Nb_{0.05}Ni_{0.05}O_{3-\delta}$ ceramics synthesized by the Pechini route and the mixed oxide route (Fig. 4.3).[2] A porous microstructure is revealed by TEM analysis. Moreover, slight differences in the morphology of different grains can be observed for the Pechini-based oxide ceramics based on the imaging contrast (Fig. 4.3a), where the surface of certain grains exhibit spots and lines which may be related to a high density of dislocations or a rough surface morphology (*cf.* P 1 and P 3, while other grains appear to have a smooth and regular surface P 2 and P 4. Considerable differences in the Ni-signal are detected by measurements of various oxide grains of the ceramic pellet fabricated by the Pechini route (Fig. 4.3b). Here, an increased amount of nickel relative to the other cations of the sample is detected for certain oxide grains, as evident from the relative intensity of the Ni emission peaks (*cf.* scan P 3 *vs.* scans P 1, P 2, and P 4). Correspondingly, a decreased intensity of the Ti- (blue), Sr- (green) and Nb- (yellow) emission peaks is evident. Notably, the Ni-enrichment is not directly correlated to the imaging contrast. Considering the characteristic diffraction signals assigned to a NiO secondary phase, as discussed above, the Ni-rich grains can be identified as NiO. The porous microstructure of the MOR ceramic sample exhibits a comparably lower grain size distribution (Fig. 4.3c). In comparison only small inhomogeneities in the dopant distribution are detected by TEM / EDXS investigations of the sample (Fig. 4.3d). However, also for the MOR sample certain oxide grains appear to be partially depleted from Ni- and Nb- dopants (*cf.* MOR 2) in comparison to other grains of the same sample (*cf.* MOR 1, MOR 3).

Conclusions

The analysis of ceramic STNNi samples has shown that nickel dopants in STNNi exhibit a tendency to be inhomogeneously distributed within the oxide lattice and, depending on the synthesis conditions, to separate from the perovskite phase. These observations indicate that the solubility of Ni in STNNi is limited, where a higher concentration limit can be estimated to be in the range between $x = 0.05$ and $x = 0.1$ at the perovksite B-site, which is equal to 1.0 at% - 2.0 at%. Notably, first indications for a deviation from the ideal elemental distribution were detected even when no secondary phases were detectable at a doping level of $x = 0.05$ (for MOR sample). The tendency for the formation of NiO secondary phases appears to be influenced by the applied synthesis route. While the Pechini method is based on the synthesis of oxides from single ions, MOR involves (nano)powders as educts. Since significant amounts of NiO secondary phases were only detected in ceramics fabricated from Pechini powders, it may be reasonable to conclude that NiO forma-

---

[2] The microscopic imaging was supported by K. Kistermann, S. Zischke and C. Herwartz (Gemeinschaftslabor für Elektronenmikroskopie (GFE), RWTH Aachen, 52074 Aachen, Germany) whose support is highly appreciated.

tion is promoted during the early stages of the Pechini process. It is worth to point out that differences in the distribution and size of secondary phases may influence their detectability by XRD and TEM / EDXS. Consequently, a certain degree of inhomogeneity in the dopant distribution can not be excluded, however the findings indicate that a doping level of x = 0.05 can be accommodated in STNNi without the formation of considerable amounts of secondary phases.

In order to ensure a high amount of exsolution-active dopants in the perovskite oxide, STNNi ceramics with a substitution level of $x = 0.05$ are in the following applied for thin film growth. Therefore, the discussion of the exsolution process throughout this work is based on a composition of $SrTi_{0.9}Nb_{0.05}Ni_{0.05}O_{3-\delta}$ with equal concentration of donor-type and acceptor-type dopants in the parent perovskite unless indicated differently.

4.2 Epitaxial thin films

This section deals with the epitaxial deposition and the characterization of the material properties of epitaxial STNNi thin films in regard to surface morphology, crystallographic properties and stoichiometry. Epitaxial growth offers a high degree of control over the properties of complex oxides. For instance, STNNi thin films can be deposited with a single crystallographic orientation and with atomically smooth surfaces making them an ideal model system for studying surface processes, such as metal exsolution.

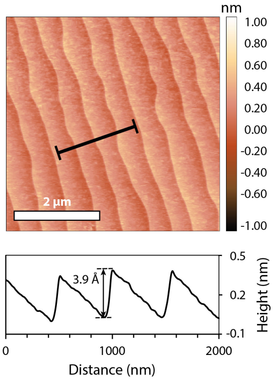

Figure 4.4: Surface morphology of a TiO_2-terminated $SrTiO_3$ single-crystal substrate after high-temperature annealing. A height profile extracted across several crystal terraces along the black line is shown below. The AFM scan size is 5 x 5 µm^2 and the scale bar denotes 2 µm.

4.2.1 Preparation of $SrTiO_3$ substrates

(001)-oriented $SrTiO_3$ and Nb:STO_3 substrates and were applied for the deposition of epitaxial thin films. Subsequently, a high-temperature annealing process is applied under continuous flow of a Ar/O_2 (80 : 20) gas mixture at T = 950°C for 2 h to obtain substrates with a well-defined step terrace structure. A detailed description of the substrate processing is given in section 3.1.2.

The step terraces originate from the miscut between the crystallographic lattice planes and the polished surface and are a characteristic feature of atomically defined surfaces. Therefore, the terrace width may vary (typically several hundreds of nanometers) while the respective step terrace height is typically in the order of one unit cell of the perovskite oxide as visible by an AFM line scan across the terrace steps shown in Fig. 4.4. Ideal STO surfaces show straight step ledges.[130]

4.2.2 Growth of epitaxial STNNi thin films on $SrTiO_3$

Pulsed laser deposition of STNNi

STNNi thin films are epitaxially deposited by RHEED-controlled PLD in [001] orientation. The growth parameters were adapted from reference [154] and minor adjustments of the laser fluence and the substrate temperature were performed, to optimize the thin film quality with respect to the surface morphology and stoichiometry. Details on the growth conditions are given in

In-situ monitoring of the electron surface diffraction pattern during growth enables to follow the structural characteristics of the evolving thin film surface which provides information about the growth kinetics of the material. Based on the distinct oscillations recorded on the basis of the averaged intensity of the (0 0)

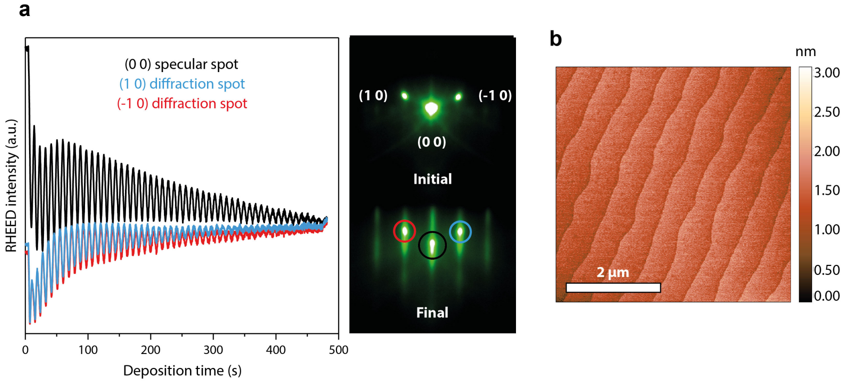

Figure 4.5: Growth of STNNi thin films on $SrTiO_3$. (a) Representative RHEED-intensity evolution recorded based on the averaged intensity of the (0 0) specular spot during *in-situ* monitoring of the thin film deposition (left). RHEED surface diffraction pattern obtained in the initial state *i.e.* recorded from the substrate and after in the final state *i.e.* after completed thin film growth (right); (b) Representative surface morphology of STNNi thin films. The AFM scan size is 5 x 5 μm^2 and the scale bar denotes 2 µm. The thin film thickness is 20 nm.

specular spot, a layer-by-layer growth mode is evident, typically over the entire deposition time (Fig. 4.5a). Notably, the base level intensity of the 1^{st} order (1 0); (-1 0) diffraction signals remains constant during the deposition, which indicates that the thin film surface remains predominantly TiO_2-terminated.[155] The two-dimensional growth mode results in an atomically defined surface morphology, adopting the characteristic step terrace structure of the underlying substrate (Fig. 4.5b). Throughout this work, STNNi thin films between 20 - 400 nm are used for the experiments.

Thin film characterization

As revealed by XRD, the STNNi thin films are deposited in a single orientation, solely revealing diffraction peaks along the (001) crystallographic axis (Fig. 4.6). While the Pechini target exhibits a minor NiO secondary phase, no secondary phases are detected by wide-angle 2θ-ω scans obtained from the epitaxial thin films. A comparison of the (002) diffraction peak obtained from the STNNi thin films deposited using the Pechini target (green) and the MOR target (purple), that exhibit a different degree of Ni inhomogeneity is given in Fig. 4.6b. As can be seen, the position of the diffraction signal *i.e.* the lattice parameter, which is determined by the structural properties of the thin film material is well comparable for both thin films. Presumably, atomization of the ceramic material during laser ablation provides for comparable plasma plume properties and growth characteristics for both of the ceramic targets. KIESSIG fringes are visible in the vicinity of the thin film diffraction signals, indicating the coherent growth and a sharp substrate-to-thin film interface as well as smooth thin film surface. Please note that the shoulder next to the diffraction peak of the substrate, visible in the purple curve, originates from a second domain of the STO substrate. XRD reciprocal space mapping (RSM) in grazing exit geometry around the asymmetric $(013)_+$ diffraction peak, reveals a fully strained crystal lattice of the perovskite thin film, based on the in-plane a-lattice parameter (*cf.* Fig. 4.6c). As can be seen, the thin film lattice adapts the a-lattice parameter of the underlying STO substrate.

The stoichiometry of the epitaxial films was characterized by surface-sensitive XPS and, after dissolution of the thin film material, by bulk-sensitive ICP-MS analysis. The quantification of the cation stoichiometry in the near-surface region was performed based on the relative peak area of the XPS Ti 2p, Sr 3d, Nb 3d, and Ni 2p core-level spectra after calibration of the relative sensitivity factors (RSFs) on the stoichiometry of the ceramic PLD target by means of a reference measurement. To determine the bulk stoichiometry, epitaxial STNNi thin films were deposited on $NdGaO_3$ with a thickness of 50 nm, dis-

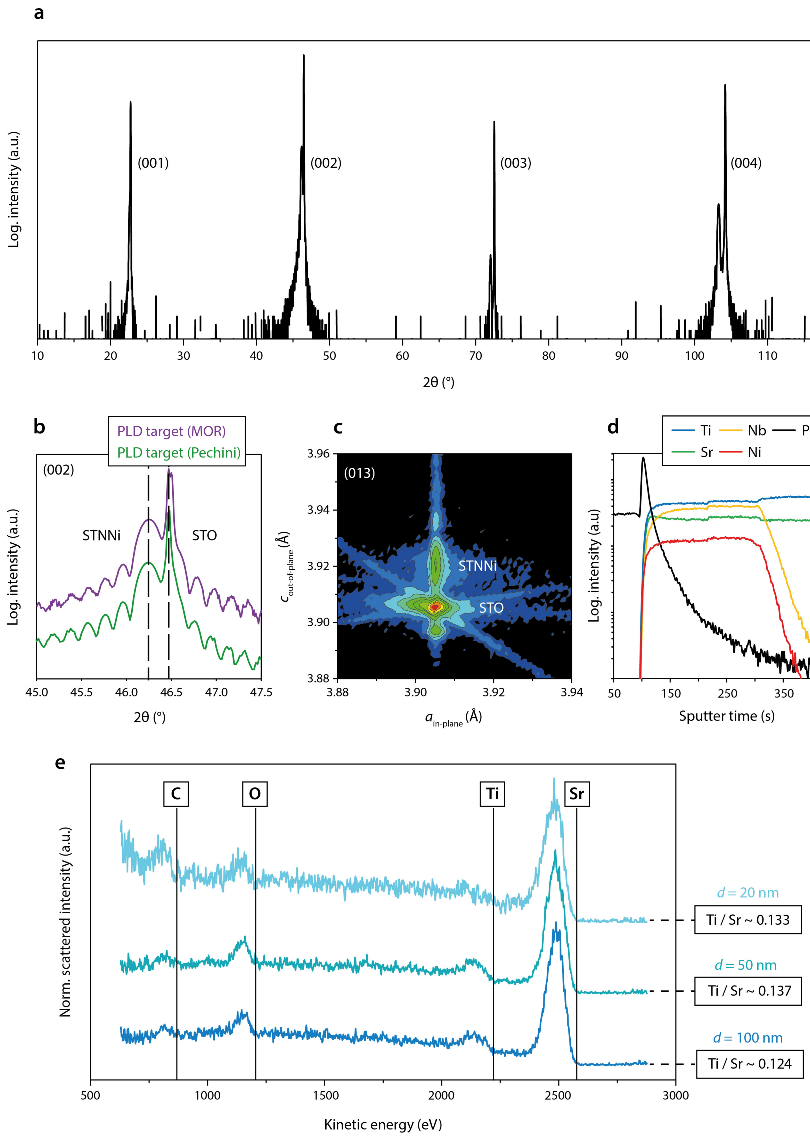

Figure 4.6: Structural characterization of 50 nm thick epitaxial STNNi thin films and probing of the cation distribution. (a) Wide-angle XRD analysis in 2θ-ω-geometry. (b) Detailed 2θ-ω scan of the (002) diffraction peaks of the STNNi thin film (left) and the STO substrate (right). (c) RSM around the (013) diffraction peak of the STNNi / STO material system. (d) SIMS depth-profiling of thin film cations. (e) LEIS of STNNi thin films with thicknesses of 20 nm, 50 nm and 100 nm in the as-prepared state. The normalized spectra are plotted with an offset for better visibility. The ratios of the Ti / Sr peak area are determined after subtraction of a Shirley background.

solved in a mixture of HCl / H_2O_2 and subsequently characterized by ICP-MS.[3] Both, surface stoichiometry $SrTi_{0.905}Nb_{0.044}Ni_{0.051}O_{3-\delta}$ and bulk stoichiometry $SrTi_{0.872}Nb_{0.070}Ni_{0.058}O_{3-\delta}$ were determined to be close to the nominal stoichiometry of $SrTi_{0.9}Nb_{0.05}Ni_{0.05}O_{3-\delta}$. Moreover, the cation distribution across the thin film thickness is investigated by secondary ion mass spectrometry after the capping of the thin film by evaporation with platinum (30 nm) to avoid irregular sputtering effects at the surface (Fig. 4.6d).[4] Homogeneous distribution of the Ni- / Nb- dopants and the Sr- / Ti- host cations is detected across the thin film bulk by means of SIMS depth-profiling. Here, a step increase of the Ti, Sr, Nb and Ni intensity indicates the Pt-to-thin film interface, while a drop in the intensity profile of the Nb and Ni dopants is visible when sputtering across the thin film-to-substrate interface.

Furthermore, low energy ion scattering (LEIS) is carried out, to investigate the elemental composition of the first atomic layer of the surface.[5] As can be seen in Fig. 4.6e, LEIS spectra were obtained from the surface of as-prepared STNNi thin films with a thickness of 20 nm, 50 nm and 100 nm. While an exact quantification of the stoichiometry of the termination layer is challenging, relative peak areas can be used to compare relative differences in the surface termination. Four prominent peaks are visible in each spectrum, that can be assigned to carbon, oxygen, strontium and titanium as denoted in the figure. Notably, a larger amount of carbon contaminants at the surface results in a decreased signal-to-noise ratio for the 20 nm sample. The peak areas are determined after subtraction of a Shirley-type background and the Ti / Sr ratios are determined, respectively. As can be seen from the signal ratios given in the figure, no significant differences in the values are detected, which indicates that the surface termination is comparable for all samples, independent from sample thickness.

Transmission electron microscopy (TEM), energy dispersive X-ray spectroscopy (EDXS) and selected area electron diffraction (SAED) is applied to investigate the nanoscale and atomic structure as well as the chemical composition of the STNNi thin films.[6] As can be seen in Fig. 4.7, inhomogeneities are detected in the as-prepared STNNi perovskite lattice. The presence of column-like structures, coherently embedded in the perovksite host lattice is visible, appearing in bright contrast

---

[3] The ICP-MS measurements were performed by V. Nischwitz (Central Institute for Engineering, Electronics and Analytics (ZEA-3), Forschungszentrum Jülich GmbH, 52425 Jülich, Germany) whose support is highly appreciated.

[4] The SIMS measurements were performed by U. Breuer (Central Institute for Engineering, Electronics and Analytics (ZEA-3), Forschungszentrum Jülich GmbH, 52425 Jülich, Germany) whose support is highly appreciated.

[5] The LEIS experiments were supported by S. Fearn (Imperial College London, Department of Materials, London SW7 2BP, United Kingdom) whose support is highly appreciated.

[6] The high-resolution microscopic investigations were performed by L. Jin (Ernst Ruska-Centre for Microscopy and Spectroscopy with Electrons (ER-C), Forschungszentrum Jülich GmbH, 52425 Jülich, Germany) and whose support is highly appreciated.

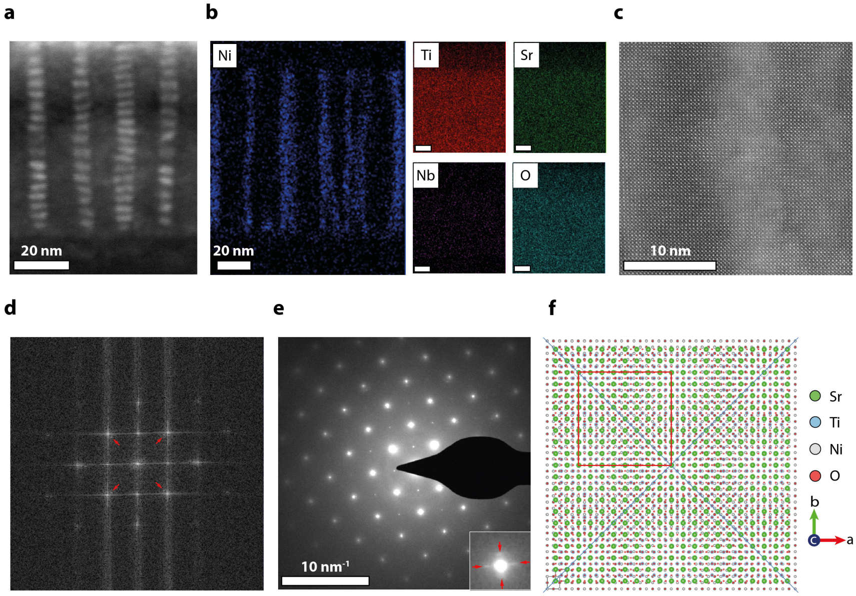

Figure 4.7: Nanoscale investigation of the structural properties and chemical composition of a representative, stoichiometric $SrTi_{0.9}Nb_{0.05}Ni_{0.05}O_{3-\delta}$ thin film in the as-prepared state. The thin film thickness is 100 nm. (a) Dark-field imaging reveals the presence of inhomogeneities in the form of column-like, vertically aligned nanostructures in the perovskite lattice of the as-prepared thin films. The scale bar denotes 20 nm. (b) Enrichment of the nanostructures with Ni dopants is detected by EDXS analysis. Scale-bars denote 20 nm. (c) High-annular angle dark-field imaging shows a detailed scan of one of the atomic structure with a embedded column of bright Z-contrast in the coherently grown strontium titanate host lattice. The scale bar denotes 10 nm. (d) Fast-Fourier transform of Z-contrast image shown in (b) reveals faint satellite spots in the vicinity of the main diffraction spots originating from dynamic scattering events (*i.e.* double diffraction) at a superimposed crystal phase of different lattice spacing (highlighted by red arrows). (e) The electron diffraction pattern exhibits intensity modulations as a results of double diffraction. The respective satellite spots are visible around each of the main diffraction spots. A close-up of a representative diffraction spot is given as inset image where the satellite spots are highlighted by red arrows. The scale bar denotes 10 nm^{-1}. (f) Simulation of the MOIRÉ pattern for the superimposed crystal lattices of $SrTiO_{3-\delta}$ and NiO. The periodicity of the MOIRÉ fringes is highlighted by red square. The model consists of 20 x 20 x 2 unit cells.

(Fig. 4.7a). Significant concentration variations in the nickel distribution, correlated to the nanostructures, are detected by means of EDXS. The embedded phase hence is enriched by Ni-dopants, while the Sr-, Ti-, and Nb-cations appear to be homogeneously distributed (Fig. 4.7b). A representative high-resolution image (aligned in zone-axis) of one of the nano-columns is shown in (Fig. 4.7c). Ni-dopants appear in bright signal in the center of the Z-contrast image, while the (predominantly Nb-doped) strontium titanate host lattice exhibits a coherent atomic structure. Faint intensity modulations are visible, which result from dynamic scattering events on different crystallographic phases (double diffraction), superimposed in the direction of the incident electron beam (remark: please see also imaging of the reduced state of the sample shown in Fig. 4.11 with more distinct intensity modulations). The emergence of the translational MOIRÉ pattern is furthermore reflected by satellite spots visible in the fast-Fourier transform of the Z-contrast image (Fig. 4.7d) as well as the electron diffraction pattern (Fig. 4.7e). Material systems of similar structural relationships are reported in literature, which are typically referred to as vertically aligned nanostructures (VANs).[156–159] In these cases, however, VANs are deliberately fabricated by sequential ablation of different oxide materials or application of highly non-stoichiometric mixed-phase PLD targets with compositions far from solubility.

Using the lattice parameter of the perovskite crystal lattice determined by XRD analysis as an internal reference, analysis on the SAED pattern enables to determine the lattice parameter of the Ni-rich phase. Here, an out-of-plane lattice parameter of c = 4.454 Å and an in-plane lattice parameter of a = 4.376 Å was determined, which is close to the lattice parameter of NiO. However, deviations from the nominal lattice parameter of NiO (d = 4.178 Å) are observed which are presumably linked to defective growth of the embedded nanostructures. In Fig. 4.7f, a simulated model of the superimposed strontium titanate and NiO crystal lattice is displayed. Consistent with TEM imaging, intensity modulations of equal periodicity as observed in the Z-contrast image are visible in the simulated real-space MOIRÉ pattern of the given material composition.

To further clarify the mechanisms underlying the accommodation of the nanostructures, a detailed analysis of the structural arrangement is given below. The structural assembly along the vertical interface of the two crystal phases can be described by a coincidence site lattice (CSL) model.[95, 96, 156, 160] Here a semi-coherent interface is formed with a superstructure between the oxides as described by equation 4.1.

$$n \times d_1 = (n \pm 1) \times d_2 \tag{4.1}$$

Accordingly, n spacings d_1 of the crystallographic planes of material 1, *e.g.* of the strontium titanate host lattice, match with $n \pm 1$ spacings d_2 of crystallographic planes of material 2, *e.g.* of the embedded NiO phase. For the present material system a registry of $n = 16$ unit cells of the host oxide was found to match a number of $n = 15$ unit cells of NiO. Notably, the respective domain matching registry results in a visible periodicity with modified, half-order modulations equal to 7.5 : 8 unit cells as indicated by the red square in Fig. 4.7f.

The minimum CSL misfit, which results from the residual mismatch between the domains, *i.e.* registries of both materials, can be determined by equation 4.2.

$$F_{\mathrm{CSL}} = 1 - \left(\frac{(n+1) \times d_1}{n \times d_2} \right) \tag{4.2}$$

According to equation 4.2, the given material constitutes a system with a CSL misfit of $F_{\mathrm{CSL}} = +\,0.18\,\%$. The residual misfit may be compensated by elastic deformation of one or both of the oxide lattices.

Systematic variation of the B-site doping level

Fig. 4.8a shows the lower-order (002) and higher-order (004) diffraction peaks obtained from STNNi thin films of varying Ni-doping level ($x = 0.0$ - 0.1). The thin films were deposited by ablation from ceramic pellets with the respective stoichiometry (*cf.* Fig. 4.2). In contrast to the ceramic samples, a systematic shift in the diffraction angle of the thin film peaks is apparent for the epitaxial STNNi thin films. It reflects an increasing expansion of the out-of-plane c-parameter of the perovskite lattice, with increasing substitution of titanium by nickel cations. The correlation between the c-lattice constants with the doping level x is shown in Fig. 4.8b. The lattice parameters were determined on the basis of the respective (004) diffraction signals according to Bragg's law and by assuming a cubic perovskite structure. For this purpose, the diffraction angles were corrected in reference to the signal of the STO substrate serving as an internal reference. The mismatch *i.e.* strain-induced expansion between the STNNi lattice of the bulk material ($x = 0$) and the STNNi thin films of varying Ni-doping level is given on the secondary y-axis.

The systematic variation of the lattice parameter is typically interpreted as an indicator for the successive substitution of host cations with dopant cations.[152, 161] As discussed above however, the Ni-dopants exhibit a considerable tendency to separate from the perovskite phase and to form vertically aligned nanostructures that assemble in a well-defined structural relationship with the surrounding perovskite lattice (Fig. 4.8c). Here, the domain matching relationship at the semi-coherent interface induces elastic deformation of the host oxide to compensate

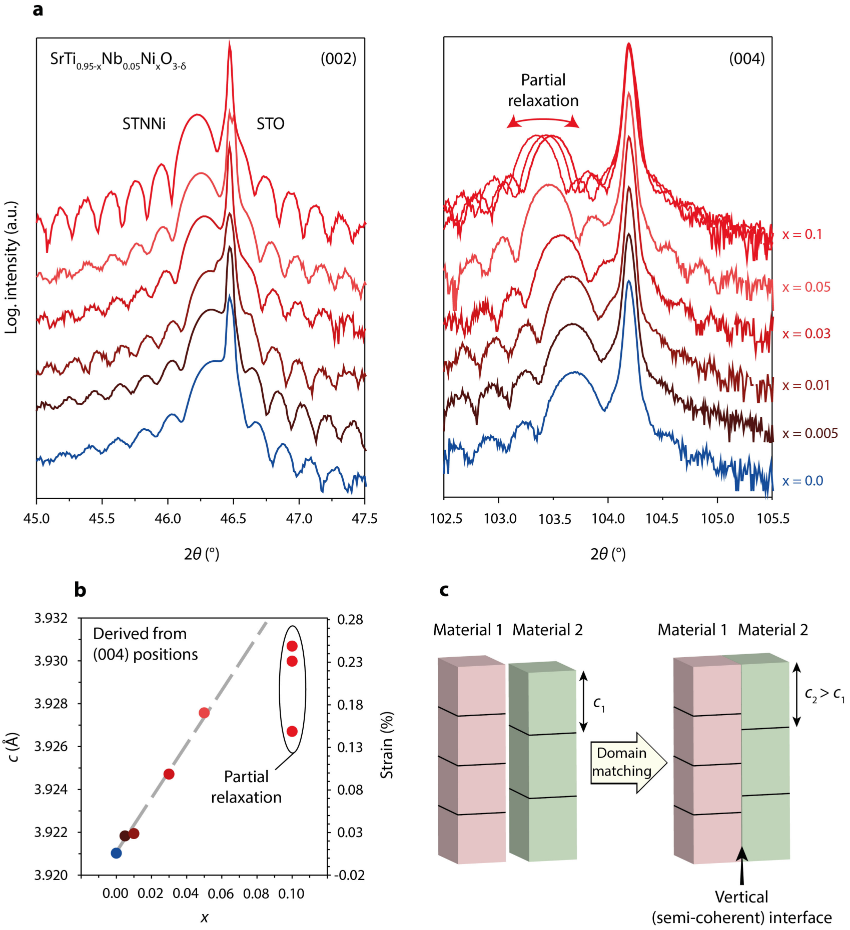

Figure 4.8: X-ray diffraction analysis of epitaxial $\mathrm{SrTi_{0.95-\mathit{x}}Nb_{0.05}Ni_{\mathit{x}}O_{3-\delta}}$ thin films with different Ni-doping levels between x = 0.0 - 0.1 deposited on STO. (a) Diffractograms obtained in the vicinity of the (002) and (004) diffraction signals measured in 2θ-ω-geometry. The thin film thickness is 50 nm respectively. (b) Dependence of the c-parameter on the Ni-doping level x. (c) Schematic illustration of the domain matching superstructure at the vertical interface of two materials. The residual mismatch of the both matching registries is compensated by the introduction of strain, which results in an expansion of the crystal lattice. The magnitude of the induced strain depends on the interfacial area between material 1 and material 2 and hence on the doping level x.

for the residual mismatch. The induced strain is directly related to the interfacial area between both phases and, therefore, to the total volume of the embedded phase.[156]

Consistently, the *c*-lattice parameter expands linearly for increasing doping levels between $x = 0.0$ and $x = 0.05$. At a high Ni-doping of $x = 0.1$ a considerable deviation from the linear trend can be observed (Fig. 4.8a,b). The partial relaxation of the thin film lattice was reported to be associated with the formation of dislocations at the interface between the perovskite host lattice and the embedded phase.[156] At low dopant concentrations, no definite conclusions about the dissolution behaviour of Ni can be made, since the exact solubility limit is not known and hardly accessible, and in case the dopants do not dissolve in the perovskite lattice even at such low concentrations the impact on the assembly of the embedded nanostructures remains unclear. Furthermore the presence of B-site vacancies, which are left behind as a result of the phase separation of NiO_x-VANs may contribute to the overall expansion of the lattice as they will have direct impact on the steric and electrostatic interactions of neighbouring ions of the crystal lattice.

4.3 Characterization of the exsolution response upon reducing annealing

To investigate the exsolution response of STNNi, the ceramic samples (fabricated *via* the MOR) and thin films are thermally reduced by annealing under continuous flow of a 4% H_2 / Ar gas mixture (T = 800°C, 5 h). As can be seen in Fig. 4.9a, nanoparticle exsolution can be observed at the polished surface of a ceramic pellet by SEM (left) and its internal surfaces in a porous ceramic (right) as revealed by STEM analysis. Notably, for ceramic samples prepared from powders synthesized by the Pechni route, no exsolution particles were detected after reducing annealing at equal conditions. Here, the extensive agglomeration of Ni in the form of extended secondary phases may inhibit the exsolution activity of the material.

As can be seen in Fig. 4.9b, similarly to the MOR ceramic pellet the formation of nanoparticles is visible at the surface of epitaxial thin films of 30 monolayers thickness after thermal reduction for different times of 5 h, 8.5 h and 15 h (4% H_2 / Ar, T = 800°C). Here, the smooth thin film surface allows to detect exsolution particles on top of the highly defined step terraces structure, which is a characteristic feature of high-quality perovskite crystal surfaces (*cf.* section 4.2.2) and which is preserved during the annealing treatment. As illustrated by line profiles obtained from the topological data (Fig. 4.9c), the investigation of Ni exsolution on the basis of the STNNi thin film samples enables to detect the particle growth over time. Here, increasing particle heights with increasing reduction times can be observed. The strong exsolution response under reducing conditions illustrates the high affinity

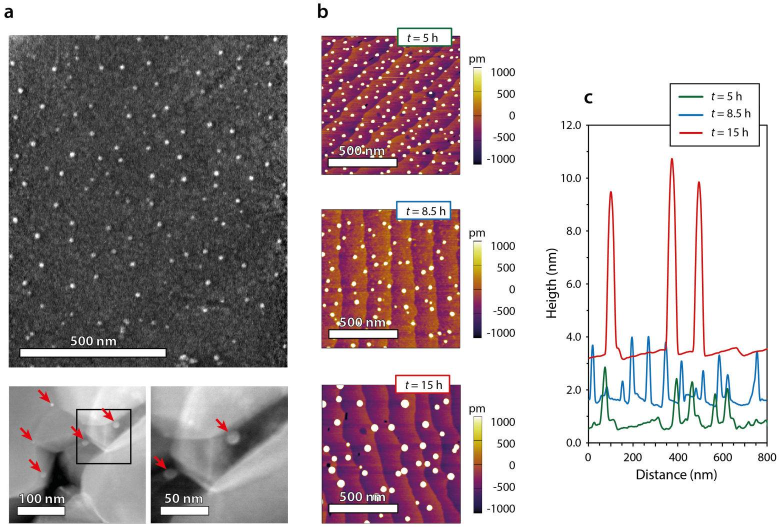

Figure 4.9: Microscopic imaging of $SrTi_{0.9}Nb_{0.05}Ni_{0.05}O_{3-\delta}$ after reducing thermal treatment. (a) SEM imaging of the polished surface (above) and STEM imaging of the bulk microstructure in dark-field mode (below) of a ceramic pellet after reduction (T = 800°C, 5 h, 4% H_2 / Ar). Several nanoparticles are highlighted by red arrows in the TEM image. (b) AFM imaging of three pieces that were cut from the same thin film sample after thermal reduction (T = 800°C, 4% H_2 / Ar). Reduction times of 5 h, 8.5 h and 15 h are applied. The AFM scan size is 1 x 1 μm^2 and the scale bar denotes 500 nm. The thin film thickness is 30 monolayers. (c) Line profiles across the thin film surface with exsolved nanoparticles, obtained from the AFM scans of the STNNi surface after reduction for different annealing times shown in (b), displayed with a slight offset on the y-axis.

of the STNNi perovksite for metal exsolution. For comparison, the evolution of the surface morphology of an $SrTiO_{3-\delta}$ thin film under reducing conditions is shown in the appendix B.

In the following, the metal exsolution response is studied in detail based on the epitaxial thin film model systems. The reducing thermal treatment is accompanied by considerable changes in the material properties of the perovskite thin films. These are, in part, directly associated to the exsolution process and thus can be used to follow the exsolution response of STNNi beyond mere morphological investigations.

The relative cation stoichiometry is determined by XPS analysis. After thermal reduction, a substantial enrichment of Ni is evident in the near-surface region of the thin films in comparison to the initially close-to stoichiometric perovskite surface in the as-prepared state (Fig. 4.10a). Please note that the increase in the atomic percentage is only a qualitative measure of dopant enrichment, since the measurement geometry is altered upon exsolution due to nanoparticle formation, which

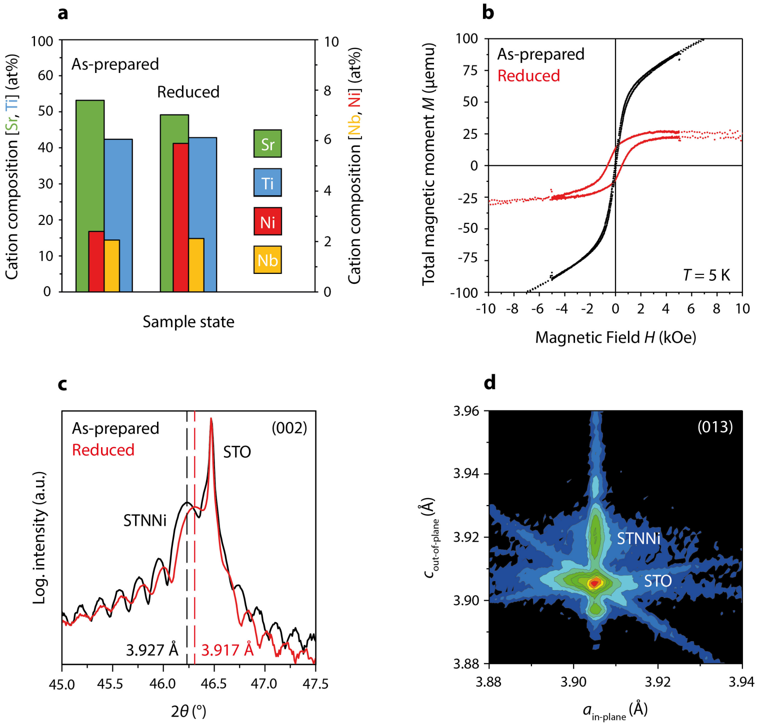

Figure 4.10: Characterization of the exsolution response of STNNi thin films under reducing thermal treatment at T = 800°C for 15 h under continuous 4% H_2/Ar gas flow. The thin film thickness is 50 nm. (a) Relative surface stoichiometry of the thin film model system derived from quantitative analysis of XPS core-level spectra, comparing the as-prepared and the reduced state. (b) Magnetic signature of STNNi thin films by vibrating sample magnetometer measurements show a magnetic transition upon reducing annealing, which gives information about the phase transition of Ni towards the metallic state during exsolution. (c) XRD 2θ-ω scan of the (002) diffraction peaks of the STNNi thin film (left) and the STO substrate (right) obtained from the as-prepared sample (black) and after metal exsolution (red). Distinct KIESSIG fringes are visible in the vicinity of the thin film diffraction signal in both sample states. A shift in the thin film diffraction peak towards larger 2θ-angles after exsolution is detected. (d) Reciprocal space mapping around the (013) diffraction peak of the STNNi / STO material system after reduction shows that the in-plane strain between the STO substrate and the STNNi thin film is preserved during high-temperature annealing.

prevents a conclusive quantitative analysis (smooth *vs.* nanostructured surface). Furthermore, a meaningful analysis of the chemical state of nickel is hampered due to the exposure of the thin films to air during sample transfer from the annealing furnace to the XPS chamber. Here, rapid surface re-oxidation of the metallic nickel particles leads to a predominant oxide / hydroxide signal.

The metallic character of the Ni nanoparticles after reduction however, is detected by vibrating sample magnetometry (VSM), where the total magnetic moment is plotted versus the applied external magnetic field.[7] In the as-prepared state a small coercive field of H_C = 50 Oe is evident from the hysteresis loop where the magnetic moment does not saturate, which may indicate a superparamagnetic behavior. This observation is consistent with the reported superparamagnetic relaxation of the spin lattices of antiferromagnetic NiO nanoparticles, which exhibit permanent magnetic moments arising from uncompensated surface spins.[162–164] In comparison, the hysteresis loop obtained from the sample after thermal reduction is given in red. A ferromagnetic signal is evident based on the considerably larger coercive field of H_C = 570 Oe. Consequently, a magnetic transition from nickel species initially present in a oxidized form towards Ni metal is evident which can be assigned to the exsolution of metallic nanoparticles.

Furthermore, metal exsolution is accompanied by the structural relaxation of the *c*-lattice parameter as revealed by XRD analysis (Fig. 4.10b). After reducing treatment of the thin film, a pronounced shift in the position of the diffraction peak of the thin film is visible (red) in comparison to the as-prepared state shown as a reference (black). Notably, the in-plane *a*-lattice parameter remains constant upon reducing thermal treatment (Fig. 4.10c). Thus, the epitaxial strain at the substrate-to-thin film interface is preserved and structural changes induced by the reducing annealing are compensated by relaxation in *c*-direction of the perovskite lattice. Here, different processes need to be taken into account which may influence the changes in the structural properties. Most importantly, the release of Ni-dopants to the surface may allow for a relaxation of the perovskite film.[27, 29, 30] Accordingly, the introduction of B-site cation vacancies as well as the formation of oxygen vacancies needs to be considered, which in turn are likely to induce a slight expansion of the perovskite lattice.[165–167]. Furthermore, changes in the transition metal valence state associated to oxygen release may contribute to the altered structural properties due to the valency-dependent ionic radius.[167, 168] In addition to that, changes in the superstructure of the vertical semi-coherent interface of the two oxide phases may play an important role for the structural properties of the present material system of embedded VANs. Here, reducing treatment at elevated temperatures is likely to affect the nature of the domain matching relationship at the vertical interface.

---

[7] The VSM measurements were performed in collaboration with M. Wilhelm (Forschungzentrum Jülich, Peter Grünberg Institut (PGI-6), 52425 Jülich, Germany) whose support is highly appreciated.

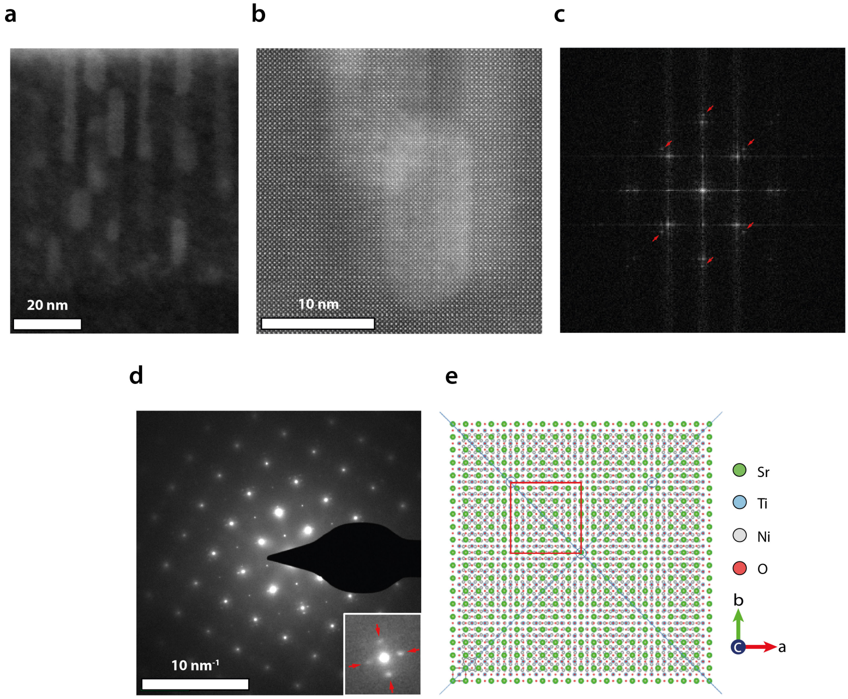

Figure 4.11: Nanoscale investigation of the structural properties and chemical composition of a representative, stoichiometric $SrTi_{0.9}Nb_{0.05}Ni_{0.05}O_{3-\delta}$ thin film after reducing thermal treatment at T = 800°C for 15 h under continuous 4 % H_2/Ar gas flow. The thin film thickness is 100 nm. (a) Dark-field imaging reveals an altered distribution of and partial depletion from the embedded phase. (b) High-annular angle dark-field imaging shows a detailed scan of a capsule-shaped nanoparticle formed under reducing annealing, while the atomic ordering of the surrounding strontium titanate host lattice is preserved. (c) Fast-Fourier transform of the Z-contrast image shown in (b) reveals clear satellite spots in the vicinity of the main diffraction pattern originating from dynamic scattering events (*i.e.* double diffraction) at a superimposed crystal phases of different lattice spacing (highlighted by red arrows). (d) Selected area electron diffraction reveals clear intensity modulations as a results of double diffraction. The respective satellite spots are visible around each of the main diffraction spots. A close-up of a representative diffraction spot is given as inset image where the satellite spots are highlighted by red arrows. (e) Simulation of the MOIRÉ pattern for the superimposed crystal lattices of $SrTiO_{3-\delta}$ and metallic nickel. The periodicity of the MOIRÉ fringes is highlighted by the red square. The model consists of 20 x 20 x 2 unit cells.

To evaluate the structural relationship of the thin film bulk after reduction, microscopic investigations were carried out as shown in Fig. 4.11. Notably, the measurements were performed in the same manner as for the as-prepared sample state discussed above (*cf.* Fig. 4.7) using a piece of the identical thin film for thermal reduction. As can be seen, the initially well-ordered nanostructures appear to redistribute within the host lattice upon reducing heat treatment (Fig. 4.11a). Atomic scale imaging reveals the formation of capsule-shaped nanoclusters of clear perimeter, while the coherency in the atomic ordering of the perovksite host lattice is preserved (Fig. 4.11b). In comparison to the as-prepared state, an enhanced modulation of the Z-contrast intensity in the area of the overlapping crystal phases is visible, which may indicate an improved orientation relationship between the embedded phase and the host lattice with respect to the zone axis as well as an increased crystallinity of the embedded nanoclusters.

Equally, pronounced intensity modulations are visible in the fast-Fourier transform of the Z-contrast image (Fig. 4.11c). Based on the diffraction patterns obtained by SAED (Fig. 4.11d), the respective diffraction vectors are determined, which allow for the calculation of the lattice parameters (see appendix A). Similar to the as-prepared state of the sample, a domain-matching relationship is apparent at the metal-to-oxide interface. Here, the lattice parameter of the embedded phase is determined to be close to nickel metal. Hence a phase transition from the initial NiO_x phase to metallic Ni is apparent. A simulated model of the superimposed strontium titanate and Ni metal crystal lattice is shown in Fig. 4.11e, which exhibits a MOIRÉ pattern with intensity modulations of equal magnitude as observed in the experimentally derived Z-contrast images.

4.4 Discussion: Phase separation and subsequent dopant transport as alternative exsolution pathway

Ceramic pellets of niobium and nickel co-doped strontium titanate were sintered as exsolution-active parent material serving as model material for the investigation of nickel exsolution. By application of the respective ceramics as PLD target, high-quality epitaxial thin films were synthesized on (001) STO substrates by means of pulsed laser deposition. The strong affinity for the exsolution of nickel in the form of metallic nanoparticles was demonstrated for both, the bulk and the thin film material system.

Microscopic investigations (STEM / EDXS) indicated a certain degree of inhomogeneity in the distribution of the Ni-dopants within the ceramic samples, that was found to depend on the respective synthesis route. The formation of a minor NiO secondary phase was detected by XRD and STEM imaging for STNNi ceramics synthesized by the Pechini route, while no secondary phases were detected for STNNi ceramics of equal stoichiometry that were fabricated by the mixed-oxide synthesis route. The solubility of Ni was further investigated by systematic variation of the Ni-doping level within the STNNi material system (MOR). Here, detectable amounts of NiO were solely found for a high doping level of 10 % at the perovksite B-site. Remarkably, no systematic shift in the lattice parameter was evident for the ceramic samples of different Ni doping, while a clear trend of increasing lattice expansion was apparent for epitaxial thin films with increasing doping level. Independent from the cation substitution level, no secondary phases were detected for the epitaxial thin films by XRD. In fact, the samples appeared to exhibit the characteristics of single-crystalline epitaxial materials. An approach of the combined investigation of the growth kinetics, surface morphology, surface- and bulk-stoichiometry, cation distribution as well as the crystallographic properties did not reveal any evidence for the deviation from the ideal perovskite structure.

Careful STEM analysis of the thin film structure on the atomic scale, however, revealed the presence of inhomogeneities in the perovskite lattice with respect to the elemental distribution and the perovskite structure. Based on the STEM investigations, the assembly of nanoscale secondary structures, which are vertically aligned between the substrate-to-thin film interface and the thin film surface and enriched by Ni dopants became visible. The detection of the embedded nanostructures by state-of-the-art analysis techniques may be strongly hampered by the nanometre size of the embedded nanostructures as well as by their uniform lateral distribution within the perovskite lattice. Here, small coherence lengths may prevent the detection by X-ray diffraction, while the limited depths relation and lateral resolution of SIMS does not allow to resolve the dopant inhomogeneities.

The surrounding perovskite host lattice, however, was found to be highly coherent in atomic ordering. Apart from the (partial) phase separation of nickel and the associated enrichment of Ni at designated areas of the perovskite lattice, the remaining cations were detected to be homogeneously distributed. The STNNi thin film system hence rather constitutes a nanostructured composite material than a single-crystal sample. The inhomogeneous distribution of Ni dopants and the accumulation of nickel in the form of nanostructures within the perovskite lattice may be related to a low solubility of Ni in the strontium titanate host lattice.[169] Moreover, the limited solubility of Ni in STNNi may be related to the defect chemistry of the material. Here, the charge compensation of the Nb-donors by the introduction of Sr-vacancies may be favored over the intended charge compensation by nickel doping.[149, 150]

The vertical interface between the embedded and the host oxide phases is assembled in a domain matching relationship with a semi-coherent interface. Consequently, a small residual mismatch along the interface of the crystallographic phases arises from the specific structural relationship. The structural properties of the perovksite are hence determined by four main parameters, which are (1) the

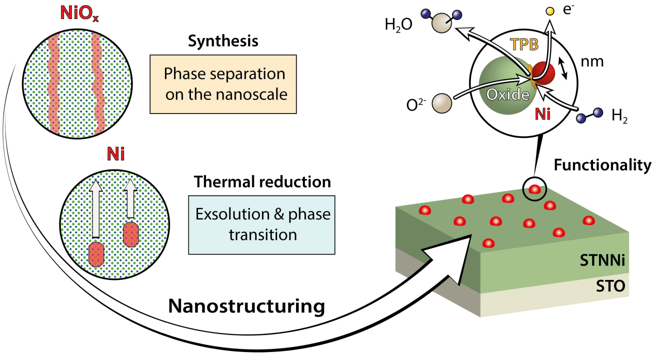

Figure 4.12: Schematic illustration of the exsolution pathway in STNNi. Ni-rich, vertically aligned nanostructures form during synthesis of the exsolution-active parent material. Nanostructuring of the perovskite surface by metal exsolution is induced by thermal reduction, which triggers the phase transition of Ni towards the metallic state. Nanostructured perovskites are promising candidates for the application in the field of energy conversion devices, due to the catalytically active triple-phase boundaries of the metal-oxide nanoframeworks.

concentration of extrinsic (mostly Nb) dopants (2) the compressive epitaxial strain at the horizontal interface between thin film and substrate (3) the CSL misfit F_{CSL} of the domains of both phases, *i.e.* the strain at the vertical interface as well as the interfacial area between both phases that depends on the volume fraction of the embedded phase and (4) dislocation density at the interface of both phases. Furthermore, (5) intrinsic defects, such as oxygen vacancies and cation vacancies may influence the structural nature of the STNNi thin films.

Upon reducing thermal treatment a strong exsolution response is evident in form of nanoparticle formation at the perovskite surface and in the oxide bulk. While the enrichment of Ni at the perovskite surface was detected spectroscopically, the detection of a magnetic transition provides evidence about the metallic character of the Ni particles. The process goes along with a structural relaxation, which may be in part related to the release of dopants from the oxide host lattice to the surface as well as the respective introduction of B-site (and oxygen) vacancies, and in part on the altered domain matching registry between the embedded and host oxide associated with the change from an oxide-to-oxide towards an oxide-to-metal vertical interface.

In conclusion, these findings have important implications for the fundamental understanding of metal exsolution processes, as they show that exsolution-active materials may not necessarily be single-phase perovskites (*cf.* Fig. 4.12). In contrast, exsolving elements may be enriched at designated areas of the perovskite host lattice, and hence be accommodated by local stoichiometry variations in the parent oxide on the nanometer scale. Nanostructures, which form during the synthesis of the exsolution-active parent materials are in contrast with the idealized concept of metal exsolution from a solid solution. It therefore needs to be considered as an alternative pathway which is based on the initial formation of dopant-rich phases and subsequent exsolution of reducible cations from the embedded secondary components.

In such materials, the phase separation, *i.e.* the release of B-site dopants from the perovskite structure and the subsequent transport towards the surface are widely decoupled since the dopants are already present in form separated phases. Therefore, it can be expected that the transport dynamics is of particular significance for the overall exsolution behavior. In this respect it should be noted that *exsolution* in STNNi describes the release of reducible dopants from the subsurface onto the surface, to be distinguished from the release of B-site cations from the perovskite structure on the unit cell level.

It is worth to point out that there might exist a smooth transition between solid solution materials and perovskites with locally enriched dopant concentrations and hence the coexistence of different exsolution routes is likely. It remains an open question to what extend the exsolution pathway may influence the nanoparticle assembly and the specific structural properties of the oxide-metal nanoframeworks.

Chapter 5

Exsolution of embedded nanoparticles in defect engineered perovskite layers

Defects play a critical role for metal exsolution. The use of A-site deficient perovskites as parent materials for the synthesis of nanostructured oxides *via* redox exsolution is a common strategy to yield an increased particle density at the surface, in comparison to stoichiometric perovskites.[19, 21, 22] Typically solid solutions are applied as parent materials. In order to investigate the influence of defects on the exsolution response of pre-formed, embedded nanostructures in STNNi (*cf.* chapter 4), a defect engineering approach is applied to tune the cation stoichiometry of the strontium titanate host lattice. For this purpose, the defect structure of the thin films is controlled by the laser fluence applied during the epitaxial growth. The exsolution behavior is compared for Sr-rich (A-site excess) and Sr-poor (A-site deficient) STNNi thin films. Please note that the data discussed in this chapter were partly published in [147].

5.1 Control of the defect structure based on the applied laser fluence

The epitaxial growth process by PLD offers many degrees of freedom to influence the material properties of functional oxides, for instance by the deliberate incorporation of defects. The technical feasibility of defect engineering by pulsed laser deposition of perovksite thin films is based on the kinetically determined growth process (*cf.* section 3.1.2). Among other parameters, the applied laser fluence has

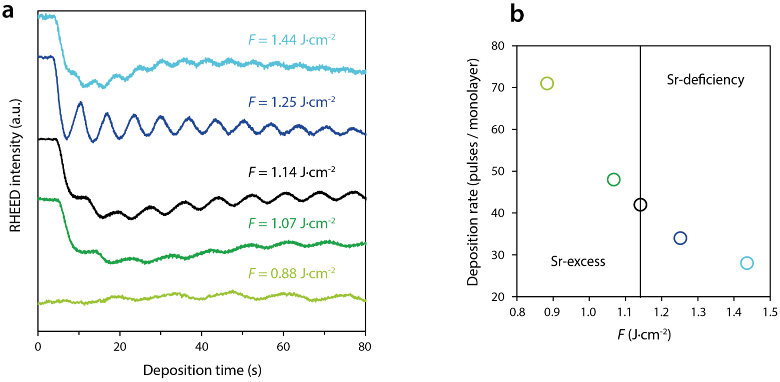

Figure 5.1: Deposition of 50 nm STNNi thin films with a laser fluence in the range between $F = 0.88\,\mathrm{J{\cdot}cm^{-2}}$ - $1.44\,\mathrm{J{\cdot}cm^{-2}}$ by PLD. (a) RHEED intensity evolution during the initial growth phase of STNNi thin films. (b) Fluence-dependent deposition rate, determined from the periodicity of the respective RHEED intensity oscillations. The solid black line denotes the stoichiometric point.

proven to affect the ablation and the plasma plume dynamics, and therefore, can be utilized to systematically change the cation stoichiometry, using a stoichiometric ceramic ablation target.[121, 170–175] When the laser fluence is tuned around the stoichiometric point, *i.e.* the sweet spot that results in stoichiometric growth for a given deposition geometry and a constant set of growth parameters, defects are introduced into the perovskite lattice. For strontium titanate, moderate non-stoichiometry was shown to be widely balanced by the Sr-sublattice in the form of cation vacancies, while at large vacancy concentrations, the formation of point defect clusters was observed.[171] Furthermore, the intergrowth of additional SrO planes, *i.e.* the formation of RP-type phases (stacking faults), was observed to compensate for Sr-excess.[94, 97, 175] In contrast, Sr-deficiency may result in the formation of separated, amorphous TiO_2 phases.[97]

STNNi thin films were deposited with a laser fluence between $F = 0.88\,\mathrm{J{\cdot}cm^{-2}}$ - $1.44\,\mathrm{J{\cdot}cm^{-2}}$. Two films with laser fluences above and below the stoichiometric point at $F = 1.14\,\mathrm{J{\cdot}cm^{-2}}$ are deposited, respectively. The RHEED intensity evolution, obtained by *in-situ* monitoring of the (0 0) specular spot during thin film growth is shown for the initial growth phase in Fig. 5.1a for STNNi depositions with different laser fluences. Here, a well-defined layer-by-layer growth mode is evident independent from the applied laser fluence. The deposition rate is determined on the basis of the periodicity of the intensity oscillations (Fig. 5.1b). Since the growth rate strongly depends on the laser fluence, the deposition time is adjusted to grow thin films of equal thickness.

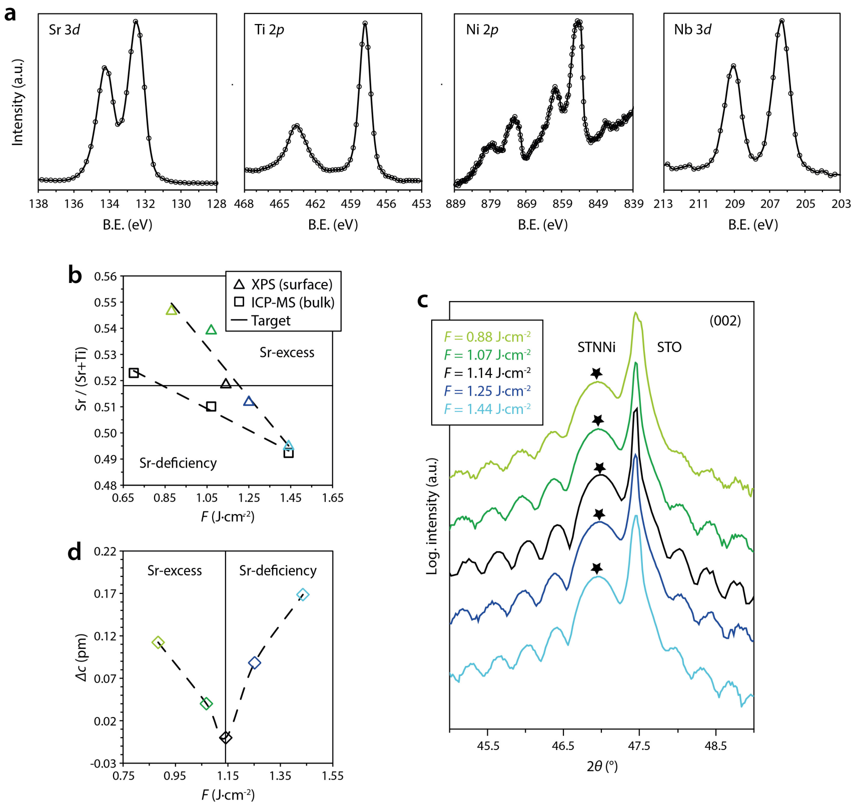

Figure 5.2: Investigation of defect incorporation for 50 nm STNNi thin films, deposited with laser fluences in the range between $F = 0.88\,\mathrm{J{\cdot}cm^{-2}}$ - $1.44\,\mathrm{J{\cdot}cm^{-2}}$ by PLD. (a) Representative XPS Sr 3*d*, Ti 2*p*, Ni 2*p* and Nb 3*d* core-level spectra, measured with a photoemission angle of $\Theta = 15°$. (b) XPS analysis reveals a systematic variation in the Sr/(Sr + Ti) ratio of the host lattice cations in the surface region (triangles) and in the bulk (squares) determined by ICP-MS, after dissolution of the STNNi thin films. (c) A slight shift in the diffraction position of the (002) Bragg peaks for non-stoichiometric STNNi is revealed by XRD analysis in 2θ-ω measurement geometry. Note that the shoulder, close to the (002) STO diffraction peak (light green), can be assigned to a second domain of the substrate. (d) Based on the diffraction angles of the (002) diffraction peaks, a relative expansion of the *c*-lattice parameter in reference to stoichiometric STNNi is evident. Solid black lines denote the stoichiometric point. Dashed lines serve as a guide for the eye.

To evaluate the thin film stoichiometry in the near-surface region, XPS is carried out. Fig. 5.2a shows representative XPS Sr 3*d*, Ti 2*p*, Ni 2*p* and Nb 3*d* core-level spectra, obtained from a stoichiometric STNNi thin film in the as-prepared state. The quantification of the Sr and Ti host cations is performed on the basis of the relative peak areas of the Sr 3*d* and the Ti 2*p* core level spectra. Here a Shirley-type background was subtracted and an STO single-crystal was used as a reference. The Sr / (Sr + Ti) ratio is plotted as a measure of stoichiometry in Fig. 5.2b. As can be seen, a systematic variation in the relative ratio of the host cations is evident (triangles). For comparison, the stoichiometry of the thin film bulk is investigated by ICP-MS after the dissolution of the STNNi thin films (squares). For this purpose, STNNi thin films were deposited on $NdGaO_3$ (NGO) substrates in a comparable range of laser fluences to prevent contamination of the solvent by cations of the substrate during the subsequent quantification of the dissolved amounts of strontium and titanium. As can be seen, changes in the surface and bulk stoichiometry reflect a similar trend, *i.e.* Sr-excess for thin films deposited with laser fluences below the stoichiometric point and Sr-deficiency for thin films deposited above the stoichiometric point is detected.

The incorporation of defect structures into the perovskite lattice of STNNi thin films is evident by XRD analysis (Fig. 5.2c). A slight shift in the position of the (002) diffraction peak for non-stoichiometric thin films, in reference to the diffraction peak obtained from stoichiometric STNNi indicates a small expansion of the of the perovksite lattice along the crystallographic *c*-axis. The average *c*-lattice parameter is calculated on the basis of the diffraction angles, obtained from the maxima of the (002) thin film diffraction peaks and the deviation to the *c*-lattice parameter of stoichiometric STNNi is plotted in Fig. 5.2d. Consistent with the stoichiometric changes, an expansion of the *c*-lattice parameter is visible for STNNi deposited above and below the stoichiometric point. Here, the accommodation of Sr-excess and Sr-deficiency results in strain, introduced to the perovskite lattice by the respective defect structures.[97, 175–177] Therefore, the magnitude of lattice expansion is sensitive to the extent of defect incorporation. In accordance with the literature, Sr-excess results in a more pronounced expansion of the *c*-lattice parameter than the accommodation of Sr-deficiency.[97]

Besides the mere expansion of the crystal lattice, the accommodation of defects results in a distortion of the perovskite thin film structure, *i.e.* the displacement of crystallographic planes. The relative degree of lattice distortion can be characterized by rocking curve analysis.[178–180] Representative rocking curves, obtained from STNNi in the as-prepared state and the reduced state (15 h, Ar / 4% H_2, 800°C) are shown in comparison to the rocking curve obtained from the underlying STO substrate in Fig. 5.3a. As can be readily seen, the rocking curve width of the thin film is increased in reference to the rocking curve of the substrate. The difference in the width indicates a decreased structural order of the epitaxial thin films, whereas the strontium titanate single crystal, typically fabricated by the Verneuil method [181], exhibits only a low defect density. However, also the coherence length for X-ray diffraction is significantly larger for the bulk STO crystal in comparison to the STNNi thin films of finite thickness.[182] A meaningful comparison of the lattice disorder is hence only possible for samples of similar thickness.

The full width half maximum (FWHM) of the rocking curve is a measure for relative differences in the structural disorder. As can be seen in Fig. 5.3b, STNNi thin films in the as-prepared state and deposited at the stoichiometric point, exhibit the lowest FWHM values and, accordingly, the lowest degree of lattice disorder. In comparison, the introduction of defects results in a relative increase of structural disorder, reflected by increased FWHM values. After thermal reduction of the STNNi thin films, the relative structural disorder is further increased for the majority of the samples. Here, the increased disorder is more pronounced for the Sr-deficient thin films. Most probably, the defect-chemical reactions triggered under the applied reduction conditions result in the reorganization of the thin film structure, for instance by nanoparticle formation in the thin film bulk. However, also the formation of secondary phases, in particular for defect-rich thin films, may influence the structural order.

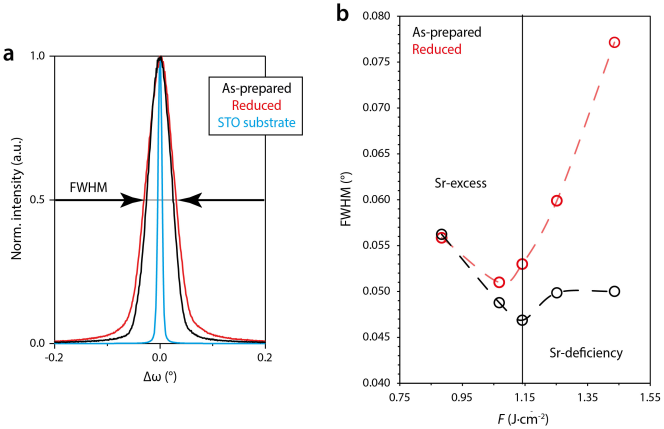

Figure 5.3: Rocking curve analysis of STNNi thin films. (a) Representative rocking curves recorded around the (002) diffraction peak of an STNNi thin film in the as-prepared state and after thermal reduction (15 h, Ar / 4% H_2, 800°C). A rocking curve that was recorded from the STO substrate is shown as a reference. (b) FWHM values of the rocking curves obtained in the as-prepared and reduced state of STNNi thin films deposited with different laser fluence. An increasing FWHM indicates an increasing distortion of the perovskite lattice.

5.2 Exsolution behavior in defect engineered STNNi

The exsolution response of the STNNi thin films of varying defect structure is evaluated by XPS analysis and by comparison of the particle population exsolved at the surface. As can be seen, in the as-prepared state, the Ni concentration is comparable for STNNi thin films deposited at different laser fluences (Fig. 5.4a). After thermal reduction (15 h, Ar / 4% H_2, 800°C) however, substantial changes of the Ni concentration can be observed. Most importantly, a considerable increase in the relative Ni concentration is evident for the initially stoichiometric STNNi thin film, while both, Sr-rich and Sr-deficient STNNi thin films exhibit no detectable increase in the Ni concentration in the near-surface region. In fact, the Ni concentration appears to be decreased for non-stoichiometric STNNi thin films after thermal reduction.

However, it needs to be taken into account that the surface geometry is altered after reduction, due to nanoparticle formation at the initially smooth crystal surface. Consequently, the surface of the STNNi thin films may be widely depleted from Ni, that accumulates in the evolving metallic nanoparticles. Therefore, quantification by XPS analysis is difficult, since it relies on a small probing volume determined by the limited information depth (inelastic mean free path of photoelectrons of a few nanometers). A relative comparison of samples in the as-prepared and in the reduced state, however, is possible. The decrease in the Ni concentration, apparent for most of the non-stoichiometric thin films, hence indicates that Ni supply by transport from the subsurface to the surface region is limited. In contrast, the stoichiometric perovskite host lattice may allow for a widely unhindered transport of Ni dopants to the perovskite surface.

The nanoparticle density is determined as a second parameter for the evaluation of the exsolution response. To avoid overestimation of the particle number due to surface decorations, which are likely to occur especially at surfaces of highly non-stoichiometric thin films, a lower threshold of 10 nm was used for the analysis of the topographical data obtained by AFM. Consistent with the XPS investigations, the highest nanoparticle density is detected at the stoichiometric point, while non-stoichiometry results in a decreased nanoparticle population at the crystal surface. It is worth to point out that the Ni concentration detected by XPS and the particle density are not directly correlated, presumably since the subsurface region of the oxide support considerably contributes to the XPS signal.

The role of the structural disorder of the STNNi parent material for the exsolution of embedded nanostructures becomes apparent, when plotting the particle density *versus* the FWHM values obtained by rocking curve analysis from the as-prepared thin films. In Fig. 5.5, a linear dependency is revealed, where low FWHM values result in the highest nanoparticle density. The relationship indicates that structural disorder hampers the mass transport of Ni dopants to the perovskite surface, while

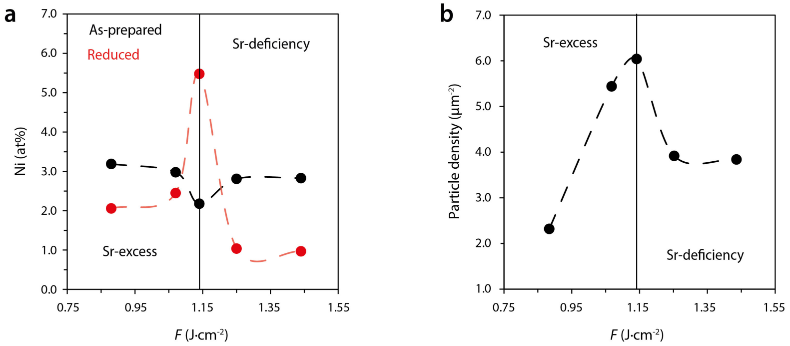

Figure 5.4: Evaluation of the exsolution response. (a) The atomic concentration of nickel determined by XPS analysis relative to the Sr, Ti and Nb cations, is shown for the as-prepared state denoted by black dots and after thermal reduction (15 h, Ar / 4% H_2, 800°C) denoted by red dots. (b) Particle density detected by representative AFM scans of 5 x 5 μm^2 as a function of the laser fluence. Dashed lines serve as guide for the eye.

a coherent perovskite structure may allow for the unhindered transport of Ni towards the surface. Here, defects may cause the trapping or slowing of Ni during the exsolution process, which results in a decreased exsolution dynamics *i.e.* a decreased exsolution strength.

5.3 Discussion: Control of metal exsolution based on embedded nanostructures

The defect structure of STNNi is tailored based on the growth conditions applied during pulsed laser deposition. Non-stoichiometry in strontium titanate, controlled by the systematic variation of the laser fluence, results in Sr-excess or Sr-deficiency. The incorporation of defects during the off-stoichiometric PLD growth is evident from the linear shift in the Sr/(Sr+Ti) ratio and the expansion of the STNNi perovskite lattice in *c*-direction. The strongest exsolution response for STNNi is observed for stoichiometric thin films. This finding appears to be in contrast to the well-established exsolution models that describe the exsolution behavior in relation to the host lattice stoichiometry.[19]

In accordance with the literature, the affinity for the exsolution of Ni cations decreases with increasing Sr-excess in STNNi. In general, the spontaneous exsolution of B-site metals results in an increase in the A / B-site occupancy, which favors the spontaneous exsolution of B-site metals in A-site cation deficient perovskite oxides, since the stoichiometric perovskite structure may be recovered by the process.[19] In contrast, A-site excess results in a reduced affinity for the exsolution of B-site

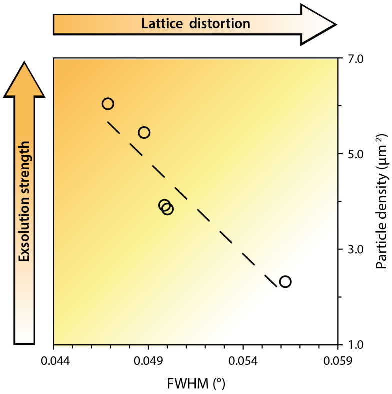

Figure 5.5: The FWHM values determined by XRD rocking curve analysis correlates with the average particle density at the crystal surface of STNNi thin films. The linear relationship indicates, that increasing structural disorder of the STNNi parent material results in a decrease in the exsolution dynamics. In contrast high structural coherency of the perovskite lattice enables a widely unhindered mass transport of Ni to the surface during metal exsolution.

cations. The presence of Sr-rich surface phases in particular, has been proposed to effectively block the formation of surface nanoparticles during redox exsolution in ceramic compounds.[19] Notably, Sr-rich RP-type surface phases, that may act as blocking layer, were reported to form at strontium titanate single crystals due to surface reconstructions.[19, 148] In addition, the surface termination may strongly influence the oxygen exchange kinetics of the strontium titanate parent material. Here, SrO-termination of the surface was reported to result in a considerably decreased oxygen exchange kinetics in comparison to TiO_2-terminated STO crystals.[84] Therefore, the dynamics of exsolution in Sr-rich parent materials may be additionally decreased by a decreased dynamics of deoxygenation during thermal reduction.

Surprisingly for STNNi thin films, also Sr-deficiency results in a decreased exsolution strength in STNNi. Considering the formation of Ni-rich nanostructures in the as-prepared thin films, the observed behavior is consistent with the common exsolution model. In solid solution parent materials, the exsolution response must include the phase separation of reducible dopants from the perovskite structure and the transport of the dopants towards the surface, where the introduction of A-site vacancies targets the destabilization of the perovskite structure to promote the spontaneous phase separation of B-site cations. In STNNi, the phase separation of Ni dopants is unnecessary, as the nickel dopants are mostly present in the form of separated, embedded nanostructures already in the as-prepared material (notably, the formation of self-assembled Ni-rich nanostructures was observed independent

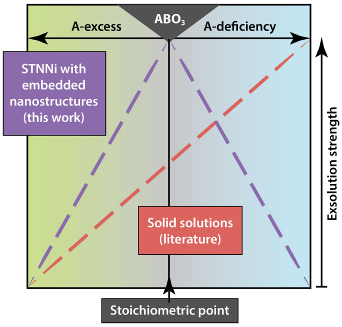

Figure 5.6: Schematic illustration of the role of A-site defects on the exsolution behavior. The influence of A-site cation defects on the exsolution response depends on the nature of the parent material. For solid solutions, increasing A-site deficiency can be used to increase the exsolution strength. For the exsolution of pre-formed embedded nanostructures any non-stoichiometry, *i.e.* A-site excess and also A-site deficiency hampers the exsolution of dopants to the surface.

from thin film stoichiometry). The phase separation step hence can not be affected by defect engineering. Therefore, dopant separation and dopant transport need to be considered as widely decoupled steps of the exsolution response for the present material system. Nanoparticle formation at the surface of STNNi during redox exsolution consequently, is mostly determined by the dynamics of dopant transport. The detected exsolution trend hence reveals a detrimental effect of defects on the exsolution dynamics, that is most probably based on the interaction of exsolving species during mass transport towards the surface region.

Remarkably, the role of defects becomes apparent by structural investigations. An increasing degree of lattice distortion results in a decreased concentration of Ni in the near-surface region and in a smaller nanoparticle population at the STNNi crystal surface. The exsolution strength is hampered by a distorted perovskite lattice, that originates from lattice defects and that is evident from the inverse correlation between the nanoparticle density with the respective FWHM values of XRD rocking curves. Here, the presence of charged defects may result in Coulomb interactions with Ni ions during the diffusion towards the surface.[30] Furthermore, local strain fields induced by defect structures may result in a trapping effect.[27, 30] Notably, extended defects were previously shown to serve as preferential nucleation sites for exsolution nanoparticles.[183] Interestingly, the exsolution strength is affected in a similar manner for Sr-rich and Sr-deficient STNNi defects. Hence, the nature of the defects appears to be not decisive for the trapping effect.

Metal exsolution of dopants, that are present in the form of nanostructures which are coherently embedded in the crystal lattice of perovskite parent materials, exhibits a different exsolution behavior than exsolution in solid solutions. As illustrated in Fig. 5.6, different strategies need to be applied to increase the nanoparticle yield at the perovskite surface. In solid solution parent materials, control of the stoichiometry is a powerful lever to control the exsolution strength (red curve). A high amount of A-site vacancies promotes metal exsolution to the surface. For the exsolution of embedded structures however, a stoichiometric host lattice is favorable to allow for the unhindered mass transport of dopants to the perovskite surface (purple curve). Any deviation from the stoichiometric point results in a decreased exsolution strength.[147]

Chapter 6

Dynamics of the exsolution response

In this chapter, strategies to disentangle the surface and bulk exsolution response are developed, to investigate the exsolution process over time. Consequently, the focus of the following discussion lies on the dynamics of nanoparticle exsolution. Among other (*ex-situ*) techniques, *in-situ* diffraction analysis and *in-situ* spectroscopy are applied to monitor the bulk structural changes and the evolution of the surface chemistry of the sample, while driving redox processes by control of the temperature and the ambient atmosphere and to link the chemical and structural changes to the morphological evolution of the surface during nanoparticle growth. Please note that the data discussed in this chapter was partly published in reference [184].

6.1 Structural relaxation of the host lattice

As elaborated in section 4, the structural properties of the present material system are determined by several parameters including epitaxial strain induced at the vertical, semi-coherent interface between perovskite host and the embedded NiO_x phase, which has domain-matching character. The change of the chemical nature of the vertical interface during reduction of the embedded Ni-rich nanostructures allows to follow the kinetics of the phase transition *e.g.* the dynamics of the formation of metallic nanoparticles in the oxide bulk. Due to the clamping effect of the substrate, the degrees of freedom of the thin film lattice to compensate structural changes is limited to the (001) crystallographic axis. The corresponding change in the *c*-lattice parameter can be determined on the basis of XRD measurements in 2θ-ω measurement geometry.

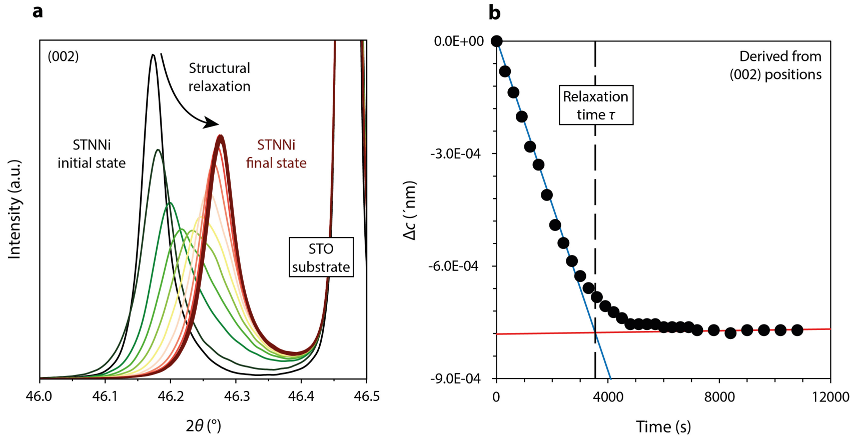

Figure 6.1: HT-XRD analysis of STNNi in reducing atmosphere. (a) Representative plot of a series of diffractograms, revealing a shift in the (002) thin film diffraction peak over time. The thin film signal shifts from higher diffraction angles (initial state) to lower diffraction angles (final state) and reflects a relaxation of the perovksite lattice in *c*-direction. (b) Representative plot of the relative change in the *c*-lattice parameter as determined based on (a). Linear fitting of the two linear regions of the curve is performed to determined the relaxation time τ. The thin film thickness is 400 nm. The annealing conditions during the measurement of the exemplary data shown were 4% H_2 / Ar, T = 700°C (backside temperature).

Thermal reduction successively alters several properties of the oxide lattice. Most importantly, the chemical nature of the NiO_x inclusions and hence the domain-matching relationship and the corresponding residual misfit F_{CSL} at the semi-coherent interface, but also the oxygen vacancy density, the dopant concentration of the host lattice *i.e.* the cation (Ni) vacancy density, and potentially, the valence state of transition metal cations may be influenced. By application of HT-XRD, the structural relaxation of the host perovskite lattice can be monitored *in-situ* during the reducing thermal treatment, to investigate the time-dependent bulk response of the host lattice during metal exsolution.

Here, an enclosed sample chamber enables the control of the ambient atmosphere *via* the gas supply, while the sample temperature is controlled by a heated sample stage. While the chamber was initially purged with oxygen, the reduction process is initiated by rapid exchange of the ambient atmosphere with 4% H_2 / Ar gas mixture after stabilization of the processing temperature. Here, a STNNi thin film with a thickness of 400 nm was used for the analysis to provide for a sharp diffraction peak.

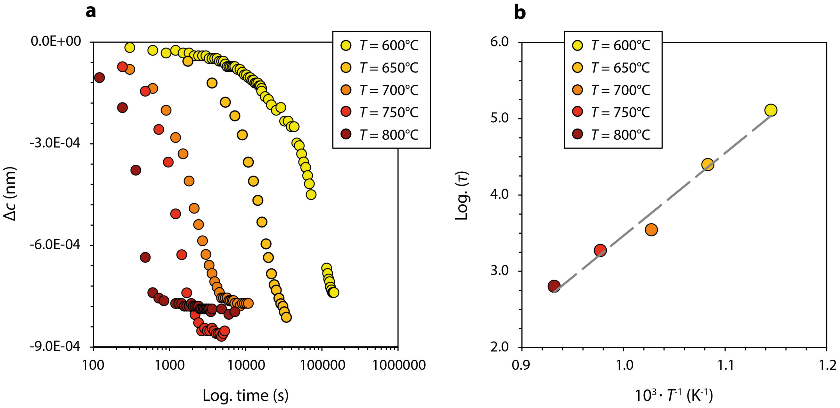

Figure 6.2: Structural relaxation of the STNNi perovskite lattice as a function of time measured in reducing atmosphere by high-temperature XRD analysis. (a) Relative change of the *c*-lattice parameter over time measured at different temperatures in the range between $T = 600°C - 800°C$. (b) Arrhenius-type plot of the logarithmic relaxation times determined at different temperatures *versus* the reciprocal temperature. A linear relationship is revealed that indicates a temperature-activated reaction underlying to the structural relaxation. The thin film thickness is 400 nm. The measurements were performed under continuous gas flow of 4% H_2 / Ar at different backside temperatures.

A representative HT-XRD plot with a series of 2θ-ω-scans is shown in Fig. 6.1a, which was recorded at T = 700°C, where a measurement was carried out each 300 s respectively (varies for measurements at different temperatures). The thin film diffraction peak is visible at a lower diffraction angle in the initial state, (denoted in black), while after thermal reduction, a slightly broadened diffraction peak of lower intensity can be observed at higher diffraction angles (denoted in red). As can be seen, the diffraction peak starts to broaden and, simultaneously to decrease in intensity, while successively shifting to higher diffraction angles. The width of the thin film peak presumably reflects local differences in the structural properties across the thin film correlated to the phase transition of the NiO_x phase towards nickel metal. Over time, a vertex is reached, and the diffraction peaks start to narrow again, while increasing in intensity. After a while, no further shift in the diffraction angle is detected, which marks the final state of the fully reduced STNNi thin film lattice.

Based on the *c*-lattice parameter, derived from the (002) diffraction angle, the change in the *c*-constant referenced to the initial value is plotted *versus* the annealing time in Fig. 6.1b. As can be seen, a linear shift of the averaged lattice parameter over time is apparent. After a while the curve flattens, which indicates that the final state of reduction is reached and no further changes in the lattice constant occur. The relaxation time τ is determined by linear fitting of the linear parts of the data curve at the point of interception of the two lines and the respective intercept with the time-axis.

The dynamics of the structural relaxation of the perovskite lattice was investigated at different temperatures in the range between T = 600 - 800°C (Fig. 6.2a). Notably, the temperatures denote the set values *i.e.* the temperature measured at the backside of the sample stage, where the heating coil is located. As can be seen, higher temperatures result in an accelerated structural relaxation, while at lower temperatures, long annealing times are required to complete the process. The rate of the structural relaxation hence is related to a characteristic relaxation time. Based on the relaxation times, determined at different temperatures, an Arrhenius plot can be generated (Fig. 6.2b). The Arrhenius equation, given below (equation 6.1), describes the temperature-dependency of the reaction rate k.

$$k = A \cdot e^{\frac{-E_\mathrm{A}}{k_\mathrm{B} \cdot T}} \tag{6.1}$$

Here, k is the rate constant, A is the frequency factor, E_A is the activation energy of the reaction, k_B is the Boltzmann constant and T is the temperature. Fig. 6.2b shows the Arrhenius plot in its logarithmic form as given by equation 6.2.

$$log(k) = log(A) - \frac{-E_\mathrm{A}}{2.303 \cdot k_\mathrm{B} \cdot T} \tag{6.2}$$

A linear relationship is revealed, which indicates a temperature-activated process underlying the structural changes of the host lattice. In principle, the activation energy can be determined from the experimentally obtained data on the basis of the slope of the Arrhenius plot. Here, an activation energy of E_A = 2.1 eV was determined. The activation energy is found to be on the upper limit of experimentally determined values for the activation enthalpy of oxygen vacancy migration in strontium titanate reported in literature[84], where most studies, however, find lower values. Typical values are in the range between $\Delta H_{\mathrm{mig},\, \mathrm{V}_\mathrm{O}^{\bullet\bullet}}$ = 0.62 - 0.67 eV.[101]. It is important to note the determined activation energy may well reflect more than a single process, and comparison to literature values can only serve as a guideline.

This finding may indicate that the reaction underlying process may depend not only on oxygen diffusion, but relies on a reaction of higher complexity. For instance, cation diffusion along the semi-coherent interface may be required during the restructuring of the domain matching registry between the crystal lattice of the embedded and the host phase. Alternatively, oxygen transport from the oxide bulk to ambient may be hindered in a way that additional energy is required to drive the reduction process. For example, the presence of space charge regions at the surface of complex oxides where shown to cause a strong increase in the activation energy and to limit oxygen transport dramatically.[84, 185]

However, the results must be taken with care since the applied measurement setup does not allow for a measurement of the temperature at the surface of the thin film sample, but relies on the temperature sensor installed at the backside of the heated sample stage. Deviations between the nominal and the real sample temperature are hence rather likely. Furthermore, it needs to be considered that an increased oxygen deficiency of the as-prepared samples may result from the PLD growth of the thin films, which can influence the oxygen exchange kinetics (chemical diffusion *vs.* self-diffusion). Yet, equilibration of the thin films samples upon heating in O_2 is expected to proceed fast.[186] Also, it is worth pointing out that HT-XRD analysis provides averaged information, which may be the result of multiple processes induced by the reducing treatment. Secondary processes, which are not directly linked to the targeted reaction may influence the average lattice parameter and may cause a deviation of the measured value from the real activation energy. The parameters that influence the structural properties of the perovskite lattice were elaborated in detail in chapter 4. Moreover, at elevated temperatures, thermal expansion of the crystal lattice needs to be taken into account, which will influence the average lattice parameter. The determination of the exact activation energy of the reaction thus may be difficult. Based on the observation of a distinct linear relationship in the Arrhenius plot however, a clear temperature-dependency of the bulk exsolution response, *i.e.* of the formation of metallic nanoparticles within the perovskite lattice is evident.

6.2 Surface chemistry changes

Near ambient-pressure X-ray photoelectron spectroscopy (NAP-XPS) is applied to probe the surface chemistry *in-situ* during metal exsolution.[1] The technique enables the measurement of the electronic structure of the surface while redox processes are driven by temperature control of the sample and control of the ambient atmosphere. In order to be sensitive to the dynamics of the process, a moderate temperature of $T = 400°C$ is applied to investigate the exsolution response. The reduction temperature is low in comparison to the HT-XRD analysis applied to investigate the bulk response. In accordance with the findings presented above, the bulk response is thus mostly absent. No detectable shift in the thin film diffraction peak can be observed after thermal reduction at $T = 400°C$ for 5 h (Fig. 6.3a, (*ex-situ*)). Yet, the formation of nanoparticles with very high coverage of the surface can be observed by AFM as can be seen in Fig. 6.3b (*ex-situ*).

---

[1] The NAP-XPS experiments were performed in collaboration with by B. Šmíd (Charles University, Department of Surface and Plasma Science, 18000 Prague, Czech Republic) whose support is highly appreciated.

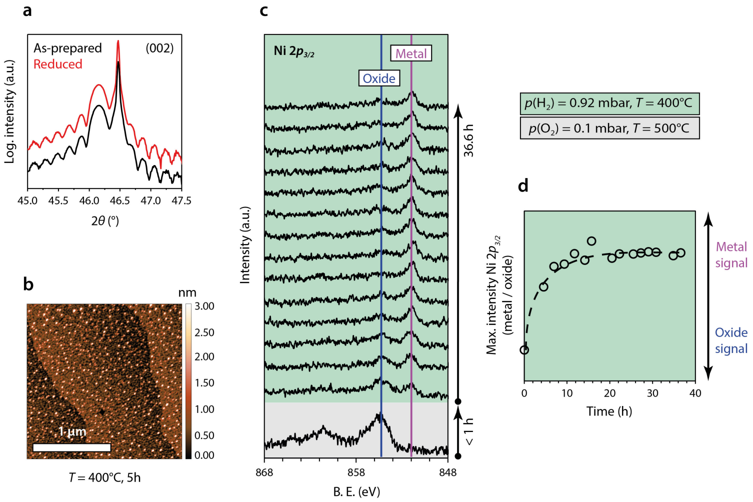

Figure 6.3: Investigation of the exsolution response at low temperatures. (a) XRD analysis reveals no detectable shift in the diffraction peak *i.e.* no structural relaxation of the host lattice; (b) AFM surface imaging reveals nanoparticle exsolution at the thin film surface after reduction at T = 400°C for 5 h under continuous gas flow of 4% H_2 / Ar. The scan size is 2 x 2 µm^2 with a scale bar of 1 µm. The thin film thickness is 50 nm. (c) Probing of the surface chemistry during metal exsolution by *in-situ* spectroscopy investigations of the Ni $2p_{3/2}$ core level spectrum by NAP-XPS during reducing sample treatment at elevated temperatures. The binding energies of the plotted spectra were corrected to the Ti $2p$ position and the intensity was normalized to the pre-peak region. (d) Evaluation of the exsolution dynamics during reducing treatment, based on the signal ratio of the metal and oxide feature derived from (c). Data points are given as black circles and a dashed line is given as guide for the eye. For NAP-XPS investigations STNNi was deposited on conductive Nb:STO substrates. The thin film thickness is 20 nm. Modified from ref. [184].

After heating the sample in oxygen atmosphere up to $T = 500$°C (< 1 h) to desorb carbon species from the thin film surface, the sample temperature is stabilized at $T = 400$°C and the exsolution process is induced by introduction of hydrogen gas ($p = 0.92$ mbar) into the XPS chamber. The surface chemistry is investigated on the basis of the cation core-level spectra, *i.e.* Ni $2p_{3/2}$, Ti $2p$, Sr $3d$ and Nb $3d$, as well as the oxygen O $1s$ spectrum. Notably, the following analysis is limited to the evolution of the Ni signature, while the more subtle changes in the core-level spectra of the other cations will be discussed in another context in chapter 7.

The Ni $2p_{3/2}$ core-level region provides valuable information about the Ni chemistry. The measured spectra are the result of multiple emission lines due to spin-orbit interactions as well as charge-transfer effects. Herein, the peak centered at about B.E. ~855.6 eV is a suitable fingerprint for the oxidized state, while a peak centered at about B.E. ~851.9 eV corresponds to the metallic state of nickel

(Fig. 6.3c).[187–189] Minor deviations from the binding energies measured on the basis of bulk reference materials may originate from size effects commonly observed for small metal clusters as well as cluster-support (oxide substrate) interactions.[190–193] Initially a pure oxide signature is visible in the Ni $2p_{3/2}$ core-level spectrum while after start of the reduction the evolution of a metal signature occurs. The exsolution dynamics is evaluated on the basis of the intensity ratio of the oxide and the metal signal, which is determined for spectra, which were typically accumulated over 50 scans, respectively. The evolution of the Ni $2p_{3/2}$ signature over time is shown in Fig. 6.3c, and the corresponding evolution of the metal / oxide intensity ratio derived from the normalized data is given in Fig. 6.3d.

A rapid evolution of the metallic signal is evident based on the relative increase of the low binding energy signal, while at the same time the oxide signal decreases over time. Initially, a jump in the relative metal / oxide ratio is evident (Fig. 6.3d), that reflects the fast surface exsolution response after $\sim$4.5 h. The ratio saturates during the further reduction and remains at a constant level after around about $\sim$10 h of sample annealing. While a meaningful quantification of the surface stoichiometry is hampered by the ongoing topological changes of the probing geometry, the stabilization of the metal / oxide ratio, gives evidence that the exsolution of metallic nanoparticles proceeds fast, *i.e.* within a few hours, even at low temperatures.

These findings strongly indicate that the nanoparticle growth at the surface and the structural changes of the perovskite lattice during exsolution is not directly interrelated. The interpretation of data obtained by bulk-sensitive techniques hence must be interpreted with great care, since it does not necessarily allow sound conclusions about the surface exsolution response.

6.3 Particle formation and surface limitations

In order to link the structural and chemical changes during exsolution with the formation of Ni nanoparticles, the temperature-dependent particle growth is investigated by surface imaging. The surface morphology of four pieces of epitaxial STNNi, that were cut from the same thin film sample, are displayed in Fig. 6.4. To improve visibility, a scan of 5 x 5 μm^2 (below) and a scan of 2 x 2 μm^2 (above) are shown, respectively. Here, the morphology of the stepped, as-prepared (001) crystal surface is compared to the morphology of thin films which are decorated with exsolved nanoparticles after thermal reduction at $T = 600°C$, $T = 700°C$ and $T = 800°C$ for 30 h respectively.

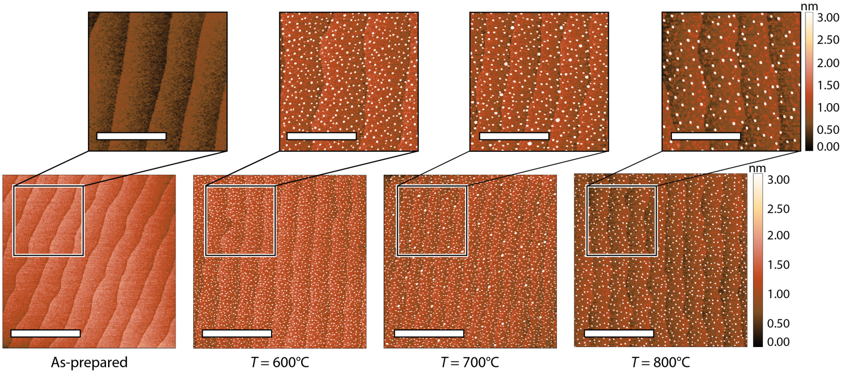

Figure 6.4: AFM surface imaging of epitaxial STNNi samples which were cut from the same thin film in the as-prepared state and after reducing thermal treatment at $T = 600°C$, $T = 700°C$ and $T = 800°C$ (4% H_2 / Ar, 30 h). The scan size is 5 x 5 μm^2 with scale bars of 2 µm for the images shown below, while the scan size is 2 x 2 μm^2 with scale bars of 1 µm for the images shown above. Modified from ref. [184].

The atomically smooth crystal surfaces of the epitaxial thin films enable the determination of nanoparticle characteristics by AFM imaging. As can be readily seen, the size and distribution of the exsolved nanoparticles strongly depends on the reduction conditions, where lower temperatures result in smaller particle sizes as well as in a higher particle density.

A more detailed characterization of the nanoparticle properties was performed by statistical evaluation of the topological data obtained by AFM analysis. Apart from the particle density (the threshold applied for detection was 1 nm), the median of the particle diameter, particle height and the sum of the average nanoparticle volume is determined. As can be seen in (Fig. 6.5, left), the nanoparticle density decreases considerably with increasing reduction temperature, from about ∼140 particles / μm^2 at $T = 600°C$ to ∼50 particles / μm^2 at $T = 800°C$ (purple symbols), while the particle size is increasing from an average diameter of ∼25 nm to ∼40 nm (green symbols) and the average height of ∼3 nm to ∼6 nm (blue symbols). The sum of the exsolution volume however, remains approximately constant independent from temperature (Fig. 6.5, right). Additionally, these observations indicate that the nanoparticles do not grow from the bulk, but rather grow at the surface after the mass transport of Ni dopants due to coalescence.

If the process of metal exsolution is considered as an issue of diffusive transport of Ni ions in the bulk and a reduction reaction at the surface that acts as a sink for Ni ions, the amount of Ni at the surface can be expected to increase with increasing reduction temperature (and time), since the materials chemistry is expected to

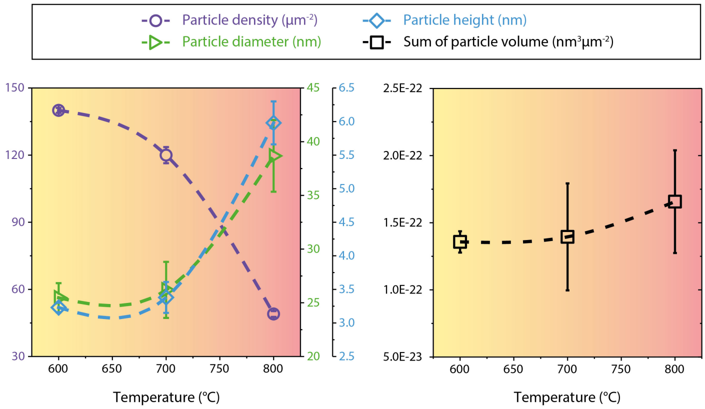

Figure 6.5: Evaluation of the nanoparticle properties. The particle characteristics are determined based on the topological data obtained by AFM imaging from the samples shown in Fig. 6.4. Averaged values obtained from three 5 x 5 µm^2 scans are plotted respectively; the error bars are based on standard deviations. Notably, solely the volume of the part of the particles that penetrate the surface is detected. The thin film thickness is 20 nm. Modified from ref. [184].

reach a state of thermodynamic equilibrium with respect to the ambient annealing conditions with increasing rate. In contrast to expectation, however, the detected difference in the sum of the exsolved nanoparticle volume after annealing at different temperatures for an equal duration is not statistically significant (Fig. 6.5, right). A possible explanation for these findings may be that all Ni dopants have been exsolved from the thin film bulk during reduction in the entire range of applied annealing conditions, so that the process is not limited by time or temperature, but by the supply of nickel dopants. If this were the case, the perovskite bulk of the sample would be widely depleted of nickel after the reducing treatment. To examine the extent of depletion of the perovskite host lattice from exsolution-active nickel dopants, SIMS analysis was carried out.[2] The concentration profiles were measured by depth-profiling after capping the samples by evaporated platinum to avoid irregular sputter effects at the surface.

Surprisingly, no concentration gradient across the thin film samples is detected by SIMS depth-profiling, irrespective of the reduction temperature (Fig. 6.6a). This finding suggests that only a small fraction of the total amount of dopants is exsolved to the surface of the perovskite thin film, while predominantly remaining in the bulk in the form of embedded metallic nanoparticles (*cf.* section 4.3). Please

---

[2] The SIMS measurements were performed by U. Breuer (Central Institute for Engineering, Electronics and Analytics (ZEA-3), Forschungszentrum Jülich GmbH, 52425 Jülich, Germany) whose support is highly appreciated.

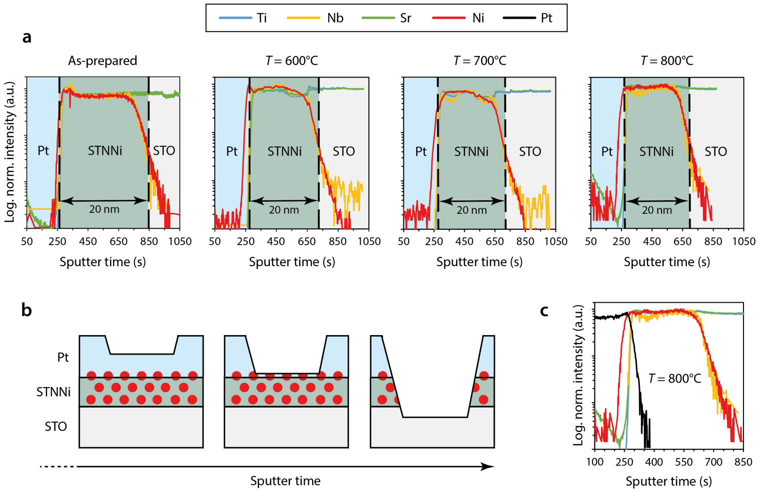

Figure 6.6: (a) Concentration profiles of Ti, Sr, Nb, and Ni cations determined by SIMS profiling. The measurements were obtained from the samples presented in Fig. 6.4 after the surface was covered with 30 nm of evaporated platinum. The Ni concentration appears to be constant in the thin film bulk independent from the sample state, while after reducing treatment Ni accumulation at the surface is detected based on the early increase of the Ni signal in comparison to the other cations. Dashed lines denote the Pt-to-thin film interface as well as the thin film-to-substrate interface. (b) Schematic sketch of the sputtering process, that illustrates the detection of exsolved Ni nanoparticles by SIMS. (c) Cation depth profiles obtained from the sample that was reduced at T = 800°C including the Pt signal which originates from the protective cover layer. Modified from ref. [184].

note, that the sputter time differs for samples in the as-prepared and the reduced state due to differences in the sputter yield. The exsolution width of dopants contributing to the formation of nanoparticles at the surface thus appears to be strongly limited to the topmost surface region of the parent material. The accumulation of nickel at the surface in form of nanoparticles after reduction is visible in the SIMS profiles in form of an early increase of the nickel signal compared to the Ti / Sr host cations and Nb-dopants. Here, the sputter process allows to probe the chemistry at the platinum-to-thin-film interface as illustrated in Fig. 6.6b. The position of the interface is determined based on the steep increase of the Ti / Sr host cations, since the Pt signal suffers from a tailing feature, which originates from occasional sputtering events at the walls of the sputter crater and potentially intermixing, when crossing the Pt top layer to a Pt-free bottom layer (Fig. 6.6c). To determine the position of the thin film-to-substrate interface however, one relies on the Nb / Ni cation profiles, which consistently exhibit a similar tailing feature.

These findings indicate that the fraction of nickel dopants that exsolves from STNNi to the surface is fixed and represents only a small part of the total amount of dopants in the parent material. Consequently, the exsolution width, and hence the amount of dopants accessible for the nanostructuring *via* metal exsolution appears to be strongly limited to the surface region of the perovskite. The final nanoparticle properties are most likely determined by subsequent particle growth *via* Ostwald ripening, that is hence strongly influenced by the temperature applied during sample reduction (*cf.* Fig. 6.4 and Fig. 6.5).

In order to investigate the apparent limitation of the exsolution process to the surface region in more detail, the thin film thickness is varied to systematically change the surface-area-to-volume ratio of the samples. Here, the thin film thickness is tailored in the range between 10 - 61 monolayers of STNNi by means of RHEED-monitoring (Fig. 6.7a), corresponding to a thickness between $\sim$ 3.9 nm and $\sim$ 23.9 nm. The surface roughness is comparable for all samples and varies between RMS $\sim$114 pm - 150 pm as determined by AFM investigations of the as-prepared thin films.

A thermal reduction step at $T = 600°\text{C}$ is applied for 5 h under continuous gas flow of 4 % H_2 / Ar gas mixture to induce the exsolution of nickel. Given the rapid exsolution response of the material (*cf.* section 6.2), the exsolution process can be expected to be mostly completed for all samples under the applied conditions. The exsolution response is compared by statistical evaluation of the nanoparticle properties as summarized in Fig. 6.7b. Nanoparticles of similar height $\sim$3.8 nm and similar diameter of $\sim$20 nm form at the surface of the thin films of different thickness. Notably, the particle dimensions are well comparable to the nanoparticles exsolved at $T = 600°\text{C}$ discussed above (*cf.* Fig. 6.5, left). Only a minor difference, *i.e.* a slightly smaller particle diameter and lower particle height was detected which is most probably related to the shorter annealing time (5 h *vs.* 30 h). Generally, this observation indicates that the coalescence of the nanoparticles is slow at low temperatures of $T = 600°\text{C}$.

In conclusion, the nanoparticle dimensions are not significantly influenced by the thin film thickness, that means a larger reservoir of nickel dopants. It is worth to point out, that the nanoparticle density, however, increases with the doping concentration (*cf.* appendix D). The most striking result to emerge from the data is that the nanoparticle density decreases with increasing thickness of the thin film samples, which directly correlates to a decreased sum of the nanoparticle volume detected at the perovskite surface. The fact that the sample thickness does not limit the exsolved dopant volume is a strong indication that the exsolution width is narrower than the minimal thin film thickness applied during the study, which is < 10 monolayers.

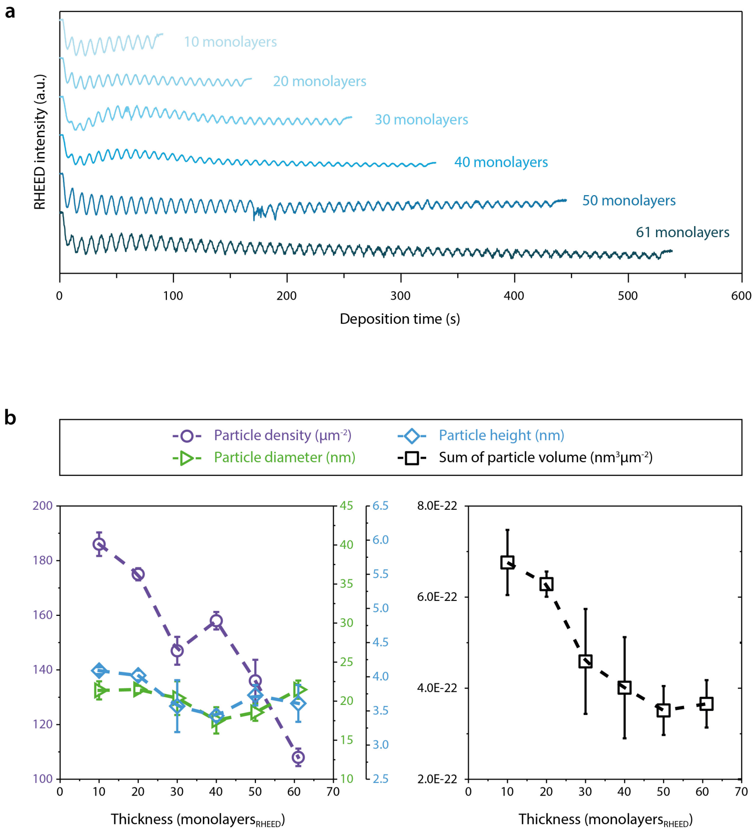

Figure 6.7: Evaluation of the nanoparticle properties for epitaxial STNNi thin films of systematically varying thickness. (a) RHEED-monitoring is used to control the thin film thickness between 10 - 61 monolayers during pulsed laser deposition. (b) The particle characteristics are determined based on the topological data obtained by AFM imaging from the samples. Averaged values obtained from three 2 x 2 μm^2 scans are plotted respectively; the error bars are based on standard deviations. Notably, solely the volume of the part of the particles that penetrate the surface is detected.

The origin of the increased nanoparticle density for decreasing thin film thicknesses remains to be elucidated. The size, shape and distribution of VANs can be very diverse[156, 157, 159, 194, 195], and the dimension of the perovskite matrix may influence the properties of the nanostructures. For instance, initial accumulation of Ni-rich nanophases may be finely dispersed, but may consolidate with increasing thin film thickness to form larger (nano)structures, which would strongly influence the subsurface distribution of reducible dopants and may result in a higher nanoparticle density. The investigation of buried nanostructures in thin films of only several nanometers in thickness, however, is extremely challenging and future research will be needed to understand if and how the distribution of embedded nanostructures impacts the nanoparticle formation at the perovskite surface during redox exsolution.

6.4 Simultaneous chemical and structural investigations of the STNNi surface

Coupled NAP-XPS and grazing incidence X-ray scattering (GIXS) was employed to simultaneously investigate the chemical and structural evolution of the STNNi surface *in-situ* during metal exsolution.[3] Details on the technique and on the experimental setup can be found in reference [138]. The method provides unique insights on the self-assembly of metallic nanoparticles at the STNNi surface and with high time-resolution enabled by the high flux of the photon beam generated by a synchrotron X-ray source. Notably, this section is kept brief, since the analysis of the experimental data and in particular the simulation of complementing scattering patterns are ongoing work. Therefore, the preliminary analysis is presented as an outlook.

NAP-XPS is used to probe the surface chemistry during metal exsolution on the basis of the Ti 2*p* and the Ni 3*s* / Ti 3*s* core-level region, while the structural properties of the surface is probed by GIXS (Fig. 6.8). Here, the as-prepared state is analyzed at (0) room temperature and after several, consecutive intervals of thermal reduction at $p(H_2)$ = 1.3 mbar after (1) 30 min, T = 400°C; (2) 90 min, T = 400°C and (3) 80 min, T = 500°C. The measurements where performed in UHV conditions after each reduction step, respectively, before the next reduction interval was initiated by exchange of the ambient gas environment back to H_2.

In the as-prepared state of the thin film sample, the Ti 2*p* core-level exhibits a typical signature found for strontium titanate, where no significant changes can be observed in the course of thermal reduction (Fig. 6.8a). Similarly, no shifts of the Ti 3*s*

---

[3] The NAP-XPS/GIXS experiments were performed by H. Kersell and S. Nemšák (Advanced Light Source (beamline 11.0.2), Lawrence Berkeley National Laboratory, CA 94720 Berkeley, USA) whose support is highly appreciated.

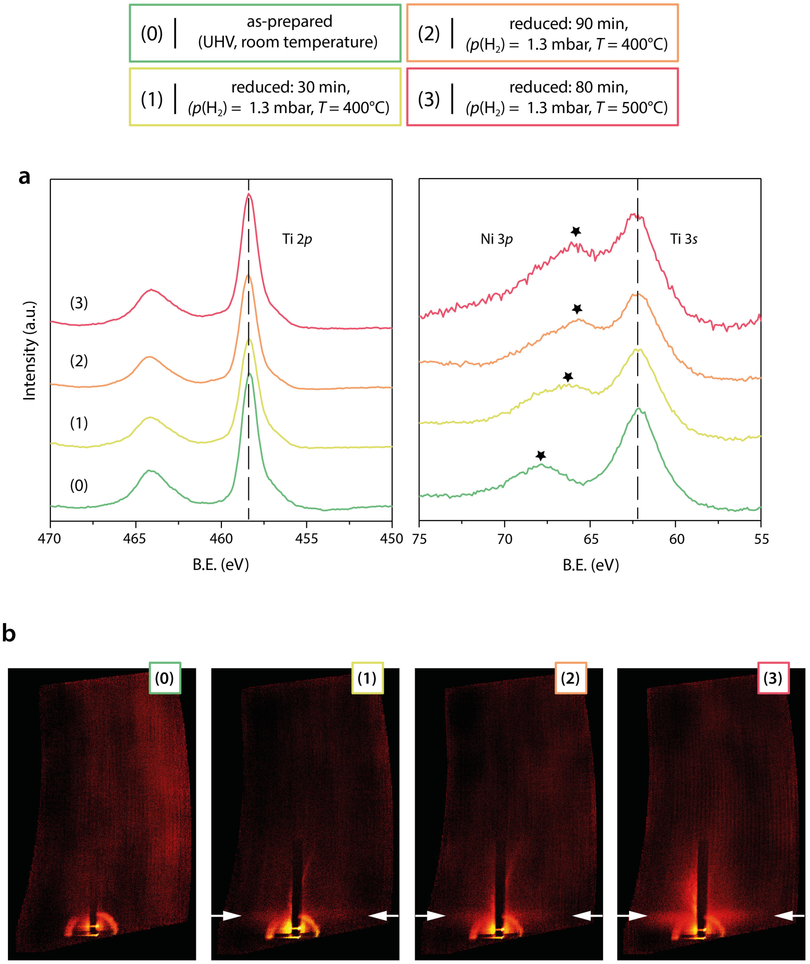

Figure 6.8: *In-situ* investigation of the coupled chemical and structural evolution of the STNNi surface during thermal reduction by combined synchrotron-based AP-XPS and GIXS measurements. (a) Probing of the surface chemistry during metal exsolution by *in-situ* spectroscopy of the Ti 2*p* and the Ni 3*s* / Ti 3*s* core-level spectra. The binding energies of the plotted spectra were corrected by means of the Ti 2*p* position (set to the nominal value for $SrTiO_3$ B.E. = 458.4 eV. The intensity of the Ti 2*p* spectrum was normalized to the pre-peak region, while the intensity of the Ni 3*s* spectrum was normalized to the post-peak region. The spectra are shown with an offset on the y-axis and the peak maximum of the Ni 3*s* signal is denoted by an asterisk. (b) Scattering patterns obtained from the STNNi surface during the thermal treatment under equivalent conditions to the NAP-XPS data shown in (a) A scattering feature evolving during the thermal treatment is highlighted by white arrows. For NAP-XPS investigations STNNi was deposited on conductive Nb:STO substrates. The thin film thickness is 30 monolayers.

core-level signal is visible. The Ni 3*s* and the Ti 3*s* signals partially overlap, however the peak maxima appear to be clearly separated for the as-prepared state. With the start of the thermal reduction a shift of the Ni 3*s* peak maximum towards lower binding energies as well as a broadening of the signal can be observed. Similarly, to the discussions on the Ni 2*p* signature presented above (*cf.* section 6.2), the shift to lower binding energies indicates the formation of metallic Ni species at the STNNi surface, while the peak broadening, in particular visible for the spectrum that was recorded after 30 min of reduction, is related to a mixed oxide / metal signal. With increasing reduction time, the B.E. shift increases and the intensity valley between the Ni 3*s* and the Ti 3*s* peaks becomes shallower, while after 90 min of reduction no further changes are observed. Also at an increased temperature of T = 500°C no significant differences in the signature are detected. Notably the Ni 3*s* / Ti 3*s* intensity ratio appears to increase during reduction which may indicate the continuous accumulation of Ni dopants at the STNNi surface.

The absence of scattering centers at the smooth perovskite crystal surface results in a weak signal recorded by the bidimensional detector during GIXS in the as-prepared state (Fig. 6.8b). Here, the signal is dominated by the primary beam, which is mostly blocked by means of a beam stop (black shadow visible). After 30 min of reduction a faint feature evolves in the scattering pattern which is visible as a diffuse horizontal streak, also known as Yoneda line (highlighted by white arrows), correlated to the nucleation of nanoparticles at the surface. The specific intensity distribution provides information about the evolution of the nanoparticle properties such as size and shape as well as their structural relationship with the host oxide, which can be studied by comparison of the experimental results with simulated scattering patterns. Here, preliminary results indicate that the nanoparticles remain partly embedded within the oxide surface, while growing in size. with increasing time and temperature of the reducing annealing.

The findings emphasize the rapid exsolution response of STNNi at low temperatures as discussed above. Moreover, the observations indicate that the exsolution of embedded nanostructures (*cf.* chapter 4) results in the formation of anchored metal nanoparticles similar to the exsolution of nanoparticles from solid solution parent perovskites.

6.5 Discussion: Bulk and surface material response during metal exsolution

The structural relaxation of the host lattice, associated to the formation of metallic nanoparticles in the perovskite bulk, exhibits a temperature-activated behaviour and proceeds exceedingly fast with increasing temperature. In contrast, the influence of the reduction temperature on the dynamics of the exsolution of nickel dopants from the subsurface to the perovskite surface is negligible. Here, *in-situ* NAP-XPS analysis of the the surface chemical changes of STNNi during sample reduction, revealed a rapid exsolution response at a temperature as low as $T = 400°\text{C}$. The bulk response was found mostly inactive at such low temperatures, while nanoparticle exsolution is still apparent at the surface of the perovskite thin film. The evolution of a metallic feature in the $\text{Ni}2p_{3/2}$ core-level signal is detected to reach an equilibrium state after $\sim$10 h. Notably, synchrotron-based analysis with improved time-resolution suggests an even faster dynamics of the process.

No relevant influence of the reduction temperature on the exsolved nanoparticle volume was measured. This finding indicates, that a fixed, small fraction of reducible (nickel) dopants is transported to the surface, while most dopants will remain in the perovskite bulk. The STEM investigations discussed in chapter 4, have shown that the Ni dopants appear to be mobile within the bulk. Considering the findings presented above, however, the Ni dopants appear to be partially immobile after transition to the metallic state and to remain embedded in the oxide host lattice in form of metallic particles.

In accordance with the observation of a finite exsolution volume, nickel exsolution in STNNi is found to be widely limited to the near-surface region of the parent material. SIMS depth-profiling revealed no significant concentration gradient of Ni across the thin film thickness of (nanostructured) STNNi after reducing thermal treatment, independent from the annealing temperature. In comparison to the as-prepared parent material, only a slight accumulation of Ni at the surface was detected. Further insights about the exsolution width were gained by a systematic variation of the surface-area-to-volume ratio. and thus the Ni reservoir provided for the subsequent exsolution under reducing conditions. Here, nanoparticles of comparable dimensions were exsolved, independent of thin film thickness, while the particle density and the sum of the nanoparticle volume was found to increase with decreasing thickness. The exsolution width hence can be estimated to be equal or smaller than the minimal sample thickness applied in the experiment *i.e.* < 10 monolayers of STNNi.

The reduction temperature, however, has considerable influence on the nanoparticle properties. It severely affects the coalescence of nanoparticles *via* Ostwald ripening and therefore, the particle density and the particle dimensions. In particular at high temperatures, a considerable decrease of the particle density and the respective increase in the particle size can be observed. The processing temperature thus proves suitable to adjust the particle properties of the nanostructured product, however it has only negligible impact on the total amount of catalytically active nickel metal at the surface of the oxide support.

Since the evolution of surface nanoparticles and the relaxation of the bulk structure follow a different dynamics, both processes appear to be not, or only weakly interrelated. The formation of surface nanoparticles during metal exsolution is mainly determined by processes which take place in the near-surface region of STNNi, while the bulk changes of the material are mostly independent from the, technically relevant, self-assembly of nanoparticles at the crystal surface. The insights gained from this study imply that many strategies to tailor exsolution-active materials discussed in literature may be misleading and need to be reconsidered as they are solely developed on the basis of bulk properties, while the surface properties appear to be vital for the exsolution of metal nanoparticles to the surface of exsolution-active perovskites.

Accordingly, the STNNi surface properties will be subject of the further discussion. In the following chapter, a detailed investigation of the chemical and physical changes in the near-surface region will be investigated under oxidizing and reducing conditions and correlated to the exsolution response.

Chapter 7

The role of surface space charge regions for metal exsolution

At the surface of oxide materials, many properties fundamentally deviate from the bulk behavior. The origin lies in the formation of space charge regions (SCRs) with large electrostatic potentials as a consequence of the redistribution of mobile charge carrier at in the surface region (reduced local enthalpy of formation for oxygen vacancies). For instance, the presence of SCRs may result in an altered electronic and ionic conductivity, thermal conductivity or catalytic activity of functional oxides and is linked to changes in the elemental composition of oxide surfaces. Therefore, surface space charge constitutes an important feature of oxides and needs to be considered for any surface process that involves charge or mass transport. In this chapter, the interrelation between the space charge region induced at the surface of STNNi and nickel exsolution is discussed and the significance of space charge for the exsolution response is elaborated, with special focus on the kinetics of the exsolution process. For this purpose, *in-situ* spectroscopy is applied to probe the formation of SCRs, and their impact on the exsolution dynamics is correlated to the assembly of nanoparticles during redox exsolution. Additionally, oxygen exchange studies are carried out to investigate the influence of SCRs on the oxygen exchange kinetics of STNNi. An approach of surface engineering is demonstrated as an efficient strategy to tailor the exsolution response of perovskite materials by modification of the defect chemistry in the near-surface region of the perovskite. Derived from the analysis, an exsolution model is described, which takes the influence of space charge regions on the ionic mass transport into account. Please note that the data discussed in this chapter was partly published in reference [184].

7.1 Surface passivation of exsolution-active perovskites caused by a negatively charged space charge region

Probing space charge regions by *in-situ* spectroscopy

The nature of space charge is strongly entangled with the defect chemistry of oxide materials. To understand the characteristics of the SCR at the surface of STNNi, one needs to consider the specific structural properties of the material. As discussed in detail in chapter 4, the dissolution of Ni dopants in STNNi is incomplete. Consequently, the STNNi host lattice is predominantly doped by Nb donors while nickel is present in secondary nanostructures and accordingly, STNNi follows the defect chemistry of an *n*-type perovksite (*cf.* section 2.4). Therefore, the formation of a space charge region of negative surface potential is expected in oxidizing conditions, that diminishes with decreasing oxygen partial pressure.[107, 196]

In order to probe the formation of a surface space charge region and to follow the changes in the electrostatic surface potential during metal exsolution under reducing conditions and in comparison under oxidizing conditions, NAP-XPS is carried out.[1] For this purpose, the methodology described in section 6.2 is revisited. The Ni $2p_{3/2}$, Ti $2p$, Sr $3d$, O $1s$ and Nb $3d$ XPS core-level spectra are recorded *in-situ*, while the redox environment is controlled by the ambient atmosphere at an elevated sample temperature. Figure 7.1a shows the evolution of the Ni $2p_{3/2}$ signature over the measurement time during alternating reduction and oxidation steps.

Initially, the XPS core-level spectra are recorded at room temperature and under UHV conditions. After a short heat-up in oxygen in order to desorb carbon species from the sample surface, the exsolution of nickel is induced by reducing annealing. As discussed in section 6.2, the relative intensity of the peak at B.E. ~855.6 eV and the peak centered at about B.E. ~851.9 eV provides information about the formation of metallic nanoparticles at the perovskite surface. Here, the metal signal successively increases over reduction time, while the oxide signal decreases. After an equilibrium state is reached, and no further changes in the Ni signature were detected during reduction, the ambient gas atmosphere is switched from H_2 to O_2. As can be seen, a pronounced oxide signal is recovered while the metal signal vanishes. Likewise, switching back from oxygen environment to hydrogen environment results in the reestablishment of a pronounced metal signal in the Ni $2p_{3/2}$ core-level spectrum. Since nanoparticle exsolution in STNNi is not reversible by re-oxidation (*cf.* appendix D), the chemical changes observed most likely indicate a change in the nanoparticle chemistry. Here the nanoparticles remain pinned at the

---

[1] The NAP-XPS experiments were performed in collaboration with by B. Šmíd (Charles University, Department of Surface and Plasma Science, 18000 Prague, Czech Republic) whose support is highly appreciated.

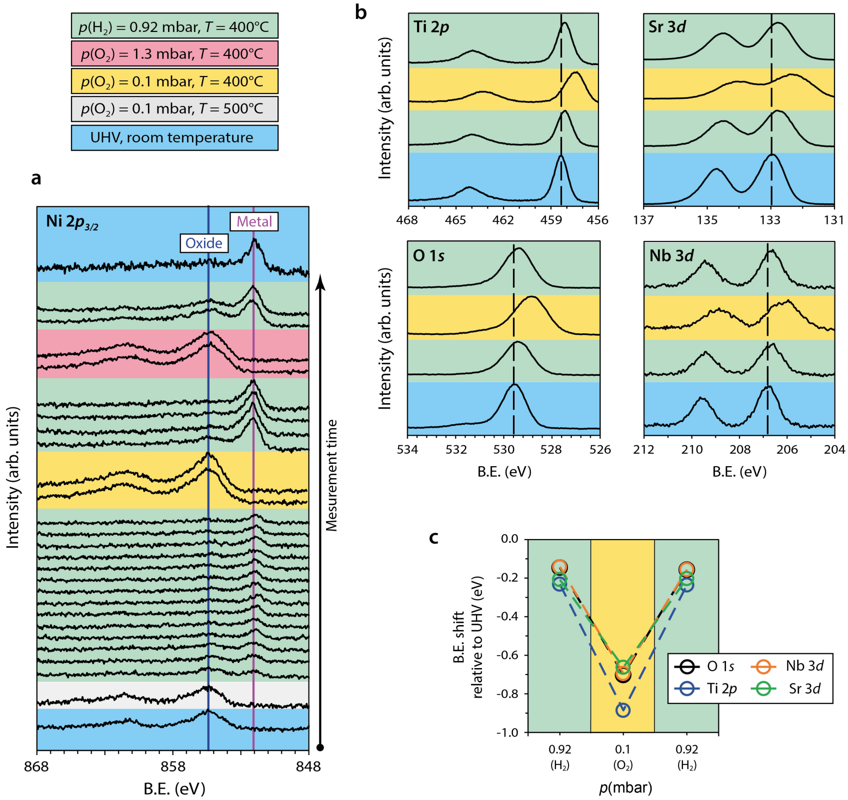

Figure 7.1: Investigation of surface chemistry and changes in the electrostatic surface potential of STNNi under oxidizing and reducing conditions related to a space charge region at the perovskite surface. (a) Investigation of the Ni$2p_{3/2}$ core-level spectrum by *in-situ* NAP-XPS during alternating oxidizing and reducing sample treatment at elevated temperatures. The binding energies of the plotted spectra were corrected to the Tip position and the intensity was normalized to the pre-peak region. Notably, the plot partly replicates data shown in Fig. 6.3c. (b) Investigations of Ti 2p, Sr 3d, O 1s and Nb 3d core-level spectra at oxidizing and reducing conditions by NAP-XPS. (c) A shift in the binding energy relative to UHV conditions gives evidence about the formation of a space charge region at the STNNi surface. For NAP-XPS investigations STNNi was deposited on conductive Nb:STO substrates. The thin film thickness is 20 nm. Modified from ref. [184].

perovskite surface while changing from metallic Ni to NiO and *vice versa*, according to the redox environment. The oxidation of the metallic particles may result in an increase of the particle size and in consequence in an increase in the intensity of the core-level spectrum.

Representative Ti 2*p*, Sr 3*d*, O 1*s* and Nb 3*d* XPS core-level spectra, obtained under UHV conditions (room temperature), reducing conditions and oxidizing conditions respectively, are shown in Fig. 7.1b. As can be seen, only minor changes are visible upon thermal oxidation and reduction. Most importantly, a shift in the spectra towards lower binding energies and of equal magnitude for all elements is visible, which was shown to be directly related to the presence of a space charge region at the perovskite surface.[111, 197, 198] To visualize the binding energy shift for oxidizing and reducing conditions, the magnitude of the B.E. shift relative to the UHV position (highlighted by a dashed line) is plotted in Fig. 7.1c. Note that the binding energy detected in ultra high vacuum does not provide information about the surface redox chemistry since the defect equilibria are not active at room temperature. The binding energy is rather influenced by the kinetically determined growth process and can hence only serve as a relative reference value. As can be seen, the magnitude of the B.E. shift depends on the respective redox conditions and is much more pronounced under oxidizing conditions, which indicates the formation of a large surface potential, while the potential is diminished in reducing conditions. Furthermore, it is reversible when switching between oxidizing and reducing conditions.

Besides a shift in the binding energies, Fig. 7.1b also indicates a general broadening of the spectra under oxygen atmosphere. The broadening of the spectra at ambient gas atmosphere may have different origins. In part, it directly results from the presence of a potential gradient at the surface[111, 114, 199] and hence the peak broadening is a consequence of the space charge region. Furthermore, extensive broadening of the Sr 3*d* spectrum under oxidizing conditions may indicate the formation of a minor SrO or $Sr(OH)_2$ surface phase in agreement with the formation of negatively charged Sr vacancies in the near-surface region.[111] Here, a considerably flattened intensity valley between the Sr $3d_{5/2}$ and the Sr $3d_{3/2}$ contribution may result from the evolution of a second doublet of slightly higher binding energy. And finally, scattering effects with the ambient oxygen and hydrogen gas may contribute to the peak broadening.

In order to investigate the influence of the oxidation-induced space charge region at the STNNi surface on the exsolution process, the exsolution response of Ni at the pristine STNNi surface (protocol 1, Fig. 7.2a) is compared to the exsolution response after an extensive pre-annealing of the STNNi thin film in oxygen (protocol 2, Fig. 7.2b) to promote the formation of a negatively charged surface SCR. It is worth to point out that the pristine thin films were quenched to room temperature after the thin film deposition to prevent overoxidation of the pristine sample

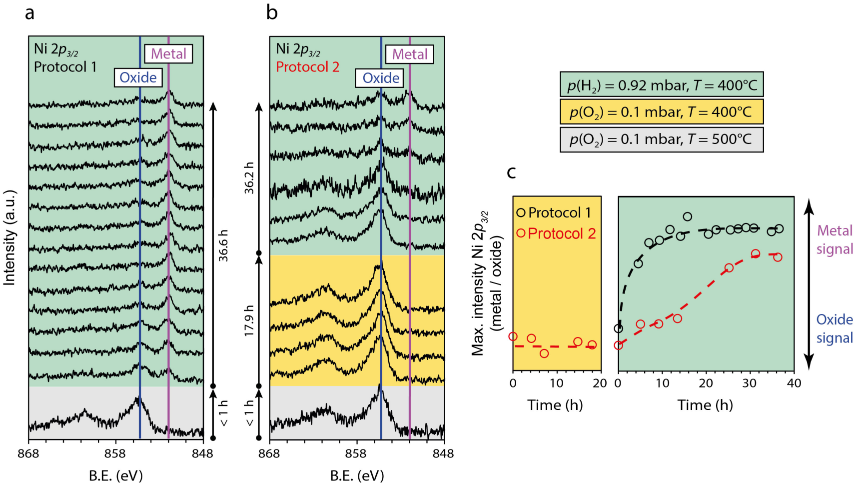

Figure 7.2: Influence of the oxidation-induced space charge region on the exsolution dynamics of Ni in STNNi. Investigation of the surface chemistry based on the Ni $2p_{3/2}$ core level spectrum during metal exsolution using *in-situ* spectroscopy. The exsolution response of a (a) pristine sample (protocol 1) and of a sample after an extensive pre-annealing procedure in oxygen (b) (protocol 2) is compared. The binding energies of the plotted spectra were corrected to the Tip position and the intensity was normalized to the pre-peak region. Note that the plot partly replicates data shown in Fig. 6.3c. (c) Evaluation of the exsolution dynamics during reducing treatment, based on the intensity ratio of the metal and oxide feature derived from (a, b). Black circles denote data points obtained on the basis of protocol 1 while red circles denote data points obtained on the basis of protocol 2. Dashed lines are given as guide for the eye. For NAP-XPS investigations STNNi was deposited on conductive Nb:STO substrates. The thin film thickness is 20 nm. Modified from ref. [184].

subsequent to the thin film growth. The evolution of the Ni $2p_{3/2}$ core level spectrum obtained from both samples over the measurement time is compared. While a rapid change in the metal / oxide ratio is detected for the pristine sample during protocol 1 (compare also section 6.2), the exsolution response is considerably delayed after the thermal treatment of STNNi in oxidizing conditions as visible during protocol 2. Here, the emergence of a metallic signal at about B.E. ∼851.9 eV remains absent after switching to hydrogen gas for several hours before a significant increase of the metallic Ni peak is visible. Compared to the rapid exsolution response at the pristine surface after ∼4.5 h during protocol 1, the formation of a metallic signature becomes first visible after ∼25 h of reduction during protocol 2 (Fig. 7.2c).

The NAP-XPS investigations revealed that the annealing history which is strongly entangled with the electrostatic potential at the perovskite surface considerably impacts the exsolution response. In order to correlate the passivation effect revealed

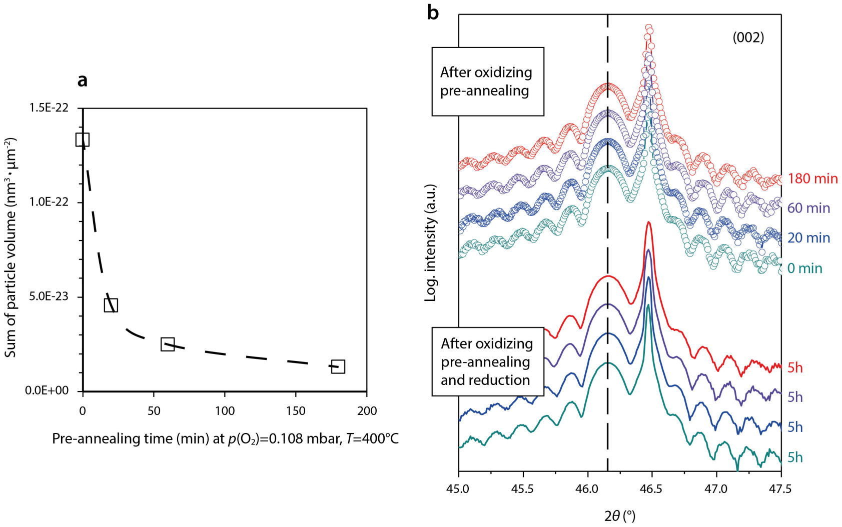

Figure 7.3: Oxidizing pre-annealing before the thermal reduction results in surface passivation. Pieces of STNNi that were cut from the same thin film sample and pre-annealed in oxidizing environment for 20 min, 60 min and 180 min respectively (T = 400°C, $p(O_2)$ = 0.108 mbar), before they were reduced (T = 400°C, 5 h, 4 % H_2 / Ar). (a) The passivation effect is directly correlated to a reduced nanoparticle volume exsolved to the perovskite surface. The nanoparticle volume was investigated by representative AFM scans with a scan size of 2 x 2 μm^2. (b) No detectable shift in the diffraction position of the (002) Bragg peaks is revealed by XRD analysis in 2θ-ω measurement geometry, either after oxidizing annealing (above), or after subsequent reducing annealing of the thin films (below). For the analysis STNNi was deposited on conductive Nb:STO substrates. The thin film thickness is 50 nm. Modified from ref. [184].

by *in-situ* spectroscopy to the morphological evolution of the perovskite surface during nanoparticle exsolution, complementary annealing studies are performed *ex-situ*. For this purpose, pieces of 5 x 5 mm^2 in size were cut from a 50 nm thick STNNi thin film and pre-annealed in the PLD chamber for different times of 20 min, 60 min and 180 min respectively, at a temperature of T = 400°C and at an oxygen partial pressure of $p(O_2)$ = 0.108 mbar. Notably, the conditions are well comparable to the annealing conditions applied during the NAP-XPS analysis. Subsequently, an as-prepared pristine sample and the pre-annealed samples were jointly reduced by thermal annealing (T = 400°C, 5 h, 4 % H_2 / Ar). As can be seen in Fig. 7.3a, the total nanoparticle volume is significantly decreased after the oxidizing treatment. Here, even a short oxidizing treatment of 20 min results in a strong suppression of the exsolution response during the comparably long reducing annealing. In accordance with the findings discussed above, XRD investigations of the thin films after oxidizing treatment and after reducing treatment did not reveal any detectable shift of the thin film diffraction peaks, indicating a surface process as the origin of the observed passivation effect (Fig. 7.3b).

The findings indicate a clear surface passivation effect of the oxidizing pretreatment, which results in a strong delay of the exsolution response of Ni in STNNi. Here, the presence of a surface space charge region may impact the exsolution process by electrostatic interactions of the charged dopants with the negatively charged surface potential.[30] Nickel dopants exhibit a negative charge relative to the B-site cations of the STNNi host lattice, *i.e.* Ti (IV) and Nb (V), where Ni cations occupying the B-site of the perovskite structure are expected to exhibit the nominal charge Ni (III). Moreover, a large amount of Ni-dopants is present in form of NiO_x nanostructures with $x \approx 1$ and hence are expected to have the nominal charge Ni (II). The negative space charge potential between the perovskite surface and the bulk results in a repulsive interaction with negatively charged species, such as mobile acceptors, and hence Ni-dopants in STO. Therefore, the negative SCR at the perovskite surface may act as a considerable energy barrier with blocking character for exsolving Ni dopants. The negative surface potential diminishes under reducing conditions[107, 196], where the accumulation of oxygen vacancies in the near-surface region is favorable, while the formation of Sr vacancies may be suppressed. At highly reducing conditions, even the inversion of the space charge region was reported.[109] Here, attractive electrostatic interactions of negatively charged dopants with the positive surface potential may even result in an accelerated exsolution response.

Finite-element electrostatic space charge simulations

In order to examine the nature of the surface potential, as a function of oxygen activity and temperature, finite-element electrostatic space charge simulations are performed.[2] A detailed description of reaction equations and input parameters used for the simulations are given in the appendix C. The calculations are based on the bulk defect concentrations for $SrTiO_3$ determined by band gap excitation, oxygen exchange as well as dopant concentration. Here, the space charge formation was calculated considering an active Schottky equilibrium at the surface that allows for the formation of strontium vacancies.[43, 108] Furthermore, a reduced enthalpy for the formation of oxygen vacancies in the topmost atomic layer[42, 89] is included in the calculations. As a consequence of the varied defect equilibria in the surface region, a redistribution of the surface defect concentrations is evident, which results in the establishment of a surface space charge region, obeying electrostatic boundary conditions. Electrostatic potential, electric field and local defect concentrations were solved self consistently using a finite-element routine, with the boundary condition of vanishing space charge in the bulk (global charge neutral-

---

[2] The calculations were performed by F. Gunkel (Forschungzentrum Jülich, Peter Grünberg Institut (PGI-7), 52425 Jülich, Germany) whose support is highly appreciated.

ity). The $a(O_2)$-dependence was derived from the intrinsic $a(O_2)$-dependence of the defect equilibria.

The species of lowest mobility, *i.e.* the diffusion of Sr vacancies in oxidizing conditions, kinetically limited to the topmost surface of the oxide, determines the formation kinetics of the space charge region.[108] At low temperature, such as T = 400°C a negative space charge region establishes in a wide range of oxygen activities, down to $a(O_2) \sim 10^{-40}$ (Fig. 7.4a). The inversion towards a positive SCR requires highly reducing conditions. Here, the negative surface potential becomes absent at an oxygen activity of $a(O_2) \sim 10^{-50}$ (comparable to the conditions in hydrogen during NAP-XPS), while the further decrease in the oxygen activity results in the formation of a positive surface potential. As can be seen, the SRC depth is similar, independent from the oxygen activity as it is mainly determined by Nb doping concentration. In accordance with the high doping level, a narrow space charge region is determined for the given conditions. Furthermore, the annealing temperature considerably influences the space charge potential. Fig. 7.4b shows that increasing temperatures favor the inversion of the space charge potential at higher oxygen activities. The blocking character due to oxidation remains, however.

7.2 Measurement of ^{18}O tracer profiles to investigate surface space charge regions by SIMS

As discussed in section 6.3, SIMS is a powerful technique to resolve the elemental distribution within a sample by recording a depth-resolved mass-spectrum starting from the sample surface followed by the successive sputtering into the bulk. Moreover, the excellent mass-resolution of the time-of-flight mass-spectrometer allows to resolve the isotopic ratios of ^{16}O / ^{18}O and hence can be applied for tracer exchange experiments to study the oxygen exchange kinetics of functional oxides.[115, 145, 200, 201] Epitaxial thin films of single-crystal character are ideal model systems for oxygen exchange experiments as they allow for the study of oxygen bulk diffusion without the influence of grain boundaries, which often exhibit different diffusion characteristics[202–204]. Moreover, the material of interest can be deposited with a low surface roughness in the sub-nanometer range, that is a prerequisite to resolve the elemental constitution of the near-surface region with high precision. This is of particular importance for probing the space charge region at the perovskite surface.

Surface SCRs can be indirectly probed by isotope exchange profiles on the basis of their impact on the oxygen exchange characteristics of oxide materials. As illustrated in the schematic sketch in Fig. 7.5, oxygen diffusion into the perovskite bulk requires the diffusion through an extended surface SCR. Depending on the nature of the SCR, it may strongly impact the oxygen exchange kinetics of oxide materials.

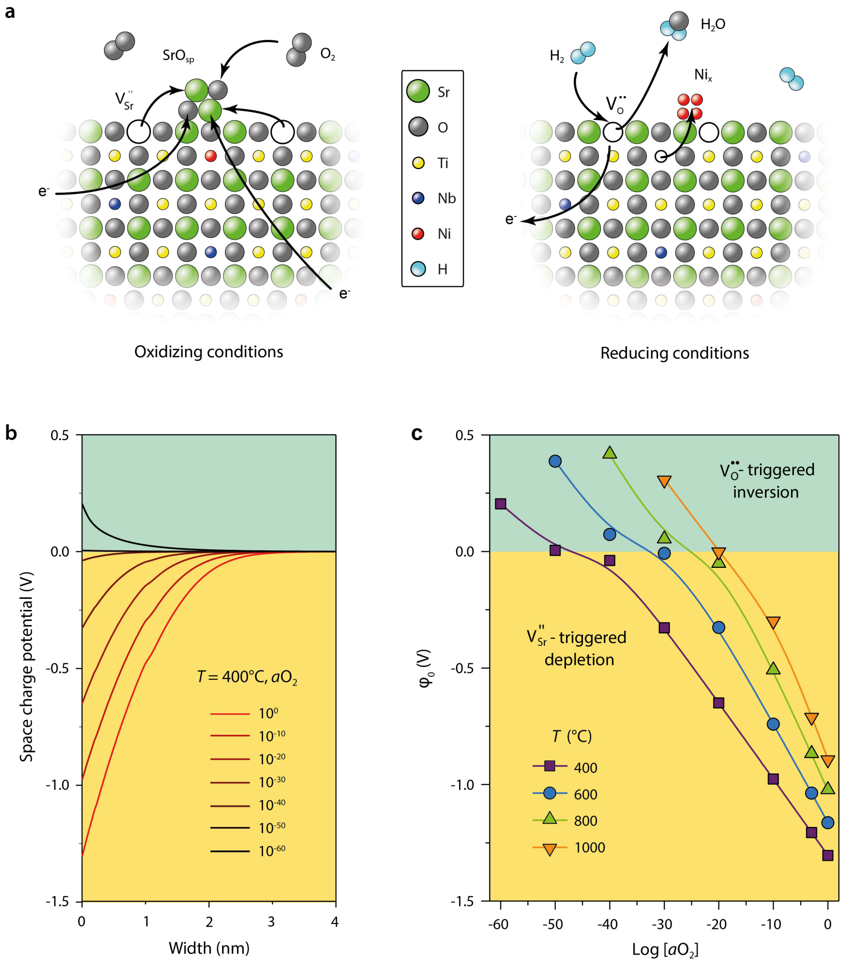

Figure 7.4: Finite-element electrostatic space charge simulations. (a) Simplified illustration of the redox chemistry of STNNi in oxidizing and reducing conditions. Under oxidizing conditions, negatively charged strontium vacancies form in the near-surface region resulting in a negative surface space charge potential. In contrast, strongly reducing conditions may result in the establishment of a positive surface potential due to the introduction of positively charged oxygen vacancies in the surface region. Notably, the change in the electrostatic surface potential is accompanied by the exsolution of acceptor-type dopants (such as Ni in STNNi). Kröger-Vink notation is used in the sketch.[105] (b) Space charge potentials at the surface of donor-doped strontium titanate at a temperature of T = 400°C. A negative surface potential is established in a wide range oxygen activities, while the inversion towards a positive space charge potential is visible at very low oxygen activities. The magnitude of the space charge potential increases with decreasing oxygen activity. The depth of the space charge region mainly depends on the Nb concentration and hence does not vary in the given range of oxygen activities. (c) Space charge potential as a function of oxygen activity and temperature. Increasing temperatures favor the inversion towards a positive surface potential at higher oxygen activities. Modified from ref. [184].

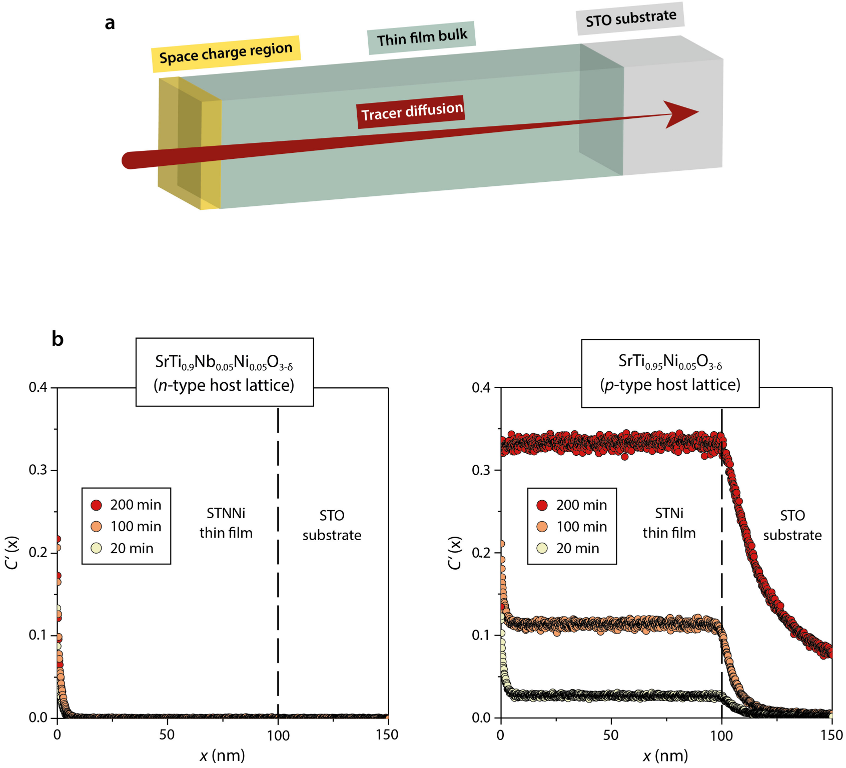

Figure 7.5: ^{18}O tracer profiles determined by SIMS analysis for STNNi (*n*-type) and STNi (*p*-type) after equilibrium in $^{16}O_2$ gas and exchange in $^{18}O_2$ gas for different annealing times of 20 min, 100 min and 200 min at T = 400°C and $p(O_2)$ = 200 mbar, respectively. Oxygen diffusion is much more sluggish in STNNi compared to STNi. The tracer profiles show no significant differences for varying exchange times for STNNi, while an increasing tracer fraction with increasing exchange time is detected for STNi. As depicted by the illustration, the tracer diffusion across the thin film is influenced by the formation of space charge regions at the surface as well as the oxygen vacancy concentration in the thin film bulk of the heavily donor- and acceptor-doped materials.

In order to compare the oxygen exchange characteristics of *n*-type STNNi, *p*-type STNi is used for direct comparison. After equilibration of the 100 nm thick samples in $^{16}O_2$ gas, oxygen exchange studies are performed in $^{18}O_2$ enriched oxygen gas (T = 400°C, p = 200 mbar) with different exchange times of 20 min, 100 min and 200 min. Here, an STNNi and STNi thin film are jointly exchanged in the same annealing process, respectively, to compare the oxygen exchange kinetics of predominantly donor-doped and acceptor-doped strontium titanate host lattice under equal conditions. After the isotopic labeling the isotopic profiles are determined by SIMS analysis. Based on this approach, a direct comparison of the oxygen exchange kinetics of the *n*-type and *p*-type perovskite materials is possible.[3]

The tracer fraction $C'(x, t)$ is calculated according to ref. [115] by equation 7.1

$$C'(x,t) = \left(\frac{C(x,t) - C_{\mathrm{bg}}}{C_{\mathrm{g}} - C_{\mathrm{bg}}} \right) \tag{7.1}$$

where $C(x,t)$ is the isotope fraction in the sample measured by SIMS, C_{bg} is the natural isotope background (0.2 %) and C_g is isotope enrichment in the $^{18}O_2$ gas used during sample annealing (83.45 %). The sputter depth is determined by using the Ni cation profile as an internal reference to normalize the sputter time to the thin film thickness determined by RHEED analysis. The time-dependent isotope profiles obtained from both materials are shown in Fig. 7.5.

As can be readily seen, the oxygen exchange kinetics are fundamentally different for the STNNi (left) and STNi (right) thin films. The oxygen exchange in STNNi is strongly limited to the surface region for the investigated temperature-time window. The high level of doping with Nb-donors effectively suppresses the presence of oxygen vacancies[108] in the perovskite lattice bulk, which considerably limits the oxygen mobility within the *n*-type oxide.[205] Consistently, no significant incorporation of ^{18}O isotopes is detected beyond the surface region. In the surface region, an increased tracer fraction is detected only within the first few nanometers of the material. The enrichment with ^{18}O is most pronounced for the topmost surface and successively decreases with increasing distance from the surface visible from the steep drop in the tracer profile. Here, the formation of negatively charged SCR, *i.e.* the establishment of an electron depletion layer results in the accumulation of oxygen vacancies in the near-surface region[108] (adjoining the topmost layer of negative charge).

---

[3] The SIMS experiments were supported by A. Aguadero, A. Cavallaro and S. Fearn (Imperial College London, Department of Materials, London SW7 2BP, United Kingdom) whose support is highly appreciated.

In contrast, acceptor doping promotes the introduction of oxygen vacancies in the perovskite bulk in order to maintain charge neutrality.[205] Therefore, the compensation of the charged Ni dopants results in large concentrations of oxygen vacancies that provide for considerable conductivity of oxygen ions within STNi. Notably, Ni is expected to be partially dissolved in the perovskite lattice. In particular for STNi (*vs.* STNNi) due to the missing influence of Nb dopants (*cf.* chapter 4). In accordance, the thin film bulk is found to be strongly enriched by ^{18}O isotopes, even after short exchange times, and increasing levels of ^{18}O tracers are detected with increasing annealing durations. Notably, the oxygen diffusivity is fast at the given temperature and results in a constant tracer fraction between the surface region and the thin film-to-substrate interface in the given temperature-time window. This region of the profile is determined by the equilibrium between oxygen diffusion into the SCR and passing through the SCR into the bulk. Hence, no shallow, exponential decrease is detected which would only become visible on larger diffusion distances for materials of high ionic conductivity at the given conditions, and which is typically visible for bulk diffusion of oxygen in STO (*cf.* reference [84]). Notably, such an exponentially decreasing tracer profile is visible for the diffusion of ^{18}O isotopes into the underlying STO substrate.

The evolution of the tracer profiles detected for STNi are heavily influenced by the positively charged space charge region at the surface. The space charge region is strongly depleted from oxygen vacancies within the electron accumulation layer, relative to the perovskite bulk of uniform oxygen vacancy concentration. Therefore, the perovskite exhibits a locally decreased oxygen diffusion coefficient D_{O^*} in the near-surface region (as well as a decreased surface exchange coefficient k^*), that changes across the width of the extended space charge region, as it is directly coupled to the surface potential.[84, 101, 185] The decreased oxygen mobility in the near-surface region strongly influences the oxygen diffusion into the bulk region as it limits the indiffusion of oxygen. Here, after passing the surface region, fast diffusion in the bulk results in a flat tracer profile.

All in all, the oxygen exchange properties of STNNi and STNi are influenced by the interplay of the oxygen mobility within the space charge region at the perovskite surface and the oxide bulk, widely determined by the (local) oxygen vacancy concentration. Among other parameters, the surface and bulk characteristics for oxygen exchange is strongly influenced by the defect chemistry of the oxides and hence the type of doping. While the oxygen exchange kinetics is fast in near-surface region relative to the bulk for STNNi, the oxygen exchange is slow in the near-surface region compared to the perovskite bulk for STNi.

7.3 Surface engineering of the redox chemistry to tailor the exsolution behavior

The studies presented thus far provide evidence that the exsolution response in STNNi is limited to the near-surface region of the material (*cf.* section 6.3), and that the surface properties of the material is strongly influenced by the formation of a SCR under thermal treatment. The formation of a surface SCR manifests in the presence of an electrostatic potential directly entangled with a modified distribution of mobile charge carriers, and influences the exsolution response in STNNi significantly.

Since the nature of the SCR depends on the redox chemistry of the topmost surface of the perovskite, the modification of the surface chemistry may prove as an efficient strategy to tailor the exsolution behavior. In order to systematically modify the surface chemistry of STNNi and compare the exsolution response, epitaxial samples were deposited in so-called stack geometry (Fig. 7.6a). Here, the exsolution-active STNNi thin film constitutes the bottom layer, while an additional layer of different doping (and hence different defect chemistry) is deposited on top. To demonstrate that the different materials can be deposited with a sharp interface, exemplary a thick STO top layer of 20 nm is deposited on a 20 nm thick STNNi bottom layer for XRD investigations. As can be seen in Fig. 7.6b, distinct KIESSIG oscillations are visible in the vicinity of the (002) diffraction peak, which exhibit a regular periodicity. This observation indicates that both the STNNi bottom layer and the STO top layer are coherently deposited with a sharp interface.[206, 207] In the as-prepared state, the Ni-containing and Ni-free materials hence can be synthesized in stack-geometry in form of two defined layers.

To compare the influence of a donor-doped and an acceptor-doped surface chemistry on the exsolution of Ni from the underlying STNNi layer, either $SrTi_{0.95}Nb_{0.05}O_{3-\delta}$ (STNb, *n*-type) or undoped STO is deposited as a top layer. Notably, nominally undoped STO exhibits a *p*-type defect chemistry, as it is typically naturally doped by acceptor-type impurities.[42, 43, 102, 108, 208] Here, only four monolayers of each material are deposited on top of an STNNi layer, respectively, to allow for mass transport through the top layer material of finite thickness.

After thermal reduction of the as-prepared stack samples (T = 600°C, 5 h, 4 % H_2 / Ar), the formation of exsolution nanoparticles is visible at the surface of the top layer materials, and the average nanoparticle volume is determined by AFM investigations (Fig. 7.6c). Thus, the mass transport of exsolving Ni across the solid-solid interface and through the originally Ni-free top layer material is evident. In a second experiment, the ionic sublattice is activated by thermal annealing under oxidizing conditions (T = 400°C, 60 min, $p(O_2)$ = 0.108 mbar) prior to the reducing

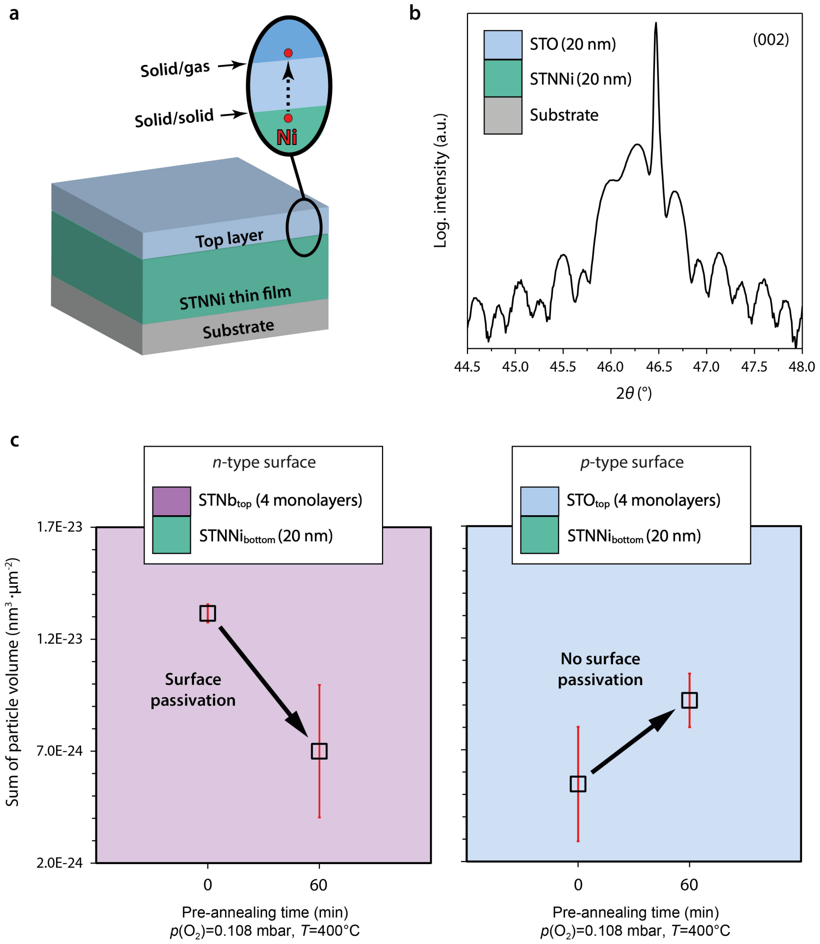

Figure 7.6: Modification of the surface redox chemistry to control the exsolution response in STNNi. (a) Schematic sketch of an epitaxially deposited sample in stack geometry. The surface chemistry is tailored by the deposition of a four monolayer thick top layer of different defect chemistry. (b) XRD investigations in 2θ-ω-geometry of a stack sample of 20 nm STO top- and 20 nm STNNi bottom layer. The modulation of the distinct KIESSIG fringes visible in the vicinity of the (002) diffraction peak indicates a sharp interface between the bottom and the top layer and gives evidence that the materials are deposited without significant intermixing. (c) For exsolution studies, four monolayers of either STNb or STO are deposited on top of pieces of STNNi which were cut from the same thin film sample. The sum of the average particle volume that has exsolved to the surface is determined after a 2-step thermal treatment ([1] oxidation ($T = 400$°C, 60 min, $p(O_2) = 0.108$ mbar); [2] reduction ($T = 600$°C, 5 h, 4 % H_2 / Ar)), based on the topological data obtained by AFM imaging. Averaged values obtained from three 2 x 2 μm^2 scans are plotted respectively; the error bars are based on standard deviations. Modified from ref. [184].

annealing step. As can be seen in (Fig. 7.6c (left), a decreased nanoparticle volume is detected for the stack sample with STNb top layer after an oxidizing pre-annealing step. The surface passivation effect related to the formation of a negatively charged SCR with blocking character at the surface of donor-doped STO, which exhibits a defect chemistry similar to STNNi, remains. In contrast, no passivation effect is detected for the stack sample with an STO top layer. In the given sample configuration, the absence of donors in the STO top layer may suppress the formation of Sr vacancies and hence the formation of a negative SCR.[209, 210] The study hence demonstrates that the exsolution behavior of perovskite parent materials can be effectively tailored by engineering of the surface chemistry.

In addition to electrostatic interactions, the different oxygen exchange properties of the top layer materials need to be taken into account. Most importantly, for *p*-type STNi oxidizing treatment results in a decreased oxygen mobility within the space charge region at the surface. During thermal reduction the space charge potential decreases and the oxygen exchange kinetics may increase. Still the passivation effect is solely visible for the *n*-type top layer, which indicates that electrostatic interactions play the major role for the surface passivation effect whereas the changes in oxygen exchange kinetics may be negligible. The role of oxygen exchange kinetics for exsolution-active perovskites remains to be elucidated and is subject of current investigations in collaboration with Imperial College London.

7.4 Discussion: Surface space charge regions govern the kinetics of metal exsolution

The study presented above was designed to investigate the role of space charge regions, that constitute an inherent feature of oxide surfaces, for metal exsolution. The presence of space charge regions at surfaces and interfaces has been shown to influence many fundamental properties of functional oxides.[30, 33–43, 211–214] The findings of the investigations indicate that surface space charge regions may also play a key role for the fundamental concept of metal exsolution and for the kinetics of metal exsolution processes in particular.

In-situ investigations by NAP-XPS revealed the reversible formation of a pronounced space charge region at the surface of STNNi under oxidizing conditions, while the surface potential diminishes during reducing treatment. STNNi follows the defect chemistry of a predominantly donor-doped material, since Ni dopants do not homogeneously dissolve in the perovskite lattice as discussed in detail in chapter 4. Notably, La donor-doped STO often applied as host lattices for exsolution dopants, show a similar redox behavior under oxidatizing conditions.[215] A blocking effect of the negative space region on exsolving Ni species is evident by comparison of the exsolution dynamics at the STNNi surface of a pristine sample

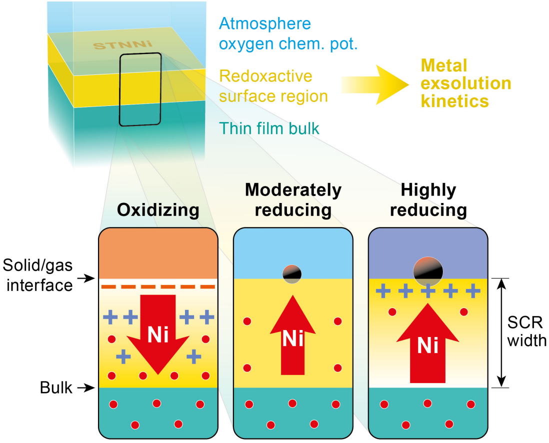

Figure 7.7: Simplified model of the exsolution process, which describes the influence of surface space charge regions on the metal exsolution kinetics at different oxygen chemical potentials. The illustration depicts three different cases, namely oxidizing, moderately reducing and highly reducing conditions. In oxidizing conditions, a negative space charge potential is induced at the surface of STNNi. The negative surface potential results in repulsive electrostatic interaction with Ni-dopants of relative negative charge.The space charge potential becomes more and more positive with decreasing oxygen activity *i.e.* under reducing conditions and allows for exsolution of Ni to the surface region. The surface acts as a sink of Ni dopants forming metallic nanoparticles. In consequence, a concentration gradient of Ni-dopants evolves which further promotes exsolution of dopants to the surface. At highly reducing conditions an inversion of the space charge region towards a positive surface potential may significantly promote the exsolution of dopants by attractive electrostatic interactions. The presence of surface-near SCRs widely dictates the exsolution kinetics. The electrostatic gradient of the SCR, critical for the release of dopants to the perovskite surface, is mainly determined by oxygen activity and temperature during thermal treatment. Modified from ref. [184].

with the exsolution response after extensive oxidizing treatment. The presence of the space charge region was further confirmed by ^{18}O exchange studies in combination with SIMS analysis, which were carried out on the *n*-type STNNi and, in comparison, on *p*-type STNi thin films. Besides the difference in the oxygen mobility within the perovskite bulk, a considerable influence on the oxygen exchange kinetics in the near-surface region results in the modulation of the tracer profiles due to local variations in the diffusion coefficient within the extended space charge region. Thus, the formation of space charge may influence the exsolution on two different levels. Most importantly, electrostatic interactions of charged dopants with the surface potential severely impact the metal exsolution kinetics. Secondly, changes in the local oxygen exchange kinetics within the extended space charge region may also influence the process.

Based on the results of the study an exsolution model is presented in Fig. 7.7.[4] The presence of a negative space charge potential, induced under oxidizing conditions, acts as blocking barrier for acceptor dopants with a negative charge relative to the host cations due to repulsive electrostatic interactions during the mass transport towards the surface and across the solid-gas interface (Fig. 7.7, left panel). Put simply: acceptor-type dopants are enclosed within the oxide by the negative surface charge. Notably, the synthesis of exsolution-active perovskites that accommodate reducible dopants is typically performed by a highly oxidizing treatment. The negative surface potential diminishes under reducing conditions and consequently, the energy barrier for metal exsolution to the surface is lowered. Nickel dopants that diffuse to the surface are reduced. The surface hence acts as a sink and in consequence a concentration gradient is established which further promotes the exsolution of Ni dopants (Fig. 7.7, central panel). Since changes in the surface potential are directly entangled with the slow diffusion of Sr vacancies, the decrease of the negative surface charge is sluggish and results in the delay of the metal exsolution response. Highly reducing conditions may result in an inversion of the space charge potential, *i.e.* in the formation of a space charge region with positive surface potential (Fig. 7.7, central panel). Here, the resulting attractive interaction may cause an accelerated exsolution response of acceptor dopants to the surface of the predominantly donor-doped host lattice.

All in all, the presence of space charge regions is pivotal for the metal exsolution behavior. The interaction of exsolving Ni dopants with the surface potential indicates that metal exsolution is based on ionic diffusion, rather than the motion of extended metal particles. In contrast, the metallic nanoparticles that are found to be embedded within the oxide bulk after reduction may exhibit a limited mobility. The motion of extended metallic nanoparticles towards the solid-gas interface would most probably not be affected by interactions with the surface potential since the metal carries no charge. The present findings indicate that the formation of metallic nanoparticles inside the bulk crystal does not necessarily imply mobility of these embedded particles.

Importantly, these results may also have significant implications for the exsolution response in multi-grain ceramics, where space charge regions typically establish at grain boundaries.

---

[4] The graphical design was supported by T. Pössinger (RWTH Aachen University, Institut für Werkstoffe der Elektrotechnik II (IWE2), 52074 Aachen, Germany) whose support is highly appreciated.

Chapter 8

Influence of the crystallographic orientation on the exsolution response at polycrystalline epitaxial surfaces

Thus far, solely thin films of (001) orientation were employed for the investigation of metal exsolution at the STNNi surface. The atomic surface composition strongly differs between the different crystallographic orientations of perovskite materials. Likewise, surface and interface processes, such as metal exsolution, that are influenced by the physical and chemical properties of functional oxides, may be orientation-dependent, as has been reported in literature.[19, 29] In this chapter, the influence of the crystallographic orientation for the exsolution response is briefly discussed. For this purpose epitaxial but polycrystalline thin films are employed as a hybrid material, that exhibits properties in between multi-grain oxide ceramics and epitaxial thin films of single-crystalline character. They hence reflect a first step from model system-like single crystalline epitaxial thin films closer toward functional ceramic exsolution materials. Markers are used to locate specific imaging areas to determine the crystallographic orientation of single facets of the thin film and to investigate the orientation-dependent nanoparticle exsolution behavior.

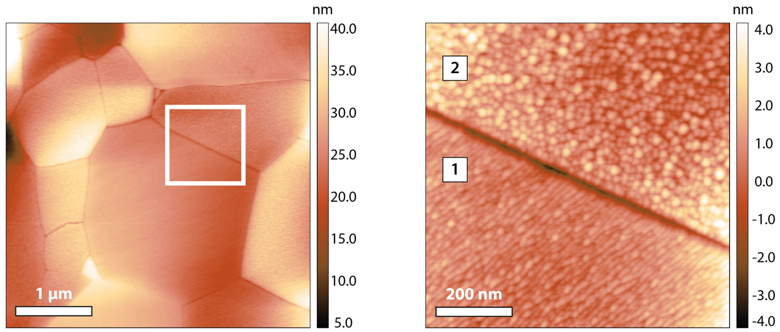

Figure 8.1: AFM surface imaging of polycrystalline STO substrates after high-temperature annealing. The scan size is 4 x 4 µm^2 (left) and 1 x 1 µm^2 (right). The image shown on the right depicts a detailed scan of the region highlighted by the white frame in the AFM image shown on the left.

8.1 Synthesis of polycrystalline epitaxial STNNi thin films

In order to synthesize epitaxial thin films in a well-defined manner, polished single crystals are typically applied as substrate materials. This is highly beneficial for the investigation of the fundamental properties of oxide materials and heterostructures, where it is preferred to exclude the influence of grain boundaries and different crystallographic orientations (among other parameters) to reduce the complexity of the material. In this spirit, [001]-oriented STNNi thin films were applied throughout this work, to study the exsolution of Ni at the (001) facet of the perovskite material. Technically relevant ceramics, however, are composed of multiple grains with randomly distributed crystallographic orientations, where the specific orientation of the crystallographic facets that are exposed to the ambient atmosphere may influence the exsolution response and consequently the overall nanoparticle yield.

A direct comparison of the material properties of epitaxial thin films and ceramics on an atomistic level is difficult, since the defect structure can be expected to differ due to the different synthesis conditions. Therefore, epitaxial thin films are deposited on polished polycrystalline substrates to investigate the role of the crystallographic orientation (and grain boundaries) on the exsolution of Ni in epitaxial STNNi. These kind of samples may be considered a hybrid material between epitaxial thin films and sintered ceramics. The defect structure is determined by the PLD growth and hence remains comparable to the results obtained from thin film samples discussed in this work, while grain boundaries separate STNNi facets of different orientations adapted from the underlying facets of the substrate to mimic the multi-grain structure of ceramic materials.

Polycrystalline STO substrates are prepared as discussed in section 4.1. Furthermore, each of the substrates, used for epitaxial growth of STNNi, was indented using a hardness testing machine in order to mark a region at the sample surface for the convenient localization of the probing area as demonstrated in ref. [216].[1] The as-prepared samples exhibit a well-defined surface morphology, with several grains visible (Fig. 8.1, left). Detailed imaging of two adjacent STO grains reveals slight differences in the surface morphology. While one of the grains (grain 1) exhibits a step-like surface morphology, the other (grain 2) exhibits a more columnar surface morphology. This observation illustrates that the surface properties may vary for different STO grains, which may be related to the orientation-dependent surface properties.

Epitaxial 50 nm thick STNNi thin films were deposited on the polycrystalline substrate. To study the orientation-dependent surface morphology, electron backscatter diffraction (EBSD) is carried out.[2] Fig. 8.2a shows the orientation map in Z_0-orientation (sample normal direction), obtained from the as-prepared STNNi thin film sample. Epitaxial growth of STNNi results in the adaption of the crystallographic orientation of the underlying STO grains. After relocalization of the EBSD probing area, AFM investigations of the sample morphology were performed (Fig, 8.2). Here, the characteristic grain boundary pattern of the surface serves as a fingerprint to identify the surface morphology of various STNNi facets of different crystallographic orientation. Similar to the STO substrate, slight differences in the morphology of several grains can be observed. In general, facets of two different kinds can be distinguished, which exhibit either a smooth and uniform appearance or facets of columnar and more irregular appearance. In combination with the EBSD mapping, it is evident that the facets of smooth surface morphology are related to the grains of (001) orientation. The surface morphology is furthermore investigated by scanning electron microscopy, comparing the surface of three adjacent facets of (001), (101) and (111) orientation. Consistent with AFM imaging, the (001) facet exhibits a smooth and uniform surface, while the (101) and (111) facets exhibit an increased surface roughness relative to the (001) surfaces.

The surface roughening is most likely related to the polarity of the (101) and (111) crystal facets.[217] Here, the surface polarity results form the dipole moment perpendicular to the surface and associated with the stacking sequence of atomic planes. Consistently, the STO (101) surfaces with a stacking sequence of $(\mathrm{SrTiO})^{4+} - (\mathrm{O}_2)^{4-}$ as well as STO (111) surfaces with a stacking sequence of $(\mathrm{SrO}_3)^{4-} - (\mathrm{Ti})^{4+}$ is polar, while the STO (001) surface with a stacking sequence of $(\mathrm{SrO}) - (\mathrm{TiO}_2)$ may be considered non-polar. As a consequence of polarity,

---

[1] Experimental support by M. Kindelmann (Forschungzentrum Jülich, Institute of Energy and Climate Research (IEK-1), 52425 Jülich, Germany) is highly appreciated.

[2] The EBSD analysis was performed by E. Wessel (Forschungzentrum Jülich, Institute of Energy and Climate Research (IEK-2), 52425 Jülich, Germany) whose support is highly appreciated.

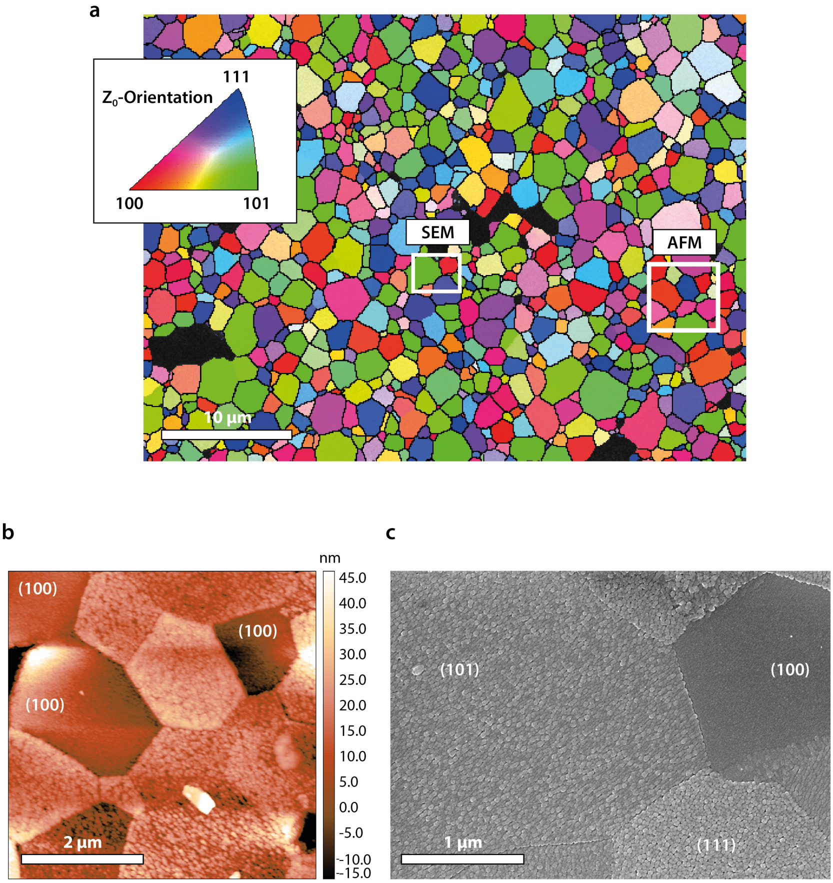

Figure 8.2: Surface analysis of 50 nm thick STNNi deposited on a polycrystalline STO substrate. (a) Electron backscatter diffraction orientation mapping. The color scheme depicts the orientation of the STNNi thin film facets adapted from the underlying STO grains in Z_0 orientation (sample normal direction). (b) AFM imaging in the EBSD probing region (highlighted in (a)). The scan size is $5 \times 5\ \mu m^2$. Grains of (001) orientation in Z_0-direction are highlighted. (c) SEM imaging in the EBSD probing region (highlighted in (a)). For comparison, three adjacent grains of (001), (101) and (111) surface orientation are shown. STNNi facets in (001) orientation exhibit a smooth surface morphology, while (101) and (111) exhibit a surface morphology with a columnar structure.

the surface energy becomes infinite which causes inherent instability of polar surfaces.[217, 218] Therefore, the charge at the (101) and (111) surface needs to be compensated either electronically or by changes in the chemical and structural composition of the surface.[219–221] The observation of orientation-dependent differences in the surface morphology hence may be related to chemical and structural reconstructions, which may influence the exsolution behaviour of Ni in STNNi. It is worth to point out that the differences in morphology that may be related to polarity-driven reconstructions were observed not only for the thin film material but also for the STO substrate, which was fabricated by sintering at high temperatures in air. This observation emphasizes that the surface reconstruction is not only a feature of thin film samples but needs to be also considered for technically relevant ceramic materials.

8.2 Evaluation of the facet-dependent exsolution behavior

To investigate the influence of the crystallographic orientation and the potential reconstruction of polar surfaces on metal exsolution, SEM-EBSD analysis was performed after thermal reduction (T = 600°C, 5 h, 4% H_2 / Ar). A representative SEM image of the polycrystalline thin film surface is shown in Fig. 8.3a. For comparison, the surface orientation of several grains are given in the figure that were determined by EBSD analysis. As can be seen, the exsolution of nanoparticles is visible at the (001) surfaces, which exhibited a smooth morphology in the pristine state. In contrast, the formation of significant nanoparticle populations can not be observed on top of the columnar (reconstructed) surfaces of the adjacent crystal facets. For comparison enlarged images of the as-prepared and the reduced (001), (101) and (111) surface extracted from Fig. 8.2c and Fig. 8.3a (left), are shown on the right. Here, several nanoparticles formed at the (001) surface are highlighted by yellow arrows. To verify the findings by topological analysis, AFM imaging is performed after thermal reduction of another piece of the sample (T = 600°C, 30 min, 4% H_2 / Ar). Consistent with the SEM investigations, an increased nanoparticle density is detected for the STNNi (001) surface, while only occasional nanoparticle growth is detected for the surrounding grains of different orientation (Fig. 8.3b). Representative scans of the nanoparticle populations at the (001) surface and an adjacent facet are shown on the right, which were obtained from the regions highlighted by white frames. Finally, an additional reduction treatment at an increased temperature (T = 800°C, 4 h, 4% H_2 / Ar) was performed using the same sample shown in Fig. 8.3b. Evidently, the nanoparticle density appears much more homogeneously distributed after treatment at an elevated temperature of T = 800°C. Notably, no preferential nucleation of exsolution nanoparticles at grain boundaries was detected for the thin film samples.

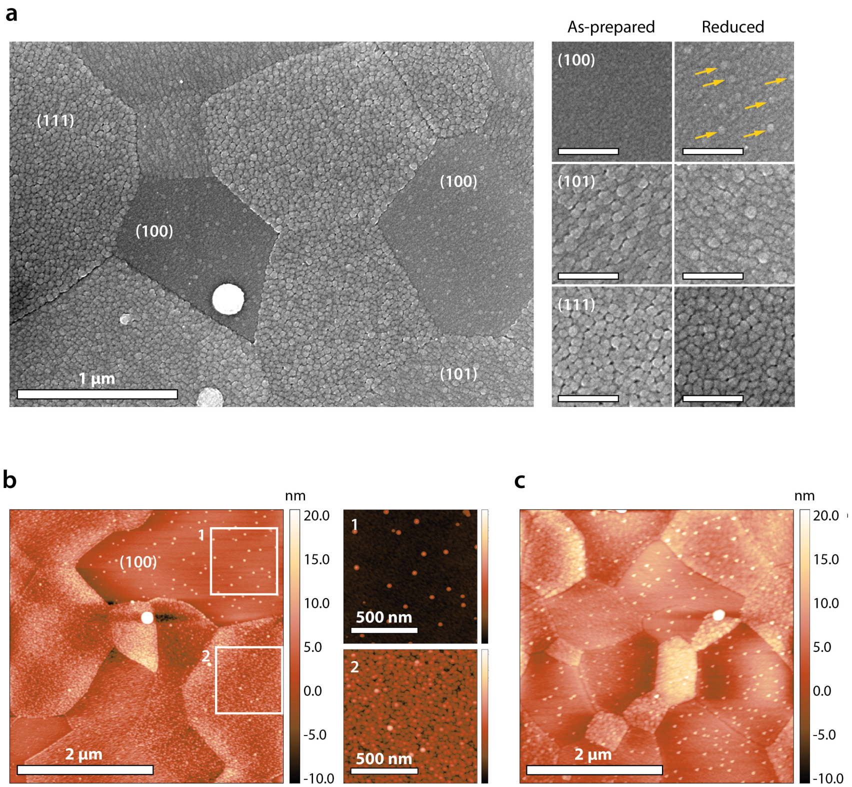

Figure 8.3: Investigation of the orientation-dependent exsolution response after thermal reduction at different conditions by surface imaging. (a) SEM imaging of the polycrystalline STNNi thin film surface after thermal reduction (T = 600°C, 5 h, 4% H_2 / Ar). The surface orientation of several grains are highlighted for comparison (determined by EBSD). The formation of exsolution nanoparticles is only detectable for (001) STNNi facets. A direct comparison of representative images of the orientation-dependent morphology in the as-prepared and the reduced state is shown on the right (scale bars denote 200 nm). Several exsolution nanoparticles at the (001) surface are highlighted by yellow arrows. (b) AFM imaging after thermal reduction (T = 600°C, 30 min, 4% H_2 / Ar). The scan size is 4 x 4 μm^2. Grains of (001) orientation, that initially show a smooth surface show a strong exsolution response, while only occasional nanoparticle growth is observed at the facets of other orientations. A detailed scan, comparing the nanoparticle density at the (001) surface to the surface of different orientation is shown on the right. (c) AFM imaging of the same sample shown in (b) after an additional thermal reduction treatment at higher temperature up to (T = 800°C, 4 h, 4% H_2 / Ar). The scan size is 4 x 4 μm^2.

The analysis has shown, that an early exsolution response is visible at the STNNi (001) facets. Therefore (001) surfaces may serve as preferential nucleation sites during redox exsolution in STNNi. In contrast, the exsolution of considerable nanoparticle populations at surfaces of different orientation required a thermal treatment at an increased temperature. Most likely, reconstructions of polar (101) and (111) surfaces result in the formation of surface layers with different chemical and structural properties relative to the perovskite structure that may act as a barrier for the mass transport of Ni during metal exsolution.

8.3 Discussion: Preferential exsolution of Ni at (001)-facets of STNNi

The orientation-dependent exsolution response was studied by employing polycrystalline epitaxial STNNi thin films. Here, markers were used to locate the imaging area to correlate the surface morphology of single STNNi facets to the respective surface orientation. Smooth perovskite surfaces are observed only for the [001]-oriented STNNi facets, while surfaces of different orientation exhibit a columnar top layer.

Based on the observation of distinct surface modifications for the polar (101) and (111) surfaces, one may hypothesize that polarity-driven surface reconstructions result in the formation of surface layers of different stoichiometry. The presence of such surface phases is directly related to a weak exsolution response in STNNi, which manifests a considerably decreased nanoparticle density at the surface, especially after reduction at a comparably low temperature while a higher temperature results in a more uniform nanoparticle distribution across all surface orientations (T = 600°C *vs.* T = 800°C). In contrast, a strong exsolution response is observed for (001) surfaces, where a considerable nanoparticle population exsolved even after short reduction times. Therefore, surface reconstructions need to be considered as a barrier for the exsolution of reducible dopants to the surface during thermal treatment.

The findings of the present study confirms the observation that metal exsolution is influenced by local deviations of native oxide surfaces from the nominal stoichiometry.[19, 32] In contrast to the findings present above, however, the authors report an increased nanoparticle yield at (101) surfaces of increased roughness, while the exsolution response appeared to be suppressed at the smooth (001) and (111) surfaces.[32] Other research indicated that the metal exsolution of nanoparticles at surfaces of different orientations may only deviate with respect to the nanoparticle properties (size, embedment etc.), while all of the (001), (101) and (111) facets exhibit a considerable exsolution response.[29]

The apparent discrepancy between the studies carried out on different material systems and by application of different processing conditions highlights the need for an in-depth analysis of orientation-dependent surface reconstructions, diffusion pathways and defect structures to develop a solid understanding of the mechanisms for the suppression of nanoparticle exsolution at surfaces of particular orientation. In view of the findings presented in chapter 7, it is impritant to note that the surface orientation may influence the space charge potential at the surface.[222]

A detailed study of the temperature-dependency of metal exsolution at surfaces of different surface orientations is ongoing work.

Chapter 9

Summary and Conclusions

The goal of this thesis was the investigation of the mechanistic processes that govern the exsolution behavior of Ni in $\mathrm{SrTi_{0.9}Nb_{0.05}Ni_{0.05}O_{3-\delta}}$ (STNNi) under reducing conditions. Special focus lay on the self-assembly of metallic nanoparticles at the perovskite surface as a promising concept for the synthesis of nanostructured catalysts.

Oxide ceramics of doped strontium titanate were synthesized and carefully analyzed with respect to the crystallographic phase and dopant distribution, while the doping composition and the doping-level was systematically varied. Furthermore, the high affinity of the material for the exsolution of Ni nanoparticles was demonstrated. For detailed analyses, epitaxial model systems of well-defined structural, chemical and surface properties were developed to assess the bulk and surface material changes associated with the exsolution of Ni dopants. Here, epitaxial thin films were employed to reduce the complexity that typically arises from the microstructure of technically relevant ceramics. Thin films with single-crystalline character, fabricated with a single-orientation, defined surface termination and with sub-nanometer surface roughness were achieved that enable the detection of nanoparticle growth in the very initial phase of metal exsolution. Based on the thin film model systems the surface and bulk dynamics of structural relaxations associated with oxygen diffusion and surface chemical changes related to the mass transport of dopants during the nanoparticle assembly were disentangled by *in-situ* spectroscopy and *in-situ* diffraction as well as oxygen exchange studies.

Investigations of the atomic structure of the exsolution-active STNNi thin films revealed inhomogeneities in the distribution of the reducible Ni dopants. A large fraction of nickel dopants was found to be enriched in NiO_x nanostructures that are embedded within the surrounding perovskite host lattice and aligned in between the thin film-to-substrate interface and the thin film surface. Exsolution in STNNi hence might not take place from dissolved single ion dopants but starts from extended dopant-rich structures. Consistent with this observation, investigations of ceramic STNNi pellets confirmed a certain degree of lateral inhomogeneity of the doping concentration, while the presence of embedded nanostructures was not detected. The structural relationship between the host lattice and the embedded phase within the thin film material was clarified, where a domain-matching mechanism that is based on the formation of a semi-coherent interface between both phases has emerged from the analysis. Here, the domain matching relationship directly influences the lattice parameter of the host phase actively changing upon metal exsolution.

Considering the foregoing results, the effect of non-stoichiometry on the exsolution behavior of embedded nanostructures was investigated. In comparison to solid solution parent materials, the application of non-stoichiometric parent perovskites is unsuitable to increase the nanoparticle yield at the perovskite surface. Here, lattice distortions correlated to the non-stoichiometry of the perovskite host lattice result in a weakened exsolution response, where defect interactions result in a decreased exsolution response.

In-depth analysis of the exsolution dynamics unveiled that the metal exsolution phenomenon, more precisely the mass transport and hence the fraction of dopants that contribute to the assembly of metallic nanoparticles, is strongly limited to the near-surface region. Accordingly, the exsolution process is mostly governed by the chemical and physical properties of the perovskite surface, that furthermore strongly depend on the ambient redox conditions at the solid-gas interface.

Systematic evaluation of the exsolved nanoparticle volume revealed that a fixed amount of Ni is exsolved to the surface independent from the reduction temperature. Differences in the nanoparticle density and in the nanoparticle dimensions are determined by subsequent coalescence which is promoted by high-temperature treatment. Consistently, no detectable depletion of the Ni concentration across the thin film thickness was observed while a slight enrichment of Ni at the surface was detected. In accordance with the findings, the systematic decrease of the surface-to-volume ratio did not result in an increased exsolution volume. Based on the analysis, a maximum exsolution width of < 10 monolayers can be determined for STNNi.

With respect to the observed surface limitations, it can be argued that the bulk and the surface contributions to the overall exsolution response are mostly independent processes, which is further emphasized by the different dynamics of the surface and bulk material changes during thermal reduction. The bulk reaction was shown to follow the kinetics of a temperature-activated reaction, that is widely based on the phase transition of Ni-rich nanoinclusions to the metallic state. The metallic transition at the surface during nanoparticle assembly however, proceeds on much shorter time scales and is active at much lower temperatures. Remarkably, the formation of nanoparticles was detected at low temperatures, where the bulk reaction *i.e.* the relaxation of the host lattice was observed to be fully inactive. The limitation of the exsolved Ni to a small sub-surface reservoir may contribute to the exceptional dimensional stability of exsolved nanoparticles, which have been shown to withstand long exposure to elevated temperatures without significant particle growth.

The most striking finding that has emerged from this study is that the kinetics of the exsolution response at the surface is strongly influenced by the presence of space charge regions at the surface. The formation of space charge regions is entangled with an altered formation energy for defects at the surface of doped oxides, and can be controlled by thermal annealing of the perovskite thin films that results in the redistribution of mobile charge carriers in the near-surface region.

Electrostatic interactions between the surface charge with the charged dopants that diffuse towards the solid-gas interface were identified to govern the exsolution kinetics (Fig. 9.1). Electrostatic repulsion between the negative surface potential, that is established at the surface of the predominantly donor-doped STNNi host lattice in oxidizing conditions, and the Ni dopants of relative negative charge results in a considerable delay of nanoparticle assembly at the perovskite surface. In comparison, nanoparticle exsolution is fast at the pristine surface, without oxidizing pre-annealing, where the magnitude of the negative surface charge is negligible.

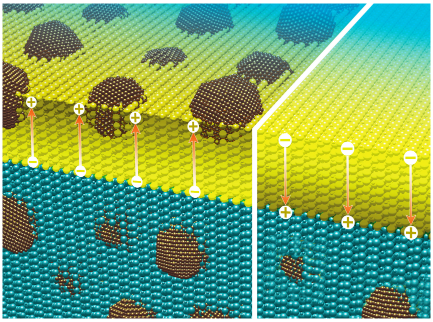

Figure 9.1: Schematic illustration of the interaction of exsolving species with surface space charge regions. A positive surface potential allows the passage of acceptor-type dopants. A negative surface potential results in severe passivation of the surface due to its blocking character for the diffusive movement of acceptor-type dopants. The graphical design was supported by T. Pössinger. Modified from ref. [184].

Derived from our combined experimental and theoretical investigations, we propose a mechanistic model that describes how metal exsolution is mediated by electrostatic surface potentials. While the dopants are enclosed within the perovskite bulk by a negative surface potential (restricting their release to the surface), thermal reduction results in a diminished surface potential. Therefore the energy barrier that results from the blocking surface potential decreases and the diffusion of Ni across the solid-gas interface becomes possible. The transition of charged Ni species to the metallic state at the surface results in a gradient of the chemical potential of Ni ions which drives the diffusion of Ni from the near-surface region. At highly reducing conditions an inversion of the surface potential results in a sign change, where the positive potential might accelerate the exsolution of acceptor dopants by attractive interaction with the surface region. As a consequence of the electrostatic interactions, the exsolution kinetics may be often dominated by the diffusion kinetics of the A-site sublattice in the near-surface region, since the formation of the space charge region is governed by A-site vacancies.

In line with the findings, engineering of the defect chemistry of the topmost atomic layers was demonstrated as a novel strategy for the active control of the exsolution behavior. Here, modifications of the space charge layer *via* doping is an effective stride to manipulate the self-assembly of exsolution nanoparticles.

With respect to the surface-dominated exsolution response, epitaxially deposited polycrystalline thin films have been synthesized to connect towards more realistic multi-grain materials in order study the exsolution response in dependence of the crystallographic orientation. Here, reconstructions of the polar (101) and (111) surfaces of STNNi were shown to hamper the exsolution dynamics of Ni to the surface. Accordingly, non-polar (001) surfaces of STNNi were found to serve as preferential exsolution sites for the facile assembly of metallic nanoparticles. The texture of exsolution-active perovskite parent materials hence needs to be considered for the evaluation of the exsolution behavior.

All in all, the findings of this thesis provide novel insights on the fundamental concepts of metal exsolution processes. While bulk properties of exsolution-active perovskite oxides are often addressed for the control of the exsolution behavior, the findings of this work highlight the major role of surface properties for metal exsolution processes. The dynamics of metal exsolution are intrinsically linked to the energy landscape of complex oxide surfaces, since the mass transport of dopants that contribute to the self-assembly of metallic nanoparticles is limited to the near-surface region. Therefore, greater attention needs to be paid to the surface properties of exsolution-active perovskites to realize the full potential of this synthesis route for the rational design of exsolution-type catalysts and to gain full control over the nanoparticle growth.

Appendix A

Structural analysis of epitaxial STNNi thin films by SAED

The diffraction vector Δg of the modulated signals can be determined from the diffraction as depicted in Fig. A.1. Several values were measured and an average value was determined. Δg depends on the diffraction vectors of the perovksite host lattice and the embedded phase.[131]

$$\Delta g = |g_{\mathrm{host}} - g_{\mathrm{embedded}}| \tag{A.1}$$

Using the lattice parameter of the perovskite host lattice determined by XRD (c = 0.393 nm) as a reference, the diffraction vector of the embedded phase can be determined. Here, equation A.1 has two solutions and in consequence two possible lattice spacings are determined. The most plausible material structure is therefore determined by comparison with literature values taking into account all chemical and structural information collected for the sample.

The out-of-plane and in-plane diffraction vectors for the embedded Ni-rich phase in the as-prepared state and after thermal reduction, as well as the possible lattice parameters are given in table A.1.

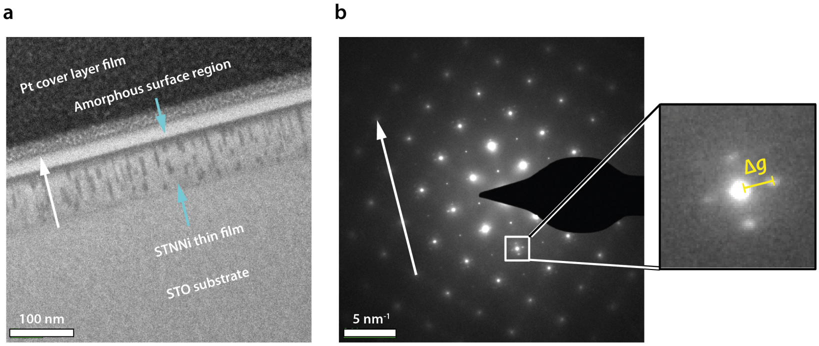

Figure A.1: Structural analysis of an 100 nm thick epitaxial STNNi thin film sample in the reduced state (T = 800°C, 15 h, 4 % H_2 / Ar) by selected area electron diffraction analysis. (a) Overview image of the FIB lamella obtained by TEM. (b) Electron diffraction pattern obtained from the thin film in the region of an embedded nanostructure. The electron diffraction pattern exhibits intensity modulations as a results of double diffraction. The respective satellite spots are visible around each of the main diffraction spots. A close-up of a representative diffraction spot is given on the right.

Table A.1: Structural analysis of epitaxial STNNi thin films by SAED. Out-of-plane (oop) and in-plane (ip) diffraction vectors g and lattice parameters d of the embedded phase (VAN) are given for the as-prepared and reduced sample state. The diffraction vectors were determined based on the satellite spots and main diffraction spots of the SAED pattern.

Sample state	$\Delta\, g_{oop}$ (nm^{-1})	$\Delta\, g_{ip}$ (nm^{-1})	d_{oop} (Å)	d_{ip} (Å)
As-prepared	0.26	0.30	3.515	3.565
			4.454	4.376
Reduced	0.53375	0.53375	3.248	3.248
			4.972	4.972

Appendix B

Evolution of the $SrTiO_3$ surface morphology under reducing annealing

In order to provide a reference for the morphological evolution of exsolution-active STNNi surfaces (discussed in the main text), a 40 nm thick epitaxial STO thin film was deposited (undoped). As can be seen in Fig. B.1 (above), the as-prepared surface exhibits a well-defined step terrace structure with smooth terrace steps. Fig. B.1 (below) shows that the surface morphology is slightly altered after thermal reduction (T = 700°C, 30 h, 4 % H_2 / Ar). Here, the formation of nanometric pits of arbitrary shape can be observed, which appear to preferentially form along the step ledges. The morphological evolution of the STO surface may be related to stoichiometric changes that are induced by the reducing treatment.[148, 223] Notably, similar pits were found to form at the surface of La-doped STO under thermal annealing.[224] Most importantly, it can be seen that the reducing treatment does not result in the formation of islands (for instance due to segregation). Therefore, it can be expected that the influence of secondary processes, which may lead to an altered surface morphology and are related to host cations, is negligible for the evaluation of Ni nanoparticles at the exsolution-active STNNi surface.

STO thin film (40 nm) on STO substrate: as-prepared

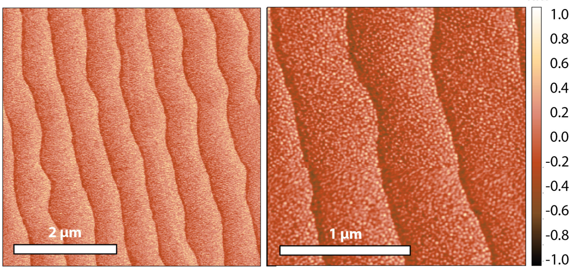

STO thin film (40 nm) on STO substrate: reduced (30 h, 700°C, 4% H_2 / Ar)

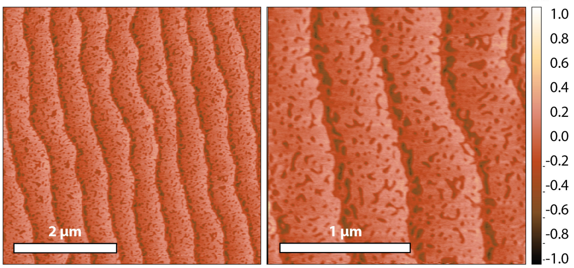

Figure B.1: AFM imaging of 40 nm thick epitaxial $SrTiO_{3-\delta}$ thin film deposited on STO. The surface morphology of the as-prepared state is compared to the reduced state (T = 700°C, 30 h, 4 % H_2 / Ar). The scan size is 5 x 5 μm^2 with scale bars of 2 μm and 2 x 2 μm^2 with scale bars of 1 μm respectively.

Appendix C

Finite-element electrostatic space charge simulations

The details on the finite-element electrostatic space charge simulations that were carried out to describe the $a(O_2)$-dependency and temperature-dependency of the space charge potential are given below. The calculations were performed by F. Gunkel (Forschungzentrum Jülich, Peter Grünberg Institut (PGI-7), 52425 Jülich, Germany).

Starting point for the space charge simulations is the bulk defect chemistry model of $SrTiO_3$ yielding the concentrations of electrons, electron holes and oxygen vacancies in the bulk as a function of temperature, ambient oxygen partial pressure (oxygen activity, $a(O_2)$) and dopant concentration.

For this, we use the intrinsic generation of electron-hole pairs via band gap excitation

$$e + h \rightleftarrows nil \tag{C.1}$$

and the corresponding law of mass action

$$np = K_{\mathrm{i}}^{0} \cdot \exp\left(-\frac{\Delta E_{\mathrm{g}}}{k_{\mathrm{B}}T}\right) \tag{C.2}$$

Here, n (p) denote electron (hole) concentration, K_{i}^{0} the reaction constant prefactor for the intrinsic electron-hole pair equilibrium, and $\Delta\, E_\mathrm{g}$ the band gap of $\mathrm{SrTiO_3}$. We moreover consider the oxygen exchange equilibrium

$$\mathrm{O_O^\times} \rightleftarrows \mathrm{V_O^{\bullet\bullet}} + 2e + \frac{1}{2}\mathrm{O_2} \tag{C.3}$$

In thermodynamic equilibrium, this renders the law of mass action

$$n^2 c_{\mathrm{V_O^{\bullet\bullet}}} (a\mathrm{O_2})^{-1/2} = K^0_\mathrm{red} \cdot \exp\left(-\frac{\Delta H_\mathrm{red}}{k_\mathrm{B}T}\right) \tag{C.4}$$

Here, $\Delta\, H_\mathrm{red}$ denotes the enthalpy of reduction of the material, *i.e.* the actual enthalpy required to form an oxygen vacancy, and $c_{\mathrm{V_O^{\bullet\bullet}}}$ the concentration of doubly ionized oxygen vacancies. Equation C.4 implies the oxygen pressure / activity dependence of the oxygen vacancy concentration and the electron concentration in oxides. In the bulk, the three variable parameters *n*, *p* and $c_{\mathrm{V_O^{\bullet\bullet}}}$ are coupled *via* the charge-neutrality condition

$$2c_{\mathrm{V_O^{\bullet\bullet}}} + c_{\mathrm{Nb^\bullet_{eff}}} + p - n = 0 \tag{C.5}$$

allowing to solve for all defect concentrations at a given *T* and $a\mathrm{O_2}$. Note that the reaction constants and enthalpies are available in the literature[107, 108, 113], as listed in table C.1.

At moderate temperature, space charge formation at the surface of $\mathrm{SrTiO_3}$ is described by 1) formation of surface strontium vacancies *via* the partial Schottky-equilibrium[108, 111, 197] and 2) by a reduction of the local enthalpy of formation for oxygen vacancies[42, 89, 102], which is reduced by Δg = -1.4 eV as compared to the bulk value. For the surface-terminating unit cell of the STNNi layer we therefore additionally assume an active partial Schottky-equilibrium

$$\mathrm{Sr_{Sr}^\times} + \mathrm{O_O^\times} \rightleftarrows \mathrm{V_O^{\bullet\bullet}} + \mathrm{V_{Sr}''} + (\mathrm{SrO})_\mathrm{sp} \tag{C.6}$$

and the corresponding law of mass action

$$c_{\mathrm{V_O^{\bullet\bullet}}} c_{\mathrm{V_{Sr}''}} = K^0_\mathrm{S} \cdot \exp\left(-\frac{\Delta H_\mathrm{S}}{k_\mathrm{B}T}\right) \tag{C.7}$$

The active surface Schottky-equilibrium results in the formation of surface strontium vacancies in oxidizing conditions which yield an electron depletion layer close the surface and a repelling electric field for acceptor-type dopants, such as Ni. For the oxygen exchange equilibrium at the surface, we moreover use ΔH_{red} (surface) = ΔH_{red} (bulk) - 1.4 eV. This condition reflects an energetically favoured formation of oxygen vacancies in the surface-near region, well discussed in the literature and essentially allows the inversion of the space charge potential at low oxygen activity, where oxygen vacancies become the dominant defect species in highly donor doped $SrTiO_3$.

The dedicated formulation of surface equilibria results in differing defect concentrations in bulk and surface at a given temperature and oxygen activity. As a result, a redistribution of defects *via* diffusion and drift is triggered which essentially leads to a balanced space charge equilibrium, in which diffusive currents driven via concentration gradients and drift currents driven via local electric fields vanish. This equilibrium moreover corresponds to the minimum in Gibbs free energy of the system, defining the thermodynamic equilibrium state of the space charge layer. In order to solve the space charge potential $\Phi(x)$ we self-consistently solve eqs. C.2, C.4 and C.7 together the boundary conditions of

$$c_{\mathrm{def}}(x) = c_{\mathrm{def}}^{\mathrm{bulk}} \cdot \exp\left(-\frac{e\phi(x)}{k_{\mathrm{B}}T}\right) \tag{C.8}$$

$$\varepsilon\varepsilon_{\mathrm{r}}\left(\frac{d\phi(x=0)}{dx}\right) = \frac{Q}{A} \tag{C.9}$$

$$\varepsilon\varepsilon_{\mathrm{r}}\left(\frac{d\phi(x=\infty)}{dx}\right) = 0 \tag{C.10}$$

$$\varepsilon\varepsilon_{\mathrm{r}}\left(\frac{d^2\phi(x)}{dx^2}\right) = e\left(2c_{\mathrm{V_O^{\bullet\bullet}}}(x) + c_{\mathrm{Nb_{eff}^{\bullet}}} + p(x) - n(x)\right) \tag{C.11}$$

Here, equations C.9, C.10 reflect Gauss law evaluated at the surface ($x = 0$) and far from the surface, where the electric field vanishes (global charge neutrality). At the surface, the electric field $\left(\frac{d\phi(x=0)}{dx}\right)$ is given by the surface charge

$$\frac{Q}{A}(\mathrm{surface}) = ec\left(2c_{\mathrm{V_O^{\bullet\bullet}}}(0) + c_{\mathrm{Nb_{eff}^{\bullet}}} + p(0) - n(0) - 2c_{\mathrm{V_{Sr}''}}(0)\right) \tag{C.12}$$

Here, *c* denotes the lattice constant of $SrTiO_3$ and the surface concentrations $c_{\mathrm{V}_\mathrm{O}^{**}}(0)$, $c_{\mathrm{V}_\mathrm{Sr}^{\prime\prime}}(0)$ obey the surface equilibria defined in equation C.7 and C.4, considering a reduced reduction enthalpy. Equation C.11 reflects the Poisson equation, whereas the local charge density is given by the sum of local defect concentrations within the space charge layer.

All equations can be solved numerically using a finite-element approach, revealing the established surface space charge potential $\Phi(x)$ as shown in the main chapter C.12, as well as all defect concentration profiles within the surface layer. Table C.1 summarizes all numerical values used for the space charge calculations as available in the listed literature.

Table C.1: Thermodynamic data for $SrTiO_3$.

	Thermodynamic data		Reference
Bulk	K_i^0 / cm^{-6}	$1.43 \times 10^{33} \times (T/\mathrm{K})^3$	[107]
	$\Delta\ E_\mathrm{g}$ / eV	3.17 - $5.66 \times 10^{-4} \times (T/\mathrm{K})$	[107]
	K_red^0 / cm^{-9} bar$^{-1/2}$	5×10^{71}	[107]
	H_red / eV	5.7	[225]
Surface	K_i^0 / cm^{-6}	$1.43 \times 10^{33} \times (T/\mathrm{K})^3$	[107]
	$\Delta\ E_\mathrm{g}$ / eV	3.17 - $5.66 \times 10^{-4} \times (T/\mathrm{K})$	[107]
	K_red^0 / cm^{-9} bar$^{-1/2}$	5×10^{71}	[107]
	H_red / eV	4.3	[42, 89]
	K_S^0 / cm^{-6}	3×10^{44}	[107, 108]
	H_S / eV	2.5	[107, 108]
SCR	$\varepsilon(T)$	$\frac{78400}{(T/\mathrm{K})-28}$	[108]

Appendix D

Non-reversibility of Ni exsolution in STNNi

In order to investigate the reversibility of Ni exsolution in STNNi, thin film of different Ni-doping level were employed in redox experiments. Here, the samples were jointly reduced and oxidized by thermal annealing, respectively. The surface morphology was studied by AFM imaging in the as-prepared, reduced and re-oxidized state. The STNNi thin films of varying doping level exhibit a smooth surface morphology in the as-prepared state (first column). As can be seen in Fig. D.1, the exsolution of nanoparticles is visible for the doped thin films, where the particle density increases with increasing doping level x (second column). Notably, also for the undoped reference sample ($x = 0.0$) the formation of somewhat larger island-like surface phases can be observed. The particle remain stable at the thin film surface upon re-oxidation in air (third column). Evidently, the exsolution of nickel in STNNi is not reversible, even for low doping concentrations.

Fig. D.2 exemplary diffractograms of STNNi in the as-prepared, the reduced state and the re-oxidized state are shown. Notably, the data is obtained from the STNNi thin film with $x = 0.05$, discussed in Fig. D.1, depicted above. As can be seen, thermal reduction results in the structural relaxation of the c-lattice parameter (*cf.* chapter 6. After re-oxidation, the original position of the (004) thin film diffraction peak is nearly fully recovered. The observation indicates, that the phase transformation of Ni-rich nanostructures, and hence the reordering of the semi-coherent interface between the embedded phase and the surrounding host lattice may be fully reversible. However, the nanoparticles that exsolved to the surface during the first reduction cycle, remain stable at the surface and do not re-dissolve within the oxide host lattice, as discussed above.

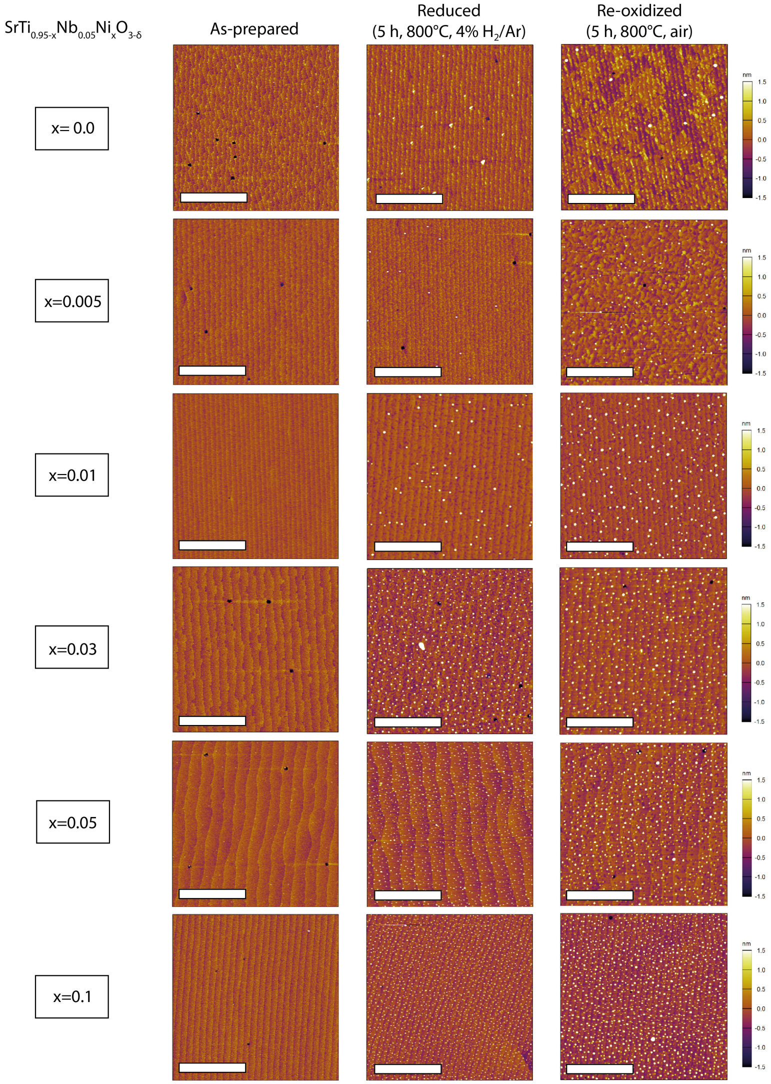

Figure D.1: AFM imaging of 50 nm thick epitaxial $SrTi_{0.95-x}Nb_{0.05}Ni_xO_{3-\delta}$ thin films with different Ni-doping levels between x = 0.0 - 0.1 deposited on STO. The surface morphology of the as-prepared state is compared to the reduced state (T = 800°C, 5 h, 4 % H_2 / Ar) and the re-oxidized state (T = 800°C, 5 h, air) of the samples. The scan size is 5 x 5 μm^2 with scale bars of 2 μm.

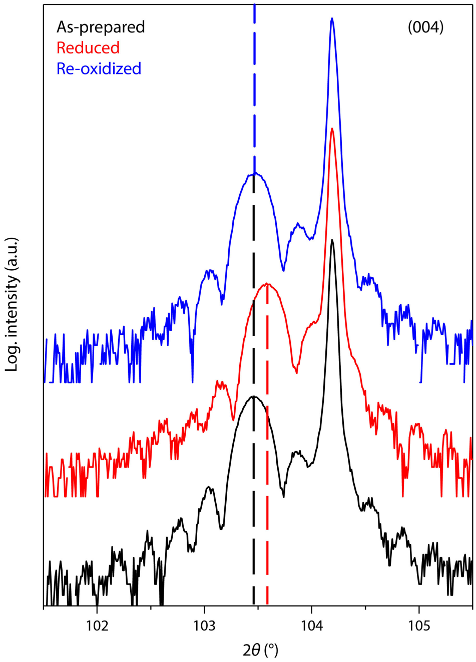

Figure D.2: X-ray diffraction analysis in 2θ-ω-geometry of an epitaxial $SrTi_{0.9}Nb_{0.05}Ni_{0.05}O_{3-\delta}$ thin film, comparing the as-prepared, reduced (T = 800°C, 5 h, 4 % H_2 / Ar) and re-oxidized state (T = 800°C, 5 h, air). The (004) diffraction peak shifts to lower diffraction angles upon reduction. After re-oxidation the original position of the thin film peak nearly fully recovered. The thin film thickness is 50 nm.

Abbreviations

1D One-dimensional

2D Two-dimensional

3D Three-dimensional

AFM Atomic force microscopy

B.E. Binding energy

BHF Buffered hydrofluoric acid

CCD Charge-coupled device

CSL Coincidence site lattice

EBSD Electron backscatter diffraction

EDXS Energy-dispersive X-ray spectroscopy

FWHM Full width half maximum

GIXS Grazing incidence X-ray scattering

HAADF High-angle annular dark-field

HF Hydrofluoric acid

HT-XRD High-temperature X-ray diffraction

ICP-MS Inductively coupled plasma mass spectrometry

ICP-OES Inductively coupled optical emission spectroscopy

LEIS Low-energy ion scattering

LPM Liters per minute

MOR Mixed oxide route

NAP-XPS Near ambient pressure X-ray photoelectron spectroscopy

Nb:STO Nb-doped (0.5wt%) strontium titanate substrate

PLD Pulsed laser deposition

RHEED Reflection high-energy electron diffraction

RMS Root mean square

RP Ruddlesden-Popper

RPM Rounds per minute

RSF Relative sensitivity factor

RSM Reciprocal space mapping

SAED Selected area electron diffraction

sccm standard cubic centimeters per minute

SCR Space charge region

SEM Secondary electron microscopy

SIMS Secondary ion mass spectrometry

STEM Scanning transmission electron microscopy

STNb Nb-doped strontium titanate / $SrTi_{0.95}Nb_{0.05}O_{3-\delta}$

STNi Ni-doped strontium titanate / $SrTi_{0.95}Ni_{0.05}O_{3-\delta}$

STNNi Nb- and Ni- co-doped strontium titanate / $SrTi_{0.9}Nb_{0.05}Ni_{0.05}O_{3-\delta}$

STO Strontium titanate / $SrTiO_{3-\delta}$

TEM Transmission electron microscopy

UHV Ultra high vacuum

VAN Vertically aligned nanostructures

VSM Vibrating sample magnetometry

XPS X-ray photoelectron spectroscopy

XRD X-ray diffraction

YSZ Yttria-stabilized zirconia

Bibliography

[1] J. Rogelj, M. Schaeffer, M. Meinshausen, R. Knutti, J. Alcamo, K. Riahi, and W. Hare, "Zero emission targets as long-term global goals for climate protection," *Environmental Research Letters*, vol. 10, no. 10, p. 105007, 2015.

[2] J. Rogelj, G. Luderer, R. C. Pietzcker, E. Kriegler, M. Schaeffer, V. Krey, and K. Riahi, "Energy system transformations for limiting end-of-century warming to below 1.5 c," *Nature Climate Change*, vol. 5, no. 6, pp. 519–527, 2015.

[3] A. Hauch, R. Küngas, P. Blennow, A. B. Hansen, J. B. Hansen, B. V. Mathiesen, and M. B. Mogensen, "Recent advances in solid oxide cell technology for electrolysis," *Science*, vol. 370, no. 6513, 2020.

[4] P. Boldrin and N. P. Brandon, "Progress and outlook for solid oxide fuel cells for transportation applications," *Nature Catalysis*, vol. 2, no. 7, pp. 571–577, 2019.

[5] S. J. Davis, N. S. Lewis, M. Shaner, S. Aggarwal, D. Arent, I. L. Azevedo, S. M. Benson, T. Bradley, J. Brouwer, Y.-M. Chiang *et al.*, "Net-zero emissions energy systems," *Science*, vol. 360, no. 6396, 2018.

[6] C. Duan, R. J. Kee, H. Zhu, C. Karakaya, Y. Chen, S. Ricote, A. Jarry, E. J. Crumlin, D. Hook, R. Braun *et al.*, "Highly durable, coking and sulfur tolerant, fuel-flexible protonic ceramic fuel cells," *Nature*, vol. 557, no. 7704, pp. 217–222, 2018.

[7] A. S. Aricò, P. Bruce, B. Scrosati, J.-M. Tarascon, and W. van Schalkwijk, "Nanostructured materials for advanced energy conversion and storage devices," *Nature Materials*, vol. 4, no. 5, pp. 366–377, 2005.

[8] E. D. Wachsman and K. T. Lee, "Lowering the temperature of solid oxide fuel cells," *Science*, vol. 334, no. 6058, pp. 935–939, 2011.

[9] H. Mistry, A. S. Varela, S. Kühl, P. Strasser, and B. R. Cuenya, "Nanostructured electrocatalysts with tunable activity and selectivity," *Nature Reviews Materials*, vol. 1, no. 4, pp. 1–14, 2016.

[10] T. Z. Sholklapper, H. Kurokawa, C. P. Jacobson, S. J. Visco, and L. C. De Jonghe, "Nanostructured solid oxide fuel cell electrodes," *Nano letters*, vol. 7, no. 7, pp. 2136–2141, 2007.

[11] L. Y. Chang, A. S. Barnard, L. C. Gontard, and R. E. Dunin-Borkowski, "Resolving the structure of active sites on platinum catalytic nanoparticles," *Nano letters*, vol. 10, no. 8, pp. 3073–3076, 2010.

[12] O. Celikbilek, C.-A. Thieu, F. Agnese, E. Calì, C. Lenser, N. H. Menzler, J.-W. Son, S. J. Skinner, and E. Djurado, "Enhanced catalytic activity of nanostructured, a-site deficient $(La_{0.7}Sr_{0.3})_{0.95}(Co_{0.2}Fe_{0.8})O_{3-\delta}$ for sofc cathodes," *Journal of Materials Chemistry A*, vol. 7, no. 43, pp. 25 102–25 111, 2019.

[13] P. C. Vesborg and T. F. Jaramillo, "Addressing the terawatt challenge: scalability in the supply of chemical elements for renewable energy," *RSC Advances*, vol. 2, no. 21, pp. 7933–7947, 2012.

[14] Y. Nishihata, J. Mizuki, T. Akao, H. Tanaka, M. Uenishi, M. Kimura, T. Okamoto, and N. Hamada, "Self-regeneration of a pd-perovskite catalyst for automotive emissions control," *Nature*, vol. 418, no. 6894, pp. 164–167, 2002.

[15] J. Myung, D. Neagu, D. N. Miller, and J. T. S. Irvine, "Switching on electrocatalytic activity in solid oxide cells," *Nature*, vol. 537, no. 7621, pp. 528–531, 2016.

[16] J. T. Irvine, D. Neagu, M. C. Verbraeken, C. Chatzichristodoulou, C. Graves, and M. B. Mogensen, "Evolution of the electrochemical interface in high-temperature fuel cells and electrolysers," *Nature Energy*, vol. 1, no. 1, pp. 1–13, 2016.

[17] O. Kwon, S. Joo, S. Choi, S. Sengodan, and G. Kim, "Review on exsolution and its driving forces in perovskites," *Journal of Physics: Energy*, vol. 2, no. 3, p. 032001, 2020.

[18] J. H. Kim, J. K. Kim, J. Liu, A. Curcio, J.-S. Jang, I.-D. Kim, F. Ciucci, and W. Jung, "Nanoparticle ex-solution for supported catalysts: Materials design, mechanism and future perspectives," *ACS nano*, vol. 15, no. 1, pp. 81–110, 2020.

[19] D. Neagu, G. Tsekouras, D. N. Miller, H. Ménard, and J. T. Irvine, "In situ growth of nanoparticles through control of non-stoichiometry," *Nature chemistry*, vol. 5, no. 11, pp. 916–923, 2013.

[20] H. Ellingham, "Transactions and communications," *Journal of the Society of Chemical Industry*, vol. 63, no. 5, pp. 125–160, 1944.

[21] Y. Gao, D. Chen, M. Saccoccio, Z. Lu, and F. Ciucci, "From material design to mechanism study: nanoscale ni exsolution on a highly active a-site deficient anode material for solid oxide fuel cells," *Nano Energy*, vol. 27, pp. 499–508, 2016.

[22] Y. Sun, J. Li, Y. Zeng, B. S. Amirkhiz, M. Wang, Y. Behnamian, and J. Luo, "A-site deficient perovskite: the parent for in situ exsolution of highly active, regenerable nano-particles as sofc anodes," *Journal of Materials Chemistry A*, vol. 3, no. 20, pp. 11 048–11 056, 2015.

[23] E. Y. Konysheva, X. Xu, and J. T. Irvine, "On the existence of a-site deficiency in perovskites and its relation to the electrochemical performance," *Advanced Materials*, vol. 24, no. 4, pp. 528–532, 2012.

[24] O. Kwon, S. Sengodan, K. Kim, G. Kim, H. Y. Jeong, J. Shin, Y.-W. Ju, J. W. Han, and G. Kim, "Exsolution trends and co-segregation aspects of self-grown catalyst nanoparticles in perovskites," *Nature communications*, vol. 8, no. 1, pp. 1–7, 2017.

[25] J. Wang, J. Yang, A. K. Opitz, W. Bowman, R. Bliem, G. Dimitrakopoulos, A. Nenning, I. Waluyo, A. Hunt, J.-J. Gallet *et al.*, "Tuning point defects by elastic strain modulates nanoparticle exsolution on perovskite oxides," *Chemistry of Materials*, vol. 33, no. 13, pp. 5021–5034, 2021.

[26] H. Lv, L. Lin, X. Zhang, Y. Song, H. Matsumoto, C. Zeng, N. Ta, W. Liu, D. Gao, G. Wang *et al.*, "In situ investigation of reversible exsolution/dissolution of cofe alloy nanoparticles in a co-doped $Sr_2Fe_{1.5}Mo_{0.5}O_{6-\delta}$ cathode for CO_2 electrolysis," *Advanced Materials*, vol. 32, no. 6, p. 1906193, 2020.

[27] H. Han, J. Park, S. Y. Nam, K. J. Kim, G. M. Choi, S. S. Parkin, H. M. Jang, and J. T. Irvine, "Lattice strain-enhanced exsolution of nanoparticles in thin films," *Nature communications*, vol. 10, no. 1, pp. 1–8, 2019.

[28] T.-S. Oh, E. K. Rahani, D. Neagu, J. T. Irvine, V. B. Shenoy, R. J. Gorte, and J. M. Vohs, "Evidence and model for strain-driven release of metal nanocatalysts from perovskites during exsolution," *The journal of physical chemistry letters*, vol. 6, no. 24, pp. 5106–5110, 2015.

[29] K. J. Kim, H. Han, T. Defferriere, D. Yoon, S. Na, S. J. Kim, A. M. Dayaghi, J. Son, T.-S. Oh, H. M. Jang *et al.*, "Facet-dependent in situ growth of nanoparticles in epitaxial thin films: the role of interfacial energy," *Journal of the American Chemical Society*, vol. 141, no. 18, pp. 7509–7517, 2019.

[30] W. Lee, J. W. Han, Y. Chen, Z. Cai, and B. Yildiz, "Cation size mismatch and charge interactions drive dopant segregation at the surfaces of manganite

perovskites," *Journal of the American Chemical Society*, vol. 135, no. 21, pp. 7909–7925, 2013.

[31] Y. Li, W. Zhang, Y. Zheng, J. Chen, B. Yu, Y. Chen, and M. Liu, "Controlling cation segregation in perovskite-based electrodes for high electro-catalytic activity and durability," *Chemical Society Reviews*, vol. 46, no. 20, pp. 6345–6378, 2017.

[32] D. Neagu, T.-S. Oh, D. N. Miller, H. Ménard, S. M. Bukhari, S. R. Gamble, R. J. Gorte, J. M. Vohs, and J. T. Irvine, "Nano-socketed nickel particles with enhanced coking resistance grown in situ by redox exsolution," *Nature communications*, vol. 6, no. 1, pp. 1–8, 2015.

[33] J. A. S. Ikeda and Y.-M. Chiang, "Space charge segregation at grain boundaries in titanium dioxide: I, relationship between lattice defect chemistry and space charge potential," *Journal of the American Ceramic Society*, vol. 76, no. 10, pp. 2437–2446, 1993.

[34] M. Shirpour, B. Rahmati, W. Sigle, P. A. van Aken, R. Merkle, and J. Maier, "Dopant segregation and space charge effects in proton-conducting $BaZrO_3$ perovskites," *The Journal of Physical Chemistry C*, vol. 116, no. 3, pp. 2453–2461, 2012.

[35] Y.-M. Chiang and T. Takagi, "Grain-boundary chemistry of barium titanate and strontium titanate: I, high-temperature equilibrium space charge," *Journal of the American Ceramic Society*, vol. 73, no. 11, pp. 3278–3285, 1990.

[36] S.-Y. Chung, S.-Y. Choi, H.-I. Yoon, H.-S. Kim, and H. B. Bae, "Subsurface space-charge dopant segregation to compensate surface excess charge in a perovskite oxide," *Angewandte Chemie International Edition*, vol. 55, no. 33, pp. 9680–9684, 2016.

[37] H.-I. Yoon, D.-K. Lee, H. B. Bae, G.-Y. Jo, H.-S. Chung, J.-G. Kim, S.-J. L. Kang, and S.-Y. Chung, "Probing dopant segregation in distinct cation sites at perovskite oxide polycrystal interfaces," *Nature communications*, vol. 8, no. 1, pp. 1–8, 2017.

[38] R. Waser, "Electronic properties of grain boundaries in $SrTiO_3$ and $BaTiO_3$ ceramics," *Solid State Ionics*, vol. 75, pp. 89–99, 1995.

[39] X. Guo, W. Sigle, and J. Maier, "Blocking grain boundaries in yttria-doped and undoped ceria ceramics of high purity," *Journal of the American Ceramic Society*, vol. 86, no. 1, pp. 77–87, 2003.

[40] H. L. Tuller, "Ionic conduction in nanocrystalline materials," *Solid State Ionics*, vol. 131, no. 1-2, pp. 143–157, 2000.

[41] F. Baiutti, G. Logvenov, G. Gregori, G. Cristiani, Y. Wang, W. Sigle, P. A. van Aken, and J. Maier, "High-temperature superconductivity in space-charge regions of lanthanum cuprate induced by two-dimensional doping," *Nature communications*, vol. 6, no. 1, pp. 1–8, 2015.

[42] R. A. De Souza, "The formation of equilibrium space-charge zones at grain boundaries in the perovskite oxide srtio$_3$," *Physical Chemistry Chemical Physics*, vol. 11, no. 43, pp. 9939–9969, 2009.

[43] F. Gunkel, R. Waser, A. H. Ramadan, R. A. De Souza, S. Hoffmann-Eifert, and R. Dittmann, "Space charges and defect concentration profiles at complex oxide interfaces," *Physical Review B*, vol. 93, no. 24, p. 245431, 2016.

[44] M. L. Weber and F. Gunkel, "Epitaxial catalysts for oxygen evolution reaction: model systems and beyond," *Journal of Physics: Energy*, vol. 1, no. 3, p. 031001, 2019.

[45] M. L. Weber, C. Baeumer, D. N. Mueller, L. Jin, C.-L. Jia, D. S. Bick, R. Waser, R. Dittmann, I. Valov, and F. Gunkel, "Electrolysis of water at atomically tailored epitaxial cobaltite surfaces," *Chemistry of materials*, vol. 31, no. 7, pp. 2337–2346, 2019.

[46] D. Antipin and M. Risch, "Trends of epitaxial perovskite oxide films catalyzing the oxygen evolution reaction in alkaline media," *Journal of Physics: Energy*, vol. 2, no. 3, p. 032003, 2020.

[47] H.-I. Ji, J. Hwang, K. J. Yoon, J.-W. Son, B.-K. Kim, H.-W. Lee, and J.-H. Lee, "Enhanced oxygen diffusion in epitaxial lanthanum–strontium–cobaltite thin film cathodes for micro solid oxide fuel cells," *Energy & Environmental Science*, vol. 6, no. 1, pp. 116–120, 2013.

[48] C. Baeumer, J. Li, Q. Lu, A. Y.-L. Liang, L. Jin, H. P. Martins, T. Duchoň, M. Glöß, S. M. Gericke, M. A. Wohlgemuth *et al.*, "Tuning electrochemically driven surface transformation in atomically flat LaNiO$_3$ thin films for enhanced water electrolysis," *Nature materials*, vol. 20, no. 5, pp. 674–682, 2021.

[49] K. A. Stoerzinger, W. S. Choi, H. Jeen, H. N. Lee, and Y. Shao-Horn, "Role of strain and conductivity in oxygen electrocatalysis on LaCoO$_3$ thin films," *The journal of physical chemistry letters*, vol. 6, no. 3, pp. 487–492, 2015.

[50] A. R. Akbashev, L. Zhang, J. T. Mefford, J. Park, B. Butz, H. Luftman, W. C. Chueh, and A. Vojvodic, "Activation of ultrathin SrTiO$_3$ with subsurface SrRuO$_3$ for the oxygen evolution reaction," *Energy & Environmental Science*, vol. 11, no. 7, pp. 1762–1769, 2018.

[51] G. Wan, J. W. Freeland, J. Kloppenburg, G. Petretto, J. N. Nelson, D.-Y. Kuo, C.-J. Sun, J. Wen, J. T. Diulus, G. S. Herman *et al.*, "Amorphization mechanism of $SrIrO_3$ electrocatalyst: How oxygen redox initiates ionic diffusion and structural reorganization," *Science advances*, vol. 7, no. 2, p. eabc7323, 2021.

[52] J. Irvine, J. Rupp, G. Liu, X. Xu, S. M. Haile, X. Qian, A. Snyder, R. Freer, D. Ekren, S. Skinner *et al.*, "Roadmap on inorganic perovskites for energy applications," *Journal of Physics: Energy*, vol. 3, no. 3, p. 031502, 2021.

[53] B. Hua, M. Li, Y.-F. Sun, J.-H. Li, and J.-L. Luo, "Enhancing perovskite electrocatalysis of solid oxide cells through controlled exsolution of nanoparticles," *ChemSusChem*, vol. 10, no. 17, pp. 3333–3341, 2017.

[54] W. G. Hardin, D. A. Slanac, X. Wang, S. Dai, K. P. Johnston, and K. J. Stevenson, "Highly active, nonprecious metal perovskite electrocatalysts for bifunctional metal–air battery electrodes," *The journal of physical chemistry letters*, vol. 4, no. 8, pp. 1254–1259, 2013.

[55] F. Horikiri, L. Han, N. Iizawa, K. Sato, K. Yashiro, T. Kawada, and J. Mizusaki, "Electrical properties of Nb-doped $SrTiO_3$ ceramics with excess TiO_2 for sofc anodes and interconnects," *Journal of the Electrochemical Society*, vol. 155, no. 1, p. B16, 2007.

[56] N. Brandon, S. Skinner, and B. Steele, "Recent advances in materials for fuel cells," *Annual Review of Materials Research*, vol. 33, no. 1, pp. 183–213, 2003.

[57] M. Li, M. J. Pietrowski, R. A. De Souza, H. Zhang, I. M. Reaney, S. N. Cook, J. A. Kilner, and D. C. Sinclair, "A family of oxide ion conductors based on the ferroelectric perovskite $Na_{0.5}Bi_{0.5}TiO_3$," *Nature materials*, vol. 13, no. 1, pp. 31–35, 2014.

[58] W. C. Chueh and S. M. Haile, "Electrochemistry of mixed oxygen ion and electron conducting electrodes in solid electrolyte cells," *Annual review of chemical and biomolecular engineering*, vol. 3, pp. 313–341, 2012.

[59] A. Aguadero, L. Fawcett, S. Taub, R. Woolley, K.-T. Wu, N. Xu, J. A. Kilner, and S. J. Skinner, "Materials development for intermediate-temperature solid oxide electrochemical devices," *Journal of Materials Science*, vol. 47, no. 9, pp. 3925–3948, 2012.

[60] R. Martínez-Coronado, J. Alonso, A. Aguadero, D. Perez-Coll, and M. Fernández-Díaz, "Neutron structural characterization and transport properties of oxidized and reduced $La_{0.5}Sr_{0.5}M_{0.5}Ti_{0.5}O_3$ (M = Mn, Fe) perovskites: Possible electrode materials in solid-oxide fuel cells," *Journal of Applied Physics*, vol. 113, no. 12, p. 123708, 2013.

[61] Q. Ma, B. Iwanschitz, E. Dashjav, S. Baumann, D. Sebold, I. Arul Raj, A. Mai, and F. Tietz, "Microstructural variations and their influence on the performance of solid oxide fuel cells based on yttrium-substituted strontium titanate ceramic anodes," *Journal of Power Sources*, vol. 279, pp. 678–685, 2015.

[62] O. A. Marina, N. L. Canfield, and J. W. Stevenson, "Thermal, electrical, and electrocatalytical properties of lanthanum-doped strontium titanate," *Solid State Ionics*, vol. 149, no. 1-2, pp. 21–28, 2002.

[63] Q. Fu, F. Tietz, D. Sebold, S. Tao, and J. T. Irvine, "An efficient ceramic-based anode for solid oxide fuel cells," *Journal of Power Sources*, vol. 171, no. 2, pp. 663–669, 2007.

[64] M. R. Pillai, I. Kim, D. M. Bierschenk, and S. A. Barnett, "Fuel-flexible operation of a solid oxide fuel cell with $Sr_{0.8}La_{0.2}TiO_3$ support," *Journal of Power Sources*, vol. 185, no. 2, pp. 1086–1093, 2008.

[65] G. Kim, M. D. Gross, W. Wang, J. M. Vohs, and R. J. Gorte, "SOFC anodes based on LST–YSZ composites and on $Y_{0.04}Ce_{0.48}Zr_{0.48}O_2$," vol. 155, no. 4, p. B360, 2008.

[66] C. Savaniu and J. Irvine, "La-doped $SrTiO_3$ as anode material for IT-SOFC," *Solid State Ionics*, vol. 192, no. 1, pp. 491–493, 2011.

[67] B. Madsen, W. Kobsiriphat, Y. Wang, L. Marks, and S. Barnett, "Nucleation of nanometer-scale electrocatalyst particles in solid oxide fuel cell anodes," *Journal of power sources*, vol. 166, no. 1, pp. 64–67, 2007.

[68] G. Tsekouras, D. Neagu, and J. T. Irvine, "Step-change in high temperature steam electrolysis performance of perovskite oxide cathodes with exsolution of B-site dopants," *Energy & Environmental Science*, vol. 6, no. 1, pp. 256–266, 2013.

[69] T. Wei, L. Jia, H. Zheng, B. Chi, J. Pu, and J. Li, "$LaMnO_3$-based perovskite with *in-situ* exsolved Ni nanoparticles: a highly active, performance stable and coking resistant catalyst for CO_2 dry reforming of CH_4," *Applied Catalysis A: General*, vol. 564, pp. 199–207, 2018.

[70] Z. Du, H. Zhao, S. Yi, Q. Xia, Y. Gong, Y. Zhang, X. Cheng, Y. Li, L. Gu, and K. Swierczek, "High-performance anode material $Sr_2FeMo_{0.65}Ni_{0.35}O_{6-\delta}$ with *in situ* exsolved nanoparticle catalyst," *ACS Nano*, vol. 10, no. 9, pp. 8660–8669, 2016.

[71] T. Zhu, H. E. Troiani, L. V. Mogni, M. Han, and S. A. Barnett, "Ni-substituted $Sr(Ti,Fe)O_3$ SOFC anodes: achieving high performance *via* metal alloy nanoparticle exsolution," *Joule*, vol. 2, no. 3, pp. 478–496, 2018.

[72] L. Thommy, O. Joubert, J. Hamon, and M.-T. Caldes, "Impregnation *versus* exsolution: Using metal catalysts to improve electrocatalytic properties of LSCM-based anodes operating at 600°C," *International journal of hydrogen energy*, vol. 41, no. 32, pp. 14 207–14 216, 2016.

[73] D. Zubenko, S. Singh, and B. A. Rosen, "Exsolution of Re-alloy catalysts with enhanced stability for methane dry reforming," *Applied Catalysis B: Environmental*, vol. 209, pp. 711–719, 2017.

[74] D. Neagu, E. I. Papaioannou, W. K. W. Ramli, D. N. Miller, B. J. Murdoch, H. Ménard, A. Umar, A. J. Barlow, P. J. Cumpson, J. T. S. Irvine, and I. S. Metcalfe, "Demonstration of chemistry at a point through restructuring and catalytic activation at anchored nanoparticles," *Nature Communications*, vol. 8, no. 1, p. 1855, Nov 2017.

[75] K. Kousi, C. Tang, I. S. Metcalfe, and D. Neagu, "Emergence and future of exsolved materials," *Small*, p. 2006479, 2021.

[76] Y. Chen, W. Jung, Z. Cai, J. J. Kim, H. L. Tuller, and B. Yildiz, "Impact of Sr segregation on the electronic structure and oxygen reduction activity of $SrTi_{1-x}Fe_xO_3$ surfaces," *Energy & Environmental Science*, vol. 5, no. 7, pp. 7979–7988, 2012.

[77] Z. Cai, M. Kubicek, J. Fleig, and B. Yildiz, "Chemical heterogeneities on $La_{0.6}Sr_{0.4}CoO_{3-\delta}$ thin films—correlations to cathode surface activity and stability," *Chemistry of Materials*, vol. 24, no. 6, pp. 1116–1127, 2012.

[78] B. Koo, K. Kim, J. K. Kim, H. Kwon, J. W. Han, and W. Jung, "Sr segregation in perovskite oxides: why it happens and how it exists," *Joule*, vol. 2, no. 8, pp. 1476–1499, 2018.

[79] B. Wei, M. Schroeder, and M. Martin, "Surface cation segregation and chromium deposition on the double-perovskite oxide $PrBaCo_2O_{5+\delta}$," *ACS applied materials & interfaces*, vol. 10, no. 10, pp. 8621–8629, 2018.

[80] P. A. Cox, *Transition metal oxides: an introduction to their electronic structure and properties*. Oxford University Press, 2010, vol. 27.

[81] M. J. Akhtar, Z.-U.-N. Akhtar, R. A. Jackson, and C. R. A. Catlow, "Computer simulation studies of strontium titanate," *Journal of the American Ceramic Society*, vol. 78, no. 2, pp. 421–428, 1995.

[82] M. Kawasaki, K. Takahashi, T. Maeda, R. Tsuchiya, M. Shinohara, O. Ishiyama, T. Yonezawa, M. Yoshimoto, and H. Koinuma, "Atomic control of the $SrTiO_3$ crystal surface," *Science*, vol. 266, no. 5190, pp. 1540–1542, 1994.

[83] G. Koster, B. L. Kropman, G. J. Rijnders, D. H. Blank, and H. Rogalla, "Quasi-ideal strontium titanate crystal surfaces through formation of strontium hydroxide," *Applied Physics Letters*, vol. 73, no. 20, pp. 2920–2922, 1998.

[84] R. A. De Souza, V. Metlenko, D. Park, and T. E. Weirich, "Behavior of oxygen vacancies in single-crystal $SrTiO_3$: Equilibrium distribution and diffusion kinetics," *Physical Review B*, vol. 85, no. 17, p. 174109, 2012.

[85] C. Noguera, *Physics and Chemistry at Oxide Surfaces*. Cambridge University Press, 1996.

[86] D. M. Smyth, *The Defect Chemistry of Metal Oxides*, ser. The Defect Chemistry of Metal Oxides, 2000.

[87] B. Fultz, *Phase transitions in materials*. Cambridge University Press, 2020.

[88] K. Szot, W. Speier, R. Carius, U. Zastrow, and W. Beyer, "Localized metallic conductivity and self-healing during thermal reduction of $SrTiO_3$," *Phys. Rev. Lett.*, vol. 88, no. 7, p. 075508, 2002.

[89] R. De Souza, F. Gunkel, S. Hoffmann-Eifert, and R. Dittmann, "Finite-size versus interface-proximity effects in thin-film epitaxial $SrTiO_3$," *Physical Review B*, vol. 89, no. 24, p. 241401, 2014.

[90] G. Gottstein, "Crystal defects," in *Physical Foundations of Materials Science*. Springer, 2004, pp. 63–106.

[91] Z. Zhang, W. Sigle, and M. Rühle, "Atomic and electronic characterization of the a [100] dislocation core in $SrTiO_3$," *Physical Review B*, vol. 66, no. 9, p. 094108, 2002.

[92] C. Jia, A. Thust, and K. Urban, "Atomic-scale analysis of the oxygen configuration at a $SrTiO_3$ dislocation core," *Physical review letters*, vol. 95, no. 22, p. 225506, 2005.

[93] G. Koster, B. L. Kropman, G. J. Rijnders, D. H. Blank, and H. Rogalla, "Influence of the surface treatment on the homoepitaxial growth of $SrTiO_3$," *Materials Science and Engineering: B*, vol. 56, no. 2-3, pp. 209–212, 1998.

[94] C. Xu, H. Du, A. J. van der Torren, J. Aarts, C.-L. Jia, and R. Dittmann, "Formation mechanism of ruddlesden-popper-type antiphase boundaries during the kinetically limited growth of Sr rich $SrTiO_3$ thin films," *Scientific reports*, vol. 6, no. 1, pp. 1–8, 2016.

[95] L. Jin, M. Zapf, M. Stübinger, M. Kamp, M. Sing, R. Claessen, and C.-L. Jia, "Atomic-scale interface structure in domain matching epitaxial $BaBiO_3$ thin films grown on $SrTiO_3$ substrates," *physica status solidi (RRL)–Rapid Research Letters*, vol. 14, no. 6, p. 2000054, 2020.

[96] A. Trampert and K. Ploog, "Heteroepitaxy of large-misfit systems: Role of coincidence lattice," *Crystal Research and Technology: Journal of Experimental and Industrial Crystallography*, vol. 35, no. 6-7, pp. 793–806, 2000.

[97] T. Suzuki, Y. Nishi, and M. Fujimoto, "Defect structure in homoepitaxial non-stoichiometric strontium titanate thin films," *Philosophical Magazine A*, vol. 80, no. 3, pp. 621–637, 2000.

[98] A. Le Claire, "Diffusion," in *Treatise on solid state chemistry*. Springer, 1976.

[99] H. Mehrer, *Diffusion in solids: fundamentals, methods, materials, diffusion-controlled processes*. Springer Science & Business Media, 2007.

[100] T. Heisig, J. Kler, H. Du, C. Baeumer, F. Hensling, M. Glöß, M. Moors, A. Locatelli, T. O. Menteş, F. Genuzio, J. Mayer, R. A. De Souza, and R. Dittmann, "Antiphase boundaries constitute fast cation diffusion paths in $SrTiO_3$ memristive devices," *Advanced Functional Materials*, vol. 30, no. 48, p. 2004118, 2020.

[101] R. De Souza, "Oxygen diffusion in $SrTiO_3$ and related perovskite oxides," *Advanced Functional Materials*, vol. 25, no. 40, pp. 6326–6342, 2015.

[102] V. Metlenko, A. H. H. Ramadan, F. Gunkel, H. Du, H. Schraknepper, S. Hoffmann-Eifert, R. Dittmann, R. Waser, and R. A. De Souza, "Do dislocations act as atomic autobahns for oxygen in the perovskite oxide $SrTiO_3$?" *Nanoscale*, vol. 6, no. 21, pp. 12 864–12 876, 2014.

[103] R. Merkle and J. Maier, "How is oxygen incorporated into oxides? a comprehensive kinetic study of a simple solid-state reaction with $SrTiO_3$ as a model material," *Angewandte Chemie International Edition*, vol. 47, no. 21, pp. 3874–3894, 2008.

[104] H. B. Callen, "Thermodynamics and an introduction to thermostatistics," 1998.

[105] F. Kröger and H. Vink, "Relations between the concentrations of imperfections in crystalline solids," *Solid state physics*, vol. 3, pp. 307–435, 1956.

[106] F. Gunkel, "The role of defects at functional interfaces between polar and non-polar perovskite oxides," 2013, Aachen, Techn. Hochsch., Diss., 2013.

[107] R. Moos and K. H. Hardtl, "Defect chemistry of donor-doped and undoped strontium titanate ceramics between 1000° and 1400°C," *Journal of the American Ceramic Society*, vol. 80, no. 10, pp. 2549–2562, 1997.

[108] R. Meyer, A. F. Zurhelle, R. A. De Souza, R. Waser, and F. Gunkel, "Dynamics of the metal-insulator transition of donor-doped $SrTiO_3$," *Physical Review B*, vol. 94, no. 11, p. 115408, 2016.

[109] M. Lewin, C. Baeumer, F. Gunkel, A. Schwedt, F. Gaussmann, J. Wueppen, P. Meuffels, B. Jungbluth, J. Mayer, R. Dittmann *et al.*, "Nanospectroscopy of infrared phonon resonance enables local quantification of electronic properties in doped $SrTiO_3$ ceramics," *Advanced functional materials*, vol. 28, no. 42, p. 1802834, 2018.

[110] T. Baiatu, R. Waser, and K.-H. Härdtl, "Dc electrical degradation of perovskite-type titanates: Iii, a model of the mechanism," *Journal of the American Ceramic Society*, vol. 73, no. 6, pp. 1663–1673, 1990.

[111] M. Andrä, F. Dvořák, M. Vorokhta, S. Nemšák, V. Matolín, C. M. Schneider, R. Dittmann, F. Gunkel, D. N. Mueller, and R. Waser, "Oxygen partial pressure dependence of surface space charge formation in donor-doped $SrTiO_3$," *APL materials*, vol. 5, no. 5, p. 056106, 2017.

[112] F. Gunkel, P. Brinks, S. Hoffmann-Eifert, R. Dittmann, M. Huijben, J. Kleibeuker, G. Koster, G. Rijnders, and R. Waser, "Influence of charge compensation mechanisms on the sheet electron density at conducting $LaAlO_3/SrTiO_3$-interfaces," *Applied physics letters*, vol. 100, no. 5, p. 052103, 2012.

[113] A. Zurhelle, D. V. Christensen, S. Menzel, and F. Gunkel, "Dynamics of the spatial separation of electrons and mobile oxygen vacancies in oxide heterostructures," *Physical Review Materials*, vol. 4, no. 10, p. 104604, 2020.

[114] M.-A. Rose, B. Šmíd, M. Vorokhta, I. Slipukhina, M. Andrä, H. Bluhm, T. Duchoň, M. Ležaić, S. A. Chambers, R. Dittmann *et al.*, "Identifying ionic and electronic charge transfer at oxide heterointerfaces," *Advanced materials*, vol. 33, no. 4, p. 2004132, 2021.

[115] R. De Souza, J. Kilner, and J. Walker, "A SIMS study of oxygen tracer diffusion and surface exchange in $La_{0.8}Sr_{0.2}MnO_{3+\delta}$," *Materials Letters*, vol. 43, no. 1-2, pp. 43–52, 2000.

[116] M. L. Weber, "Development and analysis of tailored catalytic cobaltite layers for hydrogen production using electrochemical and spectroscopic techniques," Master thesis, Leibniz Universität Hannover, 2017.

[117] M. N. Rahaman, *Ceramic processing and sintering*. CRC press, 2017.

[118] A. E. Danks, S. R. Hall, and Z. Schnepp, "The evolution of 'sol–gel'chemistry as a technique for materials synthesis," *Materials Horizons*, vol. 3, no. 2, pp. 91–112, 2016.

[119] C. B. Carter and M. G. Norton, *Ceramic materials: science and engineering*. Springer Science & Business Media, 2007.

[120] Q. Ma, F. Tietz, A. Leonide, and E. Ivers-Tiffée, "Electrochemical performances of solid oxide fuel cells based on Y-substituted $SrTiO_3$ ceramic anode materials," *Journal of power sources*, vol. 196, no. 17, pp. 7308–7312, 2011.

[121] R. Dittmann, "Stoichiometry in epitaxial oxide thin films," in *Epitaxial Growth of Complex Metal Oxides*, ser. Woodhead Publishing Series in Electronic and Optical Materials, G. Koster, M. Huijben, and G. Rijnders, Eds. Woodhead Publishing, 2015, pp. 231–261.

[122] P. Willmott, "Deposition of complex multielemental thin films," *Progress in Surface Science*, vol. 76, no. 6-8, pp. 163–217, 2004.

[123] F. Himpsel, J. Ortega, G. Mankey, and R. Willis, "Magnetic nanostructures," *Advances in physics*, vol. 47, no. 4, pp. 511–597, 1998.

[124] G. Koster, G. J. Rijnders, D. H. Blank, and H. Rogalla, "Imposed layer-by-layer growth by pulsed laser interval deposition," *Applied physics letters*, vol. 74, no. 24, pp. 3729–3731, 1999.

[125] A. J. H. M. Rijnders, "The initial growth of complex oxides: Study and manipulation." 2003.

[126] M. Naito, H. Yamamoto, and H. Sato, "Reflection high-energy electron diffraction and atomic force microscopy studies on homoepitaxial growth of $SrTiO_3$ (001)," *Physica C: Superconductivity*, vol. 305, no. 3-4, pp. 233–250, 1998.

[127] A. Biswas, C.-H. Yang, R. Ramesh, and Y. H. Jeong, "Atomically flat single terminated oxide substrate surfaces," *Progress in Surface Science*, vol. 92, no. 2, pp. 117–141, 2017.

[128] M. G. Blamire, J. L. MacManus-Driscoll, N. D. Mathur, and Z. H. Barber, "The materials science of functional oxide thin films," *Advanced Materials*, vol. 21, no. 38-39, pp. 3827–3839, 2009.

[129] D. G. Schlom, L.-Q. Chen, X. Pan, A. Schmehl, and M. A. Zurbuchen, "A thin film approach to engineering functionality into oxides," *Journal of the American Ceramic Society*, vol. 91, no. 8, pp. 2429–2454, 2008.

[130] G. Koster, G. Rijnders, D. H. Blank, and H. Rogalla, "Surface morphology determined by (001) single-crystal $SrTiO_3$ termination," *Physica C: Superconductivity*, vol. 339, no. 4, pp. 215–230, 2000.

[131] D. B. Williams and C. B. Carter, "The transmission electron microscope," in *Transmission electron microscopy*. Springer, 1996, pp. 3–17.

[132] P. Eaton and P. West, *Atomic force microscopy*. Oxford university press, 2010.

[133] P. W. Hawkes and J. C. Spence, *Springer Handbook of Microscopy*. Springer Nature, 2019.

[134] S. J. Pennycook and P. D. Nellist, *Scanning transmission electron microscopy: imaging and analysis*. Springer Science & Business Media, 2011.

[135] A. J. Wilkinson and P. B. Hirsch, "Electron diffraction based techniques in scanning electron microscopy of bulk materials," *Micron*, vol. 28, no. 4, pp. 279–308, Aug 1997.

[136] H. H. Brongersma, "Low-energy ion scattering," *Characterization of Materials*, pp. 2024–2044, 2012.

[137] H. H. Brongersma, M. Draxler, M. De Ridder, and P. Bauer, "Surface composition analysis by low-energy ion scattering," *Surface Science Reports*, vol. 62, no. 3, pp. 63–109, 2007.

[138] H. Kersell, P. Chen, H. Martins, Q. Lu, F. Brausse, B.-H. Liu, M. Blum, S. Roy, B. Rude, A. Kilcoyne, H. Bluhm, and S. Nemšák, "Simultaneous ambient pressure x-ray photoelectron spectroscopy and grazing incidence x-ray scattering in gas environments," *Review of Scientific Instruments*, vol. 92, no. 4, p. 044102, Apr 2021.

[139] G. Renaud, R. Lazzari, C. Revenant, A. Barbier, M. Noblet, O. Ulrich, F. Leroy, J. Jupille, Y. Borensztein, C. R. Henry *et al.*, "Real-time monitoring of growing nanoparticles," *Science*, vol. 300, no. 5624, pp. 1416–1419, 2003.

[140] T. Metzger, I. Kegel, R. Paniago, A. Lorke, J. Peisl, J. Schulze, I. Eisele, P. Schittenhelm, and G. Abstreiter, "Shape, size, strain and correlations in quantum dot systems studied by grazing incidence x-ray scattering methods," *Thin Solid Films*, vol. 336, no. 1-2, pp. 1–8, 1998.

[141] A. Jürgensen, N. Esser, and R. Hergenröder, "Near ambient pressure XPS with a conventional X-ray source," *Surface and interface analysis*, vol. 44, no. 8, pp. 1100–1103, 2012.

[142] T. Higuchi, T. Tsukamoto, N. Sata, M. Ishigame, Y. Tezuka, and S. Shin, "Electronic structure of *p*-type $SrTiO_3$ by photoemission spectroscopy," *Physical Review B*, vol. 57, no. 12, p. 6978, 1998.

[143] H. Hug, *Instrumentelle Analytik: Theorie und Praxis*. Verlag Europa-Lehrmittel Nourney, Vollmer, 2011.

[144] S. C. Wilschefski and M. R. Baxter, "Inductively coupled plasma mass spectrometry: introduction to analytical aspects," *The Clinical Biochemist Reviews*, vol. 40, no. 3, p. 115, 2019.

[145] R. De Souza, J. Zehnpfenning, M. Martin, and J. Maier, “Determining oxygen isotope profiles in oxides with Time-of-Flight SIMS,” *Solid State Ionics*, vol. 176, no. 15-16, pp. 1465–1471, 2005.

[146] M. L. Weber, Q. Ma, P. Meuffels, F. V. Hensling, C. Lenser, F. Gunkel, N. H. Menzler, R. Dittmann, R. Waser, and O. Guillon, “Development of epitaxial thin film model electrodes for the systematic investigation of metal exsolution from MIEC perovskite oxides,” *ECS Transactions*, vol. 91, no. 1, p. 1783, 2019.

[147] M. L. Weber, M. Wilhelm, L. Jin, U. Breuer, R. Dittmann, R. Waser, O. Guillon, C. Lenser, and F. Gunkel, “Exsolution of embedded nanoparticles in defect engineered perovskite layers,” *ACS Nano*, vol. 15, no. 3, pp. 4546–4560, 2021.

[148] K. Szot, W. Speier, J. Herion, and C. Freiburg, “Restructuring of the surface region in $SrTiO_3$,” *Applied Physics A*, vol. 64, no. 1, pp. 55–59, 1996.

[149] P. Blennow, A. Hagen, K. K. Hansen, L. R. Wallenberg, and M. Mogensen, “Defect and electrical transport properties of Nb-doped $SrTiO_3$,” *Solid State Ionics*, vol. 179, no. 35-36, pp. 2047–2058, 2008.

[150] P. Blennow, K. K. Hansen, L. R. Wallenberg, and M. Mogensen, “Synthesis of nb-doped $srtio_3$ by a modified glycine-nitrate process,” *Journal of the European Ceramic Society*, vol. 27, no. 13, pp. 3609–3612, Jan 2007.

[151] M. Schmidbauer, A. Kwasniewski, and J. Schwarzkopf, “High-precision absolute lattice parameter determination of $SrTiO_3$, $DyScO_3$ and $NdGaO_3$ single crystals,” *Acta Crystallographica Section B: Structural Science*, vol. 68, no. 1, pp. 8–14, 2012.

[152] C. Rodenbücher, M. Luysberg, A. Schwedt, V. Havel, F. Gunkel, J. Mayer, and R. Waser, “Homogeneity and variation of donor doping in verneuil-grown $SrTiO_3$:Nb single crystals,” *Scientific reports*, vol. 6, no. 1, pp. 1–8, 2016.

[153] R. D. Shannon, “Revised effective ionic radii and systematic studies of interatomic distances in halides and chalcogenides,” *Acta Crystallographica Section A*, vol. 32, no. 5, pp. 751–767, Sep 1976.

[154] F. V. E. Hensling, “Defect engineering in oxide thin films,” 2019.

[155] C. Baeumer, C. Xu, F. Gunkel, N. Raab, R. A. Heinen, A. Koehl, and R. Dittmann, “Surface termination conversion during $SrTiO_3$ thin film growth revealed by x-ray photoelectron spectroscopy,” *Scientific reports*, vol. 5, no. 1, pp. 1–11, 2015.

[156] A. Chen, J.-M. Hu, P. Lu, T. Yang, W. Zhang, L. Li, T. Ahmed, E. Enriquez, M. Weigand, Q. Su *et al.*, “Role of scaffold network in controlling strain

and functionalities of nanocomposite films," *Science advances*, vol. 2, no. 6, p. e1600245, 2016.

[157] F. Baiutti, F. Chiabrera, M. Acosta, D. Diercks, D. Parfitt, J. Santiso, X. Wang, A. Cavallaro, A. Morata, H. Wang *et al.*, "A high-entropy manganite in an ordered nanocomposite for long-term application in solid oxide cells," *Nature communications*, vol. 12, no. 1, pp. 1–11, 2021.

[158] J. L. MacManus-Driscoll, P. Zerrer, H. Wang, H. Yang, J. Yoon, A. Fouchet, R. Yu, M. G. Blamire, and Q. Jia, "Strain control and spontaneous phase ordering in vertical nanocomposite heteroepitaxial thin films," *Nature materials*, vol. 7, no. 4, pp. 314–320, 2008.

[159] H. Zheng, J. Wang, S. Lofland, Z. Ma, L. Mohaddes-Ardabili, T. Zhao, L. Salamanca-Riba, S. Shinde, S. Ogale, F. Bai *et al.*, "Multiferroic $BaTiO_3$-$CoFe_2O_4$ nanostructures," *Science*, vol. 303, no. 5658, pp. 661–663, 2004.

[160] L. Lu, J. Wang, H. Zheng, D. Zhao, R. Wang, and J. Gui, "Spontaneous formation of filamentary Cd whiskers and degradation of CdMgYb icosahedral quasicrystal under ambient conditions," *Journal of Materials Research*, vol. 27, no. 14, pp. 1895–1904, 2012.

[161] M. Kuhn, S. Hashimoto, K. Sato, K. Yashiro, and J. Mizusaki, "Thermochemical lattice expansion in $La_{0.6}Sr_{0.4}Co_{1-y}Fe_yO_{3-\delta}$," *Solid State Ionics*, vol. 241, pp. 12–16, 2013.

[162] A. Roy, J. De Toro, V. Amaral, P. Muniz, J. Riveiro, and J. Ferreira, "Exchange bias beyond the superparamagnetic blocking temperature of the antiferromagnet in a Ni-NiO nanoparticulate system," *Journal of Applied Physics*, vol. 115, no. 7, p. 073904, 2014.

[163] S. A. Makhlouf, F. Parker, F. Spada, and A. Berkowitz, "Magnetic anomalies in NiO nanoparticles," *Journal of applied physics*, vol. 81, no. 8, pp. 5561–5563, 1997.

[164] M. Tadic, D. Nikolic, M. Panjan, and G. R. Blake, "Magnetic properties of NiO (nickel oxide) nanoparticles: Blocking temperature and Neel temperature," *Journal of Alloys and Compounds*, vol. 647, pp. 1061–1068, 2015.

[165] J. Swallow, W. Woodford, Y. Chen, Q. Lu, J. Kim, D. Chen, Y.-M. Chiang, W. Carter, B. Yildiz, H. Tuller *et al.*, "Chemomechanics of ionically conductive ceramics for electrical energy conversion and storage," *Journal of Electroceramics*, vol. 32, no. 1, pp. 3–27, 2014.

[166] N. H. Perry, J. J. Kim, S. R. Bishop, and H. L. Tuller, "Strongly coupled thermal and chemical expansion in the perovskite oxide system $Sr(Ti,Fe)O_{3-\alpha}$," *Journal of Materials Chemistry A*, vol. 3, no. 7, pp. 3602–3611, 2015.

[167] S. Bishop, D. Marrocchelli, C. Chatzichristodoulou, N. H. Perry, M. B. Mogensen, H. Tuller, and E. Wachsman, "Chemical expansion: implications for electrochemical energy storage and conversion devices," *Annual Review of Materials Research*, vol. 44, pp. 205–239, 2014.

[168] F. Gunkel, D. V. Christensen, Y. Chen, and N. Pryds, "Oxygen vacancies: The (in)visible friend of oxide electronics," *Applied physics letters*, vol. 116, no. 12, p. 120505, 2020.

[169] A. M. Beale, M. Paul, G. Sankar, R. J. Oldman, C. R. A. Catlow, S. French, and M. Fowles, "Combined experimental and computational modelling studies of the solubility of nickel in strontium titanate," *Journal of Materials Chemistry*, vol. 19, no. 25, pp. 4391–4400, 2009.

[170] S. Wicklein, A. Sambri, S. Amoruso, X. Wang, R. Bruzzese, A. Koehl, and R. Dittmann, "Pulsed laser ablation of complex oxides: The role of congruent ablation and preferential scattering for the film stoichiometry," *Applied physics letters*, vol. 101, no. 13, p. 131601, 2012.

[171] D. Keeble, S. Wicklein, R. Dittmann, L. Ravelli, R. Mackie, and W. Egger, "Identification of A-and B-site cation vacancy defects in perovskite oxide thin films," *Physical review letters*, vol. 105, no. 22, p. 226102, 2010.

[172] F. Gunkel, S. Wicklein, S. Hoffmann-Eifert, P. Meuffels, P. Brinks, M. Huijben, G. Rijnders, R. Waser, and R. Dittmann, "Transport limits in defect-engineered $LaAlO_3/SrTiO_3$ bilayers," *Nanoscale*, vol. 7, no. 3, pp. 1013–1022, 2015.

[173] T. Ohnishi, M. Lippmaa, T. Yamamoto, S. Meguro, and H. Koinuma, "Improved stoichiometry and misfit control in perovskite thin film formation at a critical fluence by pulsed laser deposition," *Applied Physics Letters*, vol. 87, no. 24, p. 241919, 2005.

[174] E. Breckenfeld, A. Shah, and L. Martin, "Strain evolution in non-stoichiometric heteroepitaxial thin-film perovskites," *Journal of Materials Chemistry C*, vol. 1, no. 48, pp. 8052–8059, 2013.

[175] Y. Tokuda, S. Kobayashi, T. Ohnishi, T. Mizoguchi, N. Shibata, Y. Ikuhara, and T. Yamamoto, "Growth of Ruddlesden-Popper type faults in Sr-excess $SrTiO_3$ homoepitaxial thin films by pulsed laser deposition," *Applied Physics Letters*, vol. 99, no. 17, p. 173109, 2011.

[176] C. Brooks, L. F. Kourkoutis, T. Heeg, J. Schubert, D. Muller, and D. Schlom, "Growth of homoepitaxial $SrTiO_3$ thin films by molecular-beam epitaxy," *Applied physics letters*, vol. 94, no. 16, p. 162905, 2009.

[177] S. Wiedigen, T. Kramer, M. Feuchter, I. Knorr, N. Nee, J. Hoffmann, M. Kamlah, C. Volkert, and C. Jooss, “Interplay of point defects, biaxial strain, and thermal conductivity in homoepitaxial $SrTiO_3$ thin films,” *Applied Physics Letters*, vol. 100, no. 6, p. 061904, 2012.

[178] Z. Zhang-Yin, W. Xiao-Shan, and J. Quan-Jie, “High resolution x-ray diffraction investigation of epitaxially grown $SrTiO_3$ thin films by laser-MBE,” *Chinese Physics C*, vol. 33, no. 11, p. 949, 2009.

[179] E. A. Patterson, M. Major, W. Donner, K. Durst, K. G. Webber, and J. Rödel, “Temperature-dependent deformation and dislocation density in $SrTiO_3$ (001) single crystals,” *Journal of the American Ceramic Society*, vol. 99, no. 10, pp. 3411–3420, 2016.

[180] Z. Zhai, X. Wu, H. Cai, X. Lu, J. Hao, J. Gao, W. Tan, Q. Jia, H. Wang, and Y. Wang, “Dislocation density and strain distribution in $SrTiO_3$ film grown on (110) $DyScO_3$ substrate,” *Journal of Physics D: Applied Physics*, vol. 42, no. 10, p. 105307, 2009.

[181] H. J. Scheel, “Historical aspects of crystal growth technology,” *Journal of Crystal Growth*, vol. 211, no. 1-4, pp. 1–12, 2000.

[182] F. Martin, P. Muralt, M.-A. Dubois, and A. Pezous, “Thickness dependence of the properties of highly *c*-axis textured AlN thin films,” *Journal of Vacuum Science & Technology A: Vacuum, Surfaces, and Films*, vol. 22, no. 2, pp. 361–365, 2004.

[183] S. Singh, E. Prestat, L.-F. Huang, J. M. Rondinelli, S. J. Haigh, and B. A. Rosen, “Role of 2D and 3D defects on the reduction of $LaNiO_3$ nanoparticles for catalysis,” *Scientific reports*, vol. 7, no. 1, pp. 1–7, 2017.

[184] M. L. Weber, B. Šmíd, U. Breuer, M.-A. Rose, N. H. Menzler, R. Dittmann, R. Waser, O. Guillon, F. Gunkel, and C. Lenser, “Space charge governs the kinetics of metal exsolution,” *under review*, 2021.

[185] R. A. De Souza and M. Martin, “Using $^{18}O/^{16}O$ exchange to probe an equilibrium space-charge layer at the surface of a crystalline oxide: method and application,” *Physical Chemistry Chemical Physics*, vol. 10, no. 17, pp. 2356–2367, 2008.

[186] C. Xu, C. Bäumer, R. A. Heinen, S. Hoffmann-Eifert, F. Gunkel, and R. Dittmann, “Disentanglement of growth dynamic and thermodynamic effects in $LaAlO_3$ / $SrTiO_3$ heterostructures,” *Scientific reports*, vol. 6, no. 1, pp. 1–9, 2016.

[187] M. C. Biesinger, B. P. Payne, L. W. Lau, A. Gerson, and R. S. C. Smart, “X-ray photoelectron spectroscopic chemical state quantification of mixed nickel

metal, oxide and hydroxide systems," *Surface and Interface Analysis*, vol. 41, no. 4, pp. 324–332, 2009.

[188] M. C. Biesinger, B. P. Payne, A. P. Grosvenor, L. W. Lau, A. R. Gerson, and R. S. C. Smart, "Resolving surface chemical states in XPS analysis of first row transition metals, oxides and hydroxides: Cr, Mn, Fe, Co and Ni," *Applied Surface Science*, vol. 257, no. 7, pp. 2717–2730, 2011.

[189] B. Payne, M. Biesinger, and N. McIntyre, "Use of oxygen/nickel ratios in the XPS characterisation of oxide phases on nickel metal and nickel alloy surfaces," *Journal of Electron Spectroscopy and Related Phenomena*, vol. 185, no. 5-7, pp. 159–166, 2012.

[190] M. Mason, "Electronic structure of supported small metal clusters," *Physical review B*, vol. 27, no. 2, p. 748, 1983.

[191] G. Wertheim and S. DiCenzo, "Cluster growth and core-electron binding energies in supported metal clusters," *Physical Review B*, vol. 37, no. 2, p. 844, 1988.

[192] B. Richter, H. Kuhlenbeck, H.-J. Freund, and P. S. Bagus, "Cluster core-level binding-energy shifts: the role of lattice strain," *Physical review letters*, vol. 93, no. 2, p. 026805, 2004.

[193] G. Wertheim, "Electronic structure of metal clusters," in *Small Particles and Inorganic Clusters*. Springer, 1989, pp. 319–326.

[194] H. Zheng, Q. Zhan, F. Zavaliche, M. Sherburne, F. Straub, M. P. Cruz, L.-Q. Chen, U. Dahmen, and R. Ramesh, "Controlling self-assembled perovskite-spinel nanostructures," *Nano letters*, vol. 6, no. 7, pp. 1401–1407, 2006.

[195] V. Moshnyaga, B. Damaschke, O. Shapoval, A. Belenchuk, J. Faupel, O. Lebedev, J. Verbeeck, G. Van Tendeloo, M. Mücksch, V. Tsurkan *et al.*, "Structural phase transition at the percolation threshold in epitaxial $(La_{0.7}Ca_{0.3}MnO_3)_{1-x}:(MgO)_x$ nanocomposite films," *Nature materials*, vol. 2, no. 4, pp. 247–252, 2003.

[196] R. Muenstermann, T. Menke, R. Dittmann, S. Mi, C.-L. Jia, D. Park, and J. Mayer, "Correlation between growth kinetics and nanoscale resistive switching properties of $SrTiO_3$ thin films," *Journal of applied physics*, vol. 108, no. 12, p. 124504, 2010.

[197] M. Andrä, H. Bluhm, R. Dittmann, C. Schneider, R. Waser, D. Mueller, and F. Gunkel, "Chemical control of the electrical surface properties in donor-doped transition metal oxides," *Physical review materials*, vol. 3, no. 4, p. 044604, 2019.

[198] M. Andrä, C. Funck, N. Raab, M.-A. Rose, M. Vorokhta, F. Dvorák, B. Šmíd, V. Matolín, D. N. Mueller, R. Dittmann *et al.*, "Effect of cationic interface defects on band alignment and contact resistance in metal/oxide heterojunctions," *Advanced electronic materials*, vol. 6, no. 1, p. 1900808, 2020.

[199] S. A. Chambers, Y. Du, R. B. Comes, S. R. Spurgeon, and P. V. Sushko, "The effects of core-level broadening in determining band alignment at the epitaxial $SrTiO_3$ (001)/*p*-Ge (001) heterojunction," *Applied Physics Letters*, vol. 110, no. 8, p. 082104, 2017.

[200] V. Metlenko, W. Jung, S. R. Bishop, H. L. Tuller, and R. A. De Souza, "Oxygen diffusion and surface exchange in the mixed conducting oxides $SrTi_{1y}Fe_yO_{3-\delta}$," *Physical Chemistry Chemical Physics*, vol. 18, no. 42, pp. 29 495–29 505, 2016.

[201] S. J. Cooper, M. Niania, F. Hoffmann, and J. A. Kilner, "Back-exchange: a novel approach to quantifying oxygen diffusion and surface exchange in ambient atmospheres," *Physical Chemistry Chemical Physics*, vol. 19, no. 19, pp. 12 199–12 205, 2017.

[202] J. A. Kilner, "Optimisation of oxygen ion transport in materials for ceramic membrane devices," *Faraday Discussions*, vol. 134, no. 0, pp. 9–15, 2007.

[203] W. Lee, H. J. Jung, M. H. Lee, Y.-B. Kim, J. S. Park, R. Sinclair, and F. B. Prinz, "Oxygen surface exchange at grain boundaries of oxide ion conductors," *Advanced Functional Materials*, vol. 22, no. 5, pp. 965–971, 2012.

[204] E. Navickas, T. M. Huber, Y. Chen, W. Hetaba, G. Holzlechner, G. Rupp, M. Stöger-Pollach, G. Friedbacher, H. Hutter, B. Yildiz, and J. Fleig, "Fast oxygen exchange and diffusion kinetics of grain boundaries in sr-doped $LaMnO_3$ thin films," *Physical Chemistry Chemical Physics*, vol. 17, no. 12, pp. 7659–7669, 2015.

[205] J. A. Kilner, "Fast oxygen transport in acceptor doped oxides," *Solid State Ionics*, vol. 129, no. 1-4, pp. 13–23, 2000.

[206] T. Schemme, O. Kuschel, F. Bertram, K. Kuepper, and J. Wollschläger, "Structure and morphology of epitaxially grown Fe_3O_4/NiO bilayers on MgO (001)," *Thin Solid Films*, vol. 589, pp. 526–533, 2015.

[207] Y. Kashiwabara, M. Nakano, Y. Nakagawa, Y. Wang, H. Matsuoka, and Y. Iwasa, "Electrical conduction at the interface between insulating van der Waals materials," *Advanced Functional Materials*, vol. 29, no. 17, p. 1900354, 2019.

[208] R. Waser, "Bulk conductivity and defect chemistry of acceptor-doped strontium titanate in the quenched state," *Journal of the American Ceramic Society*, vol. 74, no. 8, pp. 1934–1940, 1991.

[209] Y. Kozuka, Y. Hikita, C. Bell, and H. Hwang, "Dramatic mobility enhancements in doped $SrTiO_3$ thin films by defect management," *Applied Physics Letters*, vol. 97, no. 1, p. 012107, 2010.

[210] H. Inoue, H. Yoon, T. A. Merz, A. G. Swartz, S. S. Hong, Y. Hikita, and H. Y. Hwang, "Delta-doped $SrTiO_3$ top-gated field effect transistor," *Applied Physics Letters*, vol. 114, no. 23, p. 231605, 2019.

[211] S. Sanna, V. Esposito, J. W. Andreasen, J. Hjelm, W. Zhang, T. Kasama, S. B. Simonsen, M. Christensen, S. Linderoth, and N. Pryds, "Enhancement of the chemical stability in confined δ-Bi_2O_3," *Nature materials*, vol. 14, no. 5, pp. 500–504, 2015.

[212] C. Korte, A. Peters, J. Janek, D. Hesse, and N. Zakharov, "Ionic conductivity and activation energy for oxygen ion transport in superlattices—the semicoherent multilayer system YSZ (ZrO_2 + 9.5 mol% Y_2O_3)/Y_2O_3," *Physical Chemistry Chemical Physics*, vol. 10, no. 31, pp. 4623–4635, 2008.

[213] H. L. Tuller, S. J. Litzelman, and W. Jung, "Micro-ionics: next generation power sources," *Physical Chemistry Chemical Physics*, vol. 11, no. 17, pp. 3023–3034, 2009.

[214] S. Taibl, G. Fafilek, and J. Fleig, "Impedance spectra of Fe-doped $SrTiO_3$ thin films upon bias voltage: inductive loops as a trace of ion motion," *Nanoscale*, vol. 8, no. 29, pp. 13 954–13 966, 2016.

[215] A. Ohtomo and H. Y. Hwang, "Surface depletion in doped $srtio_3$ thin films," *Applied Physics Letters*, vol. 84, no. 10, pp. 1716–1718, Mar 2004.

[216] M. Kindelmann, M. Stamminger, N. Schön, M. Rasinski, R.-A. Eichel, F. Hausen, M. Bram, and O. Guillon, "Erosion behavior of Y_2O_3 in fluorine-based etching plasmas: Orientation dependency and reaction layer formation," *Journal of the American Ceramic Society*, vol. 104, no. 3, pp. 1465–1474, 2021.

[217] P. Tasker, "The stability of ionic crystal surfaces," *Journal of Physics C: Solid State Physics*, vol. 12, no. 22, p. 4977, 1979.

[218] J. Goniakowski, F. Finocchi, and C. Noguera, "Polarity of oxide surfaces and nanostructures," *Reports on Progress in Physics*, vol. 71, no. 1, p. 016501, 2007.

[219] A. Pojani, F. Finocchi, and C. Noguera, "Polarity on the $SrTiO_3$ (111) and (110) surfaces," *Surface science*, vol. 442, no. 2, pp. 179–198, 1999.

[220] Z. Wang, X. Hao, S. Gerhold, M. Schmid, C. Franchini, and U. Diebold, "Vacancy clusters at domain boundaries and band bending at the $SrTiO_3$ (110) surface," *Physical Review B*, vol. 90, no. 3, p. 035436, 2014.

[221] J. A. Enterkin, A. K. Subramanian, B. C. Russell, M. R. Castell, K. R. Poeppelmeier, and L. D. Marks, "A homologous series of structures on the surface of $SrTiO_3$ (110)," *Nature materials*, vol. 9, no. 3, pp. 245–248, 2010.

[222] L. F. Zagonel, M. Bäurer, A. Bailly, O. Renault, M. Hoffmann, S. Shih, D. Cockayne, and N. Barrett, "Orientation-dependent work function of *in situ* annealed strontium titanate," *Journal of Physics: Condensed Matter*, vol. 21, no. 31, p. 314013, 2009.

[223] D. Wrana, C. Rodenbücher, W. Bełza, K. Szot, and F. Krok, "*In situ* study of redox processes on the surface of $SrTiO_3$ single crystals," *Applied Surface Science*, vol. 432, pp. 46–52, 2018.

[224] A. Gunhold, K. Gömann, L. Beuermann, M. Frerichs, G. Borchardt, V. Kempter, and W. Maus-Friedrichs, "Geometric structure and chemical composition of $SrTiO_3$ surfaces heated under oxidizing and reducing conditions," *Surface science*, vol. 507, pp. 447–452, 2002.

[225] C. Ohly, S. Hoffmann-Eifert, X. Guo, J. Schubert, and R. Waser, "Electrical conductivity of epitaxial $SrTiO_3$ thin films as a function of oxygen partial pressure and temperature," *Journal of the American Ceramic Society*, vol. 89, no. 9, pp. 2845–2852, 2006.

Acknowledgements

Since the opportunities to say thank you were rare lately, I genuinely feel that the following paragraph is one of the most important ones in this thesis. I would like to express my deepest gratitude to the many people who have supported me professionally or on a personal level over the years, many of whom have contributed directly to this work.

First of all, I would like to thank Dr. Felix Gunkel, Prof. Regina Dittmann and Prof. Rainer Waser for giving me the chance to continue my work at PGI-7 after finishing my master thesis at the institute. I can clearly remember the day I was offered the opportunity to pursue a PhD as I was extremely happy to get the chance to keep working with great colleagues and in an exciting field of research. In the course of my new role as a networking doctoral student, my work environment expanded as I was no longer employed only at PGI-7, but also at IEK-1. In this regard, I would like to thank Dr. Christian Lenser, Hon.-Prof. Norbert H. Menzler and Prof. Olivier Guillon who have been integrating me into the institute from this point on. I am truly grateful for the unique infrastructure and supportive research environment that was provided to me during my time at Forschungszentrum Jülich by all of the above mentioned. My special thanks go to Prof. Olivier Guillon and Prof. Regina Dittmann for examining my doctoral thesis and for the stimulating discussions on various occasions.

I would like to thank Felix Gunkel and Christian Lenser who have supervised my work in close exchange and who offered incredible support and mentoring. Here, I'm particularly thankful to Christian for drawing my interest to the topic of metal exsolution and for constantly challenging my writing skills. I would like to especially thank Felix for his guidance and mentoring as his support has been invaluable to my work and also to me as a person.

I am very happy about the collaborative nature of the research that made this thesis possible. Here, I would like to thank Dr. Břetislav Šmíd who has been working very hard to make our beamtime at Charles University Prague a success, while travel restrictions at this time did not allow us to support him in person. I have enjoyed the

many discussions and close cooperation at days and nights of our spectroscopy sessions. Likewise, I would like to express my warmest gratitude to Dr. Heath Kersell and Dr. Slavomir Nemšák for providing exciting insights into metal exsolution using their unique analysis techniques at Advanced Light Source, Lawrence Berkeley National Laboratory. I am very happy about the enduring collaboration and close exchange. In particular, I am grateful for the hospitality of Dr. Ainara Aguadero and Prof. Stephen Skinner as well as the entire electroceramics group at Imperial College London who have welcomed me warmly and hosted me during the final phase of my doctoral thesis. Big thanks to Sarah Fearn and Andrea Cavallaro who have been of great support during my time in London.

Furthermore, a large part of this work would have not been possible without the help of excellent collaborations with researchers of the different institutions located at Forschungszentrum Jülich. I'm most thankful to Dr. Lei Jin, Dr. Uwe Breuer, Dr. Egbert Wessel, Dr. Volker Nischwitz, Dr. Yoo Jung Sohn, Dr. Marek Wilhelm, Dr. Moritz Kindelmann, Dr. Christoph Baeumer and Marc-André Rose who have contributed to the research presented in this thesis in different ways. I am thankful for the terrific technical support that I have received from René Borowski, Dr. Paul Meuffels, Georg Pickartz, Grigory Potemkin, Cerstin Makovicka, Stephan Masberg, Marcel Gerst, Jochen Friedrich, Sylvia de Waal, Kevin Kistermann, Sebastian Zischke, Cleo Herwartz and Thomas Pössinger.

Moreover, I enjoyed being involved in the inspiring work on water splitting catalysis in the group of Felix Gunkel at PGI-7, which allowed me to work with a wonderful team. While many great colleagues where involved I would like to express my heartfelt gratitude to Christoph Baeumer in particular for his constant support and mentoring.

I was lucky to enjoy the company of many great colleagues and friends during coffee breaks or shared working hours in the lab as well as after-work meetings and scientific meetings around the world. A few names I would like to mention are Jacqueline Börgers, Alexander Gutsche, Seongeun Park, Felix Hensling, Moritz Kindelmann, Fabian Grimm, Alexander Schwiers, Marcus Wohlgemuth, Lisa Heymann, Suqin He, Hong Yan, Alexandros Sarantopoulos, Nick Williams, George Wilson, Zonghao Shen and Jia Guo.

I would also like to thank my friends outside of science that made my time so valuable during my time in Cologne. I'm grateful for relaxed nights at Kitty's, the Trude-Herr soccer crew, delicious food and wine in Nippes, long nights with the Krefelder guys, my day ones from Lückerath and my family around the world.

I thank my parents who have always encouraged me to follow my interest for the more complex things in life. Importantly, Mia deserves a very special thanks for her loving support.

Typeset April 14, 2022

Band / Volume 582
Closed Carbon Cycle Mobility –
Klimaneutrale Kraftstoffe für den Verkehr der Zukunft
F. Schorn, J. Häusler, J. L. Breuer, S. Weiske, J. Pasel, R. C. Samsun, R. Peters (2022), 220 pp
ISBN: 978-3-95806-636-6

Band / Volume 583
Machine learning for monitoring groundwater resources over Europe
Y. Ma (2022), viii, 125 pp
ISBN: 978-3-95806-638-0

Band / Volume 584
Mechanical properties of single and dual phase proton conducting membranes
W. Zhou (2022), IV, VI, 133 pp
ISBN: 978-3-95806-645-8

Band / Volume 585
Improvements to gravity wave physics from an observational perspective
M. Geldenhuys (2022), vii, 136 pp
ISBN: 978-3-95806-647-2

Band / Volume 586
Impact of severe convection on the water vapor mixing ratio in the extra-tropical stratosphere
D. Khordakova (2022), ii, 136 pp
ISBN: 978-3-95806-648-9

Band / Volume 587
Effects of salt precipitation during evaporation on porosity and permeability of porous media
J. Piotrowski (2022), xxvii, 139 pp
ISBN: 978-3-95806-650-2

Band / Volume 588
IEK-14 Report 2022
Forschung für die Energiewende und den Wandel im Rheinischen Revier
B. Emonts (Hrsg.) (2022)
ISBN: 978-3-95806-652-6

Band / Volume 589
Oxidation of monoterpenes studied in atmospheric simulation chambers
L. L. Hantschke (2022), 188 pp
ISBN: 978-3-95806-653-3

Band / Volume 590
NiFe Layered Double Hydroxide Catalysts for Oxygen Evolution Reaction in Alkaline Water Electrolysis
W. Jiang (2022), 165 pp
ISBN: 978-3-95806-658-8

Band / Volume 591
Optimizing Cross-linked Infrastructure for Future Energy Systems
L. Welder (2022), xxiii, 360 pp
ISBN: 978-3-95806-659-5

Band / Volume 592
Evaluation von Reaktorkonzepten für die CO_2-basierte Methanolsynthese aus Wasserstoff und Kohlendioxid mithilfe von CFD-Simulationen
S. Weiske (2022), x, 369 pp
ISBN: 978-3-95806-661-8

Band / Volume 593
Spectral Induced Polarization of Biochar in Soil
Z. Gao (2022), XXVI, 155 pp
ISBN: 978-3-95806-662-5

Band / Volume 594
Eignung von nickelhaltigen Katalysatorsystemen in sauren Medien zur Nutzung im Betrieb von Brennstoffzellen
A. Karaca (2022), iv, 249 pp
ISBN: 978-3-95806-663-2

Band / Volume 595
Seasonal Comparison of the Chemical Composition and Source Apportionment of Aerosols during the Year-Long JULIAC Campaign
L. Liu (2022), VIII, 189 pp
ISBN: 978-3-95806-668-7

Band / Volume 596
Nanoscale Understanding and Control of Metal Exsolution in Perovskite Oxides
M. L. Weber (2022), ix, 160 pp
ISBN: 978-3-95806-669-4

Weitere ***Schriften des Verlags im Forschungszentrum Jülich*** unter
http://wwwzb1.fz-juelich.de/verlagextern1/index.asp

Energie & Umwelt / Energy & Environment
Band / Volume 596
ISBN 978-3-95806-669-4

Mitglied der Helmholtz-Gemeinschaft

JÜLICH
Forschungszentrum